

**Band
419**

Verlagsschriftenreihe des Heinz Nixdorf Instituts
Prof. Dr.-Ing. Christoph Scheytt (Hrsg.)
Schaltungstechnik

Meysam Bahmanian

Optoelectronic Phase-Locked Loop, Theory and Implementation

PADERBORN UNIVERSITY

DOCTORAL THESIS

**Optoelectronic Phase-Locked Loop,
Theory and Implementation**

**Optoelektronischer Phasenregelschleife,
Theorie und Implementierung**

Author:
Meysam Bahmanian

Bibliografische Information Der Deutschen Bibliothek

Die Deutsche Bibliothek verzeichnet diese Publikation in der Deutschen Nationalbibliografie detaillierte bibliografische Daten sind im Internet über <http://dnb.ddb.de> abrufbar

Band 419 der Verlagsschriftenreihe des Heinz Nixdorf Instituts

© Heinz Nixdorf Institut, Universität Paderborn – Paderborn – 2024

ISSN (Online): 2365-4422

ISBN: 978-3-947647-38-5

Das Werk einschließlich seiner Teile ist urheberrechtlich geschützt. Jede Verwertung außerhalb der engen Grenzen des Urheberrechtsgesetzes ist ohne Zustimmung der Herausgeber und des Verfassers unzulässig und strafbar. Das gilt insbesondere für Vervielfältigung, Übersetzungen, Mikroverfilmungen, sowie die Einspeicherung und Verarbeitung in elektronischen Systemen.

Als elektronische Version frei verfügbar über die Digitalen Sammlungen der Universitätsbibliothek Paderborn.

Satz und Gestaltung: Meysam Bahmanian

PADERBORN UNIVERSITY

DOCTORAL THESIS

Optoelectronic Phase-Locked Loop, Theory and Implementation

*zur Erlangung des akademischen Grades eines
DOKTORS DER INGENIEURWISSENSCHAFTEN (DR.-ING.)*

*A thesis submitted in fulfillment of the requirements
for the degree of Doctor of Philosophy*

in the

Faculty of Computer Science, Electrical Engineering and Mathematics
System and Circuit Technology Group
Heinz Nixdorf Institute

Author:
Meysam Bahmanian
Paderborn

Tag des Kolloquiums:

19.02.2024

Referent:

Prof. Dr.-Ing. J. Christoph Scheytt

Korrrferent:

Prof. Dr. Franz Xaver Kärtner

Declaration of Authorship

I, Meysam Bahmanian, declare that this thesis titled, “Optoelectronic Phase-Locked Loop, Theory and Implementation” and the work presented in it are my own. I confirm that:

- This work was done wholly or mainly while in candidature for a research degree at this University.
- Where any part of this thesis has previously been submitted for a degree or any other qualification at this University or any other institution, this has been clearly stated.
- Where I have consulted the published work of others, this is always clearly attributed.
- Where I have quoted from the work of others, the source is always given. With the exception of such quotations, this thesis is entirely my own work.
- I have acknowledged all main sources of help.
- Where the thesis is based on work done by myself jointly with others, I have made clear exactly what was done by others and what I have contributed myself.

Signed: Meysam Bahmanian

Date: 15.04.2023

اسماعیل دژوار سیداحمد شکراللهی محمدجواد زاهدی آرتین مریدی محمد امینی مینو مجیدی فریدون محمودی مهسا ژینا امینی

نگین صالحی عارف عاشوری مهرگان زحمتکش صدرالدین لیتانی کمال فقهی عزیز مرادی آرتین صیادی سینا نادری امید مهدوی

احمدرضا قلیچی دانش رهنما محمد عبداللہی حسین جزی اسرا پناهی سیدمحمد حسینی مهرزاد بهروز مهران رجبی میلاد درخشان

سینا ملایری محمد خواجری دره بالایی آرتیکا قائم مقامی رامین کریمی رامین فاتحی علی جلیلی علی بنی اسد علی اکبر ربیعی آروین مدلی گلزاری

شاهو خضری مائده جوانفر افشین آشام محمد شریعتی اسماعیل مولودی مهدی فرحانی نگین عبدالملکی ساسان قربانی

فریدون فرجی مهرشاد شهیدی محمد لطف‌اللهی امین معرفت (معروفی) کیوان درویشی زانبار ابوبکر کبری شیخ سقا

حسین اکبرزاده میلان حقیقی سیدعلی سیدی هادی حق‌شناس مسعود احمدزاده سارینا ساعدی صدف موحدی مطلب سعید پیرو فرشته احمدی

ابوالفضل باثو محمد مهرداد لیتا نامور رضا خشنود هولاری رضا اسماعیل‌زاده پوریا کیانی آیتاز جواهری

محمد صامری بیرانوند بهتاز افشاری حمیدرضا مال‌میر میلاد جاویدپور مرصیه دشمن زبیری محسن قیصری احسان خواجوی دره بالایی رحیم کلیچ

سامان قادرپور محمد کشاورز فرید کورآوند پویا شیدا پریسا بهمنی ابراهیم میرزایی کومار درافتاده محمود کشوری کیوان شریف

مختار احمدی ناهید مصطفی‌پور مؤمن زند کریمی نسیم صدقی رسول محمدآقا امیر (عارف) قربانپور

ایمان بهزادپور اهل رضا بنیادی نادیا عارفان محمدرضا سروری مرتضی سلطان‌نیا احسان خان محمدی پویا رجب‌نیا غزاله جلالی کنعان آقایی

شیرین عزیزاده سپهر شریفی طریقه محمد مام صالح پریسا عسگری مهدی عسگری ستاره تاجیک الهه سعیدی فرزین فرخی

متین عبداللہ‌پور محسن محمدی کامران شهبازی عزت‌الله شهبازی سیدفرهاد حسینی حمیدسعید مظفری میثم مقدسی دیاکو مهرنوبی

امیرحسین رومیانی نظری عرفان زمانی علی بساکی امیرمهدی ملک محمدی رسول حدادی فرزانه کاظمی دیانا محمودی جعفر قربانی

مهران شکاری علی فاضلی نسرین قادری پرستو مرادخانی اسماعیل حیدری عبدالله محمودپور نیما نوری محمد انوش نیا

محمدرضا سروی حنا‌نه کیا مهدی حضرتی محمدامین حشمتیان علی روزبهانی محمدحسین سالاری محمد قائمی فرد

فاتح مام قادری محمدرضا فردوسی عباس لویی مرگان کدخدایی رضا ساعد مهدی زاهدی محمدرضا بالی لاشک محمدحسین فرجی

میلاد خاوری سمیه محمودی نژاد میلاد استادهاشم مرتضی شیرمحمدی سجاد جعفری سپهر بیرانوند (سام) یاسین جمالزاده کتیل امیرخلیلو

محسن مال میر فریدون احمدی آرش پهلوان ماریا غواصیه مهرباب نجفی سینا فیروزآبادی متین نصری علیرضا کریمی مهدیس حسینی

امیرنوروزی روزبه خادمی سیدمهدی موسوی سعید محمدی بهنام لایق‌پور ایمان محمدی محمدجواد فرمانی امیرعلی فولادی علی مظفری

امیرحسین شمس ابوالفضل مهدی‌پور عرفان رضایی هدیه نعیمانی رضا لطفی مازیار سلیمانیان پدرام آفرنوش مهرداد بهنام اصل مهدی لیلازی

حدیث نجفی زکریا خیال روشنا احمدی مهدی بیرنژاد عرفان خزایی ابوالفضل اکبری دوست سعید ایرانمنش مهرداد انوش نیا

مهرداد عوض‌پور محمد حسین‌خواه جواد حیدری محمدحسن ترکمان محمد فلاح پارسا رضادوست محمدرضا اسکندری رضا شپرنیا

محمد جامه یزرگ فردین بختاری سیدسینا موسوی عبدالسلام گلوانی حسین علی‌کیا محسن پازوکی فرزین لطفی محمدرسول مومنی‌زاده

محسن موسوی مهسا موگویی سیدعباس میرموسی میلاد زارع علیرضا فتحی ساسان باقری سارینا اسماعیل‌زاده صمد برگ‌نیا

فرجاد درویشی یاسر جعفری حمید فولادوند جواد خوانساری علیرضا حبیبی عرفان نظری‌گی محمدجواد زمانی ابوالفضل آدینه‌زاده

نیکا شاکرمی سپارش محمودی پویا (علی) احمدپور پسپرخانی حسین مروتی مرتضی نوروزی احسان علیبازی امیرحسین مهدوی

امیرحسین بساطی امیررضا نادرزاده محمد زارعی فواد قدیمی محراب دولت‌پناه امیرمهدی فرخی‌پور محسن محمدی کوچکسرای

مبین میرکاذهی دانیال شه‌بخش پیمان منبری یحیی رحیمی داریوش عزیزاده نیما شفیق‌دوست عماد حیدری محمدامین تکلی حمید صابغی‌پور

عبدالمالک شهنوازی صادق براهوویی سعید سهراب زهی رحیم‌داد شهلای شعیب درغاله اوپس شکرزهی مونا تقیب

امید نارویی یونس میریلوچ‌زهی یونس شه‌بخش محمد شه‌بخش محمد شه‌بخش محمد سلحشوران کامبیز ریگی علی کردکلاهوری عظیم محمود زهی

حامد باجی‌زهی یاسر بهادرزهی علی براهوویی هستی نارویی مولوی یوسف زبیری یاسر نارویی پارسا همتا عادل بریچی زیاست بادل بلچ

احمد سرگلزایی احمد سارانی ابوبکر نهانی ابوبکر عزیزهی ابراهیم گرگیچ موسی آتشینی عبدالله نارویی سدیس کشانی محمدصادیق نارویی

امیرحمزه شهنوازی امیرحسین پرنیان امید صفرزهی امید شهنوازی امید سارانی اسماعیل حسین‌زهی اسماعیل آبی‌ل احمد شه‌بخش

جلیل رخشانی جابر شیروزی بهزاد ریگی پلال رخشانی پلال آتشینی آرمان حسن‌زهی امین‌الله قلجایی امین گل‌بچه امیرمحمد گمشادزهی

حمید عیسی‌زهی حمزه نارویی حمزه نارویی جواد پوشه جمال‌عبدالناصر محمدحسینی جلیل محمدزهی جلیل قنبرزهی

سامر هاشمزهی ذالغفار حسن‌زهی خلیل قنبرزهی خدانور لجهای حیدر نارویی‌رشید حمید نارویی حمید نارویی

عبدالصمد براهوویی عبدالرحمن بلوچی‌خواه عبدالغاق شهنوازی عبدالجلیل رخشانی صلاح‌الدین گمشادزهی سلیمان عرب سلمان ملکی سامی هاشمزهی

عبدالوحد توحیدنیا عبدالمنان رخشانی عبدالملک شه‌بخش عبدالمجید ریگی عبدالله شه‌بخش عبدالغفور نوربراهویی عبدالغفور دهمرده عبدالصمد ثابتی‌زاده

فرزاد شه‌بخش عمران شه‌بخش عمران حسن‌زهی علی‌اکبر حلقه بگوش علی‌اکبر براهوویی علی عاقل عزیزالله کُبدانی

محمد براهوویی محسن گمشادزهی مجید بلوچ‌زهی شه‌بخش متین قنبرزهی ماه‌الدین شیروزی لال‌محمد عاقل‌زهی لال‌محمد آتشینی

محمدعلی اسماعیل‌زهی محمدرضا ادیب‌توتازهی محمدامین گمشادزهی محمدآقبال نا‌ب‌زهی محمد قلجایی محمد ریگی محمد رخشانی

مصطفی بریچی مرتضی حسن‌زهی محی‌الدین شه‌بخش محمود شهنوازی محمود حسن‌زهی محمود براهوویی محمدآرواق رخشانی محمدعلی گمشادزهی

یونس نارویی یاسر شه‌بخش یاسر شاهو‌زهی نعمت‌الله کُبدانی نجم‌الدین تاجیک مهدی آتشینی موسی ویراء منصور رخشانی

میلاد خوش‌کام کاروان قادری سپهر مقصودی برهان کریمی آیلار حق حمیدرضا روحی دانیال پابندی کیان پیروفلک

اسعد رحیمی آرام حبیبی محمد بزرگر مهدی زارع علیرضا شجاعی آرمان عمادی آرتین رحمانی شهریار محمدی

محسن نیاز علی عراقی سالار مجاور حمید کلی عیسی بیگلری شاهو بهمنی سامان قادری‌گی زانبار‌الله مرادی

مجید عبداللہی آسترکی هانی مرادی امید حسینی شیرکو سلطانی حامد صدیقی مطلب سعیدپور سعید پیرمغانی سمانه نیک‌نام نوید بادیا محمد حسن‌زاده

محمد حسین کمندلو افشین شهامت فواد سواری‌جوان حبیب‌الله فتحی ابراهیم صدری جمشید فتحی حسین عبد پناه کمال احمدی

آرام مجد عباس شفیعی رضا کاظمی شورش نیک‌نام مهران سماک فرزین معروفی آوات قادرپور حامد سلحشور امین نظری هیمین امان

اوپس مسعودی‌زاده سیروس شریفی باگو مهدی بهرنژاد امان اله خان باجی زهی مائده (ماهک) هاشمی جبار فریژاده امیرجواد اسعدزاد حسین زرینجوویی

امید قمصری ریباز صالحی‌وند علی اکبر حیدرزاده سعدی شاه‌رخ‌فر شمال خذیری‌پور رضا کاظمی آرشیا امام‌قلی‌زاده ندا بیات

شهاب‌الدین هاشمی دریا نظمه کوروش پاژخ محمدرضا بادبوت عدنان کمالی امید مؤیدی زارع شهریار عادل‌ی حسین محمدی

سروش سیدی حیدر محالی جمال اعظمی جوهر فتاحی (میری) تحسین میری مسعود تیموری اسماعیل گل‌عنبر حسام حسینی دنیا فرهادی

فرشید موسوی لقمان کاکایی عرفان کاکایی بها‌الدین ویسی طاهر عزیزی ستار رحیمی جلال قربانی سلیمان شکر

ادریس غریب‌زاده محمد احمدی گاکش امیر فراستی شاد مهران رحمانی میلاد معروفی منصور قربانی حسین شیرازی‌پور مهران توانا عمران ابرکار

امجد عنایتی هیوا جانان آزاد حسین‌پوری حامد مولایی دشتی دوران توتازهی آسو قادری جواد موسوی مصطفی شهبانی

فرهاد خسروی امیر محمد دلبری مهدی کابلی کفشگیری اصغر آقایی غفور مولودی عبدالرحمان بختیاری هزارام خسروی

بهرام مرادیان علی عباسی مسلم هوشنگی میلاد آصفی جواد رضایی علی مولایی علی محمدی سجاد قائمی رشید رشیدی

سعید مرادی میلاد سعیدی سعید اسعدی وحید خانی امید زارع موبدی رضا شریعتی مهدی زارع اشکدزی اشرف نیکبخت

مولوی عبدالواحد ریگی حمیدرضا روحی میلاد استادهاشم رضا زارع-مؤیدی علی فاضلی هادی چاکسری محمدرضا مشهدی فراهانی فواد محمدی

Vorwort

ZEIT ist eine der rätselhaftesten physikalischen Größen in unserem Universum. Sie erscheint normalerweise als unabhängige Variable in unseren Gleichungen, das unaufhaltsame Phänomen der Welt, das sich nur in eine Richtung bewegt. Man kann angemessen behaupten, dass alle unsere wissenschaftlichen Experimente direkt oder indirekt mit der Zeit zu tun haben; ob wir nun ein schwarzes Loch beobachten — oder vielleicht nicht beobachten! — weit entfernt von unserem Planeten, oder ob wir die Ziehzeit unserer Tasse Tee messen wollen, wir brauchen einen Sinn von Zeit; eine Referenzeinheit, auf die wir uns verlassen können. Eine Zeitreferenz ist die Grundlage für unser modernes digitales Lebens. Das Wort *digital* enthält das Konzept der Zeit in sich: eine Abfolge von Werten mit einem festen Takt. Aber was ist dieser *feste Takt* und inwieweit kann dieser Takt *fest* sein? Verschiedene Techniken nutzen unterschiedliche physikalische Prinzipien, um dieses Ziel zu erreichen: von periodischen Schwingungen in einem Kristallgitter bis hin zu Atomen, die zwischen zwei Energiezuständen oszillieren. Diese Techniken haben ihre eigenen Vor- und Nachteile und Präzision bei der Zeitmessung, und es hängt schließlich von der Anwendung ab, welche Methode gewählt wird. Die Fehler, die diese Techniken für den gesamten Anwendungsapparat mit sich bringen, sind ein entscheidender Faktor. Je kleiner die physikalischen Größen sind, mit denen wir es zu tun haben, desto höhere Präzision wird für die Zeitmessung benötigt. Der technische Fortschritt hat uns dazu gebracht, physikalischen Prinzipien mit besserer Präzision bei der Messung von Zeiteinheiten anzuwenden. Eines dieser Prinzipien ist die Verwendung von periodischen Laserpulsen, genauer gesagt von modengekoppelten Lasern, als Referenz für Zeit. Die Anwendung dieser Technik erfordert eine neue Klasse von Geräten, sodass das emittierte Licht des Lasers in elektronischen Schaltungen genutzt werden kann. Darüber hinaus müssen wir verschiedene Raten oder Frequenzen mit unserem periodischen optischen Impuls erzeugen, da wir eine breite Palette von Systemen haben, die Signale mit unterschiedlichen Frequenzen benötigen. Dies sind Herausforderungen auf dem Weg zu einer präzisen optischen Referenz für die Zeit als Herzstück unserer elektronischen Systeme. Diese Herausforderungen sind das Thema der vorliegenden Arbeit, und wir werden sie behandeln und praktische Lösungen für sie anbieten.

— Meysam Bahmanian
April 2023
Paderborn

Preface

TIME is one of the most puzzling physical quantities in our universe. It usually appears as an independent variable in our equations, the non-stoppable phenomenon of the world that moves only in one direction. It is fair to say that all our scientific experiments directly or indirectly relate to time; whether we are observing a black hole — or maybe not observing! — far from our planet or whether we want to measure the brewing time of our cup of tea, we need a sense of time; a reference unit to rely on. Having a time reference is the foundation of our modern digital life. The word *digital* contains the concept of time in itself: a sequence of values at a *fixed rate*. But what is this fixed rate and to which degree this rate can be *fixed*? Various techniques use different physical principles to achieve this goal, from periodic vibrations in a crystal lattice to atoms oscillating between two energy states. These techniques have their own pros and cons and precision in measurement of time, and it is the application that determines which one to choose. The errors these techniques impose on the whole application apparatus are a decisive factor. The smaller the physical quantities we deal with, the more precision required to measure time. The advancement of technology has pushed us to employ physical principles with better precision in time unit measurement. One of these principles is using periodic laser pulses, or more precisely *mode-locked laser*, as a reference for time. Employing this technique requires to use a new class of devices, so we can use the emitted light from the laser in our electronic circuits. In addition, we need to generate different rates, or frequencies, using our periodic optical pulse, as we have a wide range of systems that require signals with different frequencies. These are the challenges in our way to have a precise optical reference for time as the beating heart of our electronic systems. These challenges are the topic of this work, and we will address them and provide practical solutions for them.

— Meysam Bahmanian
April 2023
Paderborn

List of Publications

Journal Publications

- M. Bahmanian and J. C. Scheytt, "A 2–20-GHz ultralow phase noise signal source using a microwave oscillator locked to a mode-locked laser," *IEEE Transactions on Microwave Theory and Techniques*, vol. 69, no. 3, pp. 1635–1645, 2021. DOI: [10.1109/TMTT.2020.3047647](https://doi.org/10.1109/TMTT.2020.3047647)
- M. Bahmanian, C. Kress, and J. C. Scheytt, "Locking of microwave oscillators on the interharmonics of mode-locked laser signals," *Opt. Express*, vol. 30, no. 5, pp. 7763–7771, Feb. 2022. DOI: [10.1364/OE.451894](https://doi.org/10.1364/OE.451894)
- M. Bahmanian and J. C. Scheytt, "Noise processes and nonlinear mechanisms in optoelectronic phase-locked loop using a balanced optical microwave phase detector," *IEEE Transactions on Microwave Theory and Techniques*, vol. 70, no. 10, pp. 4422–4435, 2022. DOI: [10.1109/TMTT.2022.3197621](https://doi.org/10.1109/TMTT.2022.3197621)

Conference Publications

- M. Bahmanian, J. Tiedau, C. Silberhorn, and J. C. Scheytt, "Octave-band microwave frequency synthesizer using mode-locked laser as a reference," in *2019 International Topical Meeting on Microwave Photonics (MWP)*, IEEE, Oct. 2019, pp. 1–4. DOI: [10.1109/MWP.2019.8892046](https://doi.org/10.1109/MWP.2019.8892046)
- M. Bahmanian, S. Fard, B. Koppelman, and J. C. Scheytt, "Ultra low phase noise and ultra wide-band frequency synthesizer using an optical clock source," in *2020 IEEE MTT-S International Microwave Symposium (IMS)*, Aug. 2020, pp. 1283–1286. DOI: [10.1109/IMS30576.2020.9224118](https://doi.org/10.1109/IMS30576.2020.9224118)

Other Publications

- J. C. Scheytt, D. Wrana, M. Bahmanian, and I. Kallfass, "Ultra-low phase noise frequency synthesis for thz communications using optoelectronic pll's," in *2020 Second International Workshop on Mobile Terahertz Systems (IWMTS)*, 2020, pp. 1–4. DOI: [10.1109/IWMTS49292.2020.9166347](https://doi.org/10.1109/IWMTS49292.2020.9166347)
- S. Kruse, M. Bahmanian, P. Kneuper, C. Kress, H. G. Kurz, T. Schneider, *et al.*, "Phase noise investigation for a radar system with optical clock distribution," in *The 17th European Radar Conference*, Jaarbeurs Utrecht, Netherlands, Jan. 2021. DOI: [10.1109/EuRAD48048.2021.00018](https://doi.org/10.1109/EuRAD48048.2021.00018)
- C. Kress, M. Bahmanian, T. Schwabe, and J. C. Scheytt, "Analysis of the effects of jitter, relative intensity noise, and nonlinearity on a photonic digital-to-analog converter based on optical Nyquist pulse synthesis," *Opt. Express*, vol. 29, no. 15, pp. 23 671–23 681, Jul. 2021. DOI: [10.1364/OE.427424](https://doi.org/10.1364/OE.427424)

Zusammenfassung

Optoelektronischer Phasenregelschleife, Theorie und Implementierung

In dieser Arbeit werden die Theorie und die Implementierung der Erzeugung von Mikrowellensignalen auf der Grundlage einer optischen Frequenzreferenz unter Verwendung einer Phasenregelschleife vorgestellt: der optoelektronischen Phasenregelschleife (OEPLL). Der Phasendetektor der OEPLL wird als balancierter optischer Mikrowellen-Phasendetektor (BOMPD) bezeichnet und arbeitet in einer gemischt-elektro-optischen Domäne, da er in der Lage sein muss, die Phasendifferenz zwischen zwei Signalen zu unterscheiden, die in unterschiedlichen Domänen liegen.

Modengekoppelte Laser (MLL) haben gezeigt, dass sie in der Lage sind, optische Pulse mit ausgezeichnetem Kurzzeit-Timing-Jitter zu erzeugen. Der Timing-Jitter der optischen Pulsfolge von MLLs kann weitaus besser sein als der von Quarz- und Oberflächenwellenoszillatoren. Darüber hinaus erzeugen MLLs eine oberwellenreiche Intensitätswellenform, die für die Breitband-Frequenzsynthese verwendet werden kann. Diese Eigenschaften von optischen MLL-Pulsen machen sie zu einem perfekten Kandidaten für die Verwendung als Frequenzreferenz für die Erzeugung rauscharmer HF-Signale.

Unter den verschiedenen Techniken zur Erzeugung von Mikrowellensignalen mit MLL ist die OEPLL besonders interessant für die breitbandige Mikrowellenfrequenzsynthese. Daher konzentriert sich diese Arbeit hauptsächlich auf die Analyse, den Entwurf und die Optimierung der OEPLL. Es wird ein allgemeines Modell der PLL auf Komponentenebene gegeben und dann wird dieses Modell an die OEPLL angepasst. Diese Modellierung auf Systemebene wird dann verwendet, um das Verhalten der OEPLL zu simulieren und das Phasenrauschen zu optimieren. Darüber hinaus wird eine gründliche Analyse des BOMPD durchgeführt, die sich mit verschiedenen Rauschprozessen befasst, die das Phasenrauschen beeinflussen. Die nichtlinearen Mechanismen des BOMPD werden ebenfalls diskutiert. Die nichtlineare Analyse führt zur Entdeckung eines neuen Betriebsregimes der OEPLL, das sie in die Lage versetzt, auf Zwischenharmonische (d.h. nicht-ganzzahlige Harmonische) der optischen Referenz-Wiederholrate einzurasten.

Die in dieser Arbeit entwickelte Theorie wird genutzt, um zwei verschiedene Breitband-OEPLLs zu entwerfen und zu implementieren. Der erste Entwurf verwendet einen VCO, der eine Oktave des Frequenzbereichs 5–10 GHz abdeckt. Die OEPLL hat ein In-Band-Phasenrauschen von -135 dBc/Hz bei 100 kHz Offset-Frequenz und 10 GHz Trägerfrequenz, mit einem Effektiv-Jitter von 13,8 fs, integriert von 1 kHz bis 100 MHz. Der zweite Entwurf verwendet einen breitbandigen Yttrium-Eisen-Granat (YIG)-Oszillator mit einem Frequenzbereich von 2–20 GHz. Die OEPLL hat ein In-Band-Phasenrauschen von -150 dBc/Hz bei 100 kHz Offset-Frequenz und 10 GHz Trägerfrequenz, mit einem Effektiv-Jitter von 2,8 fs, integriert von 1 kHz bis 100 MHz. Dieses Resultat des In-Band-Phasenrauschens ist 10–20 dB besser als das der besten kommerziellen Frequenzsynthesizern auf dem aktuellen Markt.

Abstract

Optoelectronic Phase-Locked Loop, Theory and Implementation

This work presents the theory and implementation of microwave signal generation based on optical frequency reference using phase-locked loop (PLL) technique, the optoelectronic phase-locked loop (OEPLL). The phase detector of the OEPLL is called balanced optical microwave phase detector (BOMPD). It operates in a mixed-electro-optical domain, as it should be able to discriminate the phase difference between two signals that are in different domains.

Mode-locked lasers (MLLs) have shown their potential to generate optical pulses with excellent short-term timing jitter. The timing jitter of the optical pulse train of MLLs can be better than that of the quartz and surface acoustic wave (SAW) oscillators by orders of magnitude. In addition, MLLs generate a harmonic-rich intensity waveform which can be used for wideband frequency synthesis. These features of MLL optical pulses make them a perfect candidate to be used as a frequency reference for ultralow noise RF generation.

Among various microwave signal generation techniques using MLL, OEPLL is especially interesting for wideband microwave frequency synthesis. Therefore, this work mainly focuses on OEPLL analysis, design and optimization. A generic model of PLL at component level is given and then this model is adapted to OEPLL. This system-level modeling is then used to simulate the OEPLL response, stabilize the system and optimize the phase noise. In addition a detailed and thorough analysis of BOMPD is provided which addresses different noise processes affecting its phase noise. The nonlinear mechanisms with respect to the optical and RF inputs of BOMPD are also discussed. The nonlinear analysis leads to the discovery of a new operating regime of OEPLL which makes it capable of locking on interharmonics (i.e non-integer harmonics) of the optical reference repetition rate.

The developed theory in this work is utilized to design and implement two different wideband OEPLLs. The first design uses a semiconductor voltage controlled oscillator (VCO) which covers an octave of frequency range 5–10 GHz. The OEPLL has an in-band phase noise of -135 dBc/Hz at 100 kHz offset frequency at 10 GHz carrier frequency, with an rms-jitter of 13.8 fs integrated from 1 kHz to 100 MHz. The second design uses a wideband Yttrium Iron Garnet (YIG) oscillator with a frequency range of 2–20 GHz. The OEPLL has an in-band phase noise of -150 dBc/Hz at 100 kHz offset frequency at 10 GHz carrier frequency, with an rms-jitter of 2.8 fs integrated from 1 kHz to 100 MHz. This level of in-band phase noise is 10–20 dB better than the best-in-class state-of-the-art commercial frequency synthesizers.

Acknowledgements

Foremost, I would like to express my sincere gratitude to Prof. Christoph Scheytt for giving me the opportunity to do this thesis at System and Circuit Technology Group.

My sincere thank goes to Bastian Koppelman and Peer Adelt for the stimulating discussions and a lively working environment. I am specially thankful to Christian Kress for proof-reading the theory and correction of the mistakes in the formulas, for agreeing to translate parts of this work, and for his always-ready-to-help spirit. I am thankful to Saeed Fard for his friendly and productive collaboration. I would like to also thank Birgit Ritter for her continued support.

Contents

Optoelectronic Phase-Locked Loop, Theory and Implementation

List of Publications	xi
Zusammenfassung	xiii
Abstract	xv
1 Introduction	1
1.1 Frequency synthesizer	2
1.2 RF Generation Using Mode-Locked Lasers	5
1.2.1 Direct detection	5
1.2.2 Pulse interleaving rate multiplier	6
1.2.3 Spectral filtering rate multiplier	7
1.2.4 Heterodyne mixing and optical phase-locked loop	7
1.2.5 Optoelectronic phase-locked loop	9
1.2.6 Comparison and conclusions	9
1.3 Scope of the thesis	11
2 Mode-Locked Laser	13
2.1 Active mode-locked laser	14
2.2 Passive mode-locked laser	16
2.3 Properties of mode-locked laser signals	18
2.4 $f - 2f$ interferometry	20
2.4.1 Optical frequency division	22
2.5 Summary and conclusion	22
3 Theory of Optoelectronic Phase-Locked Loop	25
3.1 Generic theory of phase-locked loop	25
3.2 Dynamics of optoelectronic phase-locked loop	29
3.3 Characteristic function of BOMPD	32
3.3.1 BOMPD behavior in dynamics of OEPLL	35
3.4 Summary and conclusion	37
4 Noise and Nonlinearity in Optoelectronic Phase-Locked Loop	39
4.1 Noise in BOMPD	39
4.1.1 Shot noise of photodiodes	40
4.1.2 Generation-Recombination noise	45
4.1.3 Relative intensity noise of the MLL	49
4.1.4 Noise of MZM bias voltage	49
4.2 Nonlinear effects in BOMPD	51
4.2.1 Saturation of the photodiodes	51
4.2.2 RF nonlinearity in BOMPD and interharmonic locking	54
4.3 Summary and conclusion	56

5	Design, Simulation and Characterization of OEPLL	59
5.1	BOMPD design and characterization	59
5.2	OEPLL design and characterization	62
5.2.1	Design I: OEPLL with semiconductor VCO	62
5.2.2	Design II: improved OEPLL with YIG oscillator	64
5.3	Interharmonic OEPLL	66
5.4	Summary and conclusion	67
6	Conclusion and Outlook	69
6.1	Comparison with the state of the art	69
6.2	Outlook	71
A	Phase Noise, Timing Jitter and Amplitude Noise	73
A.1	Phase noise and timing jitter	73
A.2	Timing jitter	75
A.3	Amplitude noise	75
B	Fourier Transform	77
C	Characteristic function of balanced intensity modulator	79
D	Transfer Characteristic of the Bias Electrode Noise	81
E	Gain of BOMPD with Nonlinear Photodiode	83
F	Phase Noise Measurement Techniques	85
F.1	Baseband PSD measurement using cross correlation	85
F.2	Single-channel phase noise measurement	87
F.3	Two-channel phase noise measurement	90
G	Phase Noise and Jitter of OEPLL with YIG Oscillator	93
	Bibliography	97

List of Figures

1.1	Comparison of the phase noise of the state of the art	2
1.2	Abstract representation of frequency synthesizer	3
1.3	Block diagram of PLL with loop frequency divider and reference frequency multiplier	3
1.4	Phase noise comparison of microwave frequency synthesizers	4
1.5	RF generation using direct detection of optical pulses and space-charge effects in photodiodes	6
1.6	Schematic of rate multiplier and its effect on generated RF power	7
1.7	Rate multiplier using Fabry-Perot cavity	7
1.8	RF generation using optical phase-locked loop	8
1.9	Optoelectronic phase-locked loop	9
1.10	Phase noise comparison of different RF generation methods using MLL optical pulses	10
2.1	Electric field of mode-locked laser signal	13
2.2	Schematic of mode-locked laser	14
2.3	Schematic of active mode-locked laser	14
2.4	Evolution of active MLL spectral lines after each roundtrip	15
2.5	MLL pulse in time and frequency domain	18
2.6	Illustration of $f - 2f$ interferometry	21
2.7	Effect of CEO frequency stabilization on phase noise	23
3.1	Generic block diagram of phase-locked loop	25
3.2	Linear model of phase-locked loop in the phase domain	26
3.3	Open loop and closed-loop transfer functions of PLL	28
3.4	Optoelectronic phase-locked loop	30
3.5	Linear model of the optoelectronic phase-locked loop in the phase domain	31
3.6	Phase detector characteristic curves for different excitation amplitudes and bias points	36
4.1	Linear model of photodiode including shot noise	41
4.2	Modeling of non-stationary shot noise	42
4.3	Effect of pulsed stimulation on GR noise	46
4.4	Photodiode noise measurement setup and results	48
4.5	Effect of photodiode saturation on BOMPD performance	51
4.6	Photodiode integrated responsivity	52
4.7	Effect of photodiode saturation on BOMPD characteristic function	53
4.8	BOMPD nonlinear model with respect to RF signal	54
4.9	BOMPD characteristic curves for interharmonic locking	56
5.1	Test setup for characterization of BOMPD	59
5.2	Effect of RF harmonics on bompd characteristic curves	60

5.3	Effect of dc bias point on BOMPD characteristic curves	61
5.4	Measured BOMPD characteristic curves for interharmonic locking . . .	61
5.5	Extending the frequency range of frequency synthesizer	62
5.6	Block diagram of OEPLL design I with semiconductor VCO.	63
5.7	Phase noise of OEPLL design I with semiconductor VCO	63
5.8	Block diagram of OEPLL design II with YIG oscillator	64
5.9	Phase noise of OEPLL design II with YIG oscillator	65
5.10	Measured power spectrum of the OEPLL output signal	67
5.11	Measured phase noise of the OEPLL at interharmonic frequencies . . .	68
6.1	Phase noise comparison of this work with state-of-the-art frequency synthesizers	70
A.1	Illustration of phase noise in a sinusoidal signal	73
A.2	Effect of phase noise on the signal spectrum.	74
A.3	Illustration of amplitude noise in a sinusoidal signal	75
C.1	Block diagram of Mach-Zehnder modulator with two separate elec- trodes for RF modulation and dc bias.	79
F.1	Schematic of PSD measurement setup using cross correlation tech- nique.	85
F.2	Phase detection using double balanced mixer.	88
F.3	Phase noise measurement using delay line frequency discrimination technique.	88
F.4	Phase noise measurement using PLL technique.	89
F.5	Two-channel phase noise measurement system	90
F.6	Two-channel phase noise measurement of mmWave and terahertz sig- nals	91

List of Tables

3.1 Behavior of different PLL transfer functions at close-in and far offset frequencies.	28
B.1 Fourier series	77
B.2 Fourier transform	77
B.3 Lowpass equivalent of bandpass signals.	78

List of Abbreviations

ADC	analog-to-digital converter.
BIM	balanced intensity modulator.
BOMPD	balanced optical microwave phase detector.
CEO	carrier envelope offset.
COEO	coupled optoelectronic oscillator.
CW	continuous wave.
DAC	digital-to-analog converter.
DCF	dispersion compensation fiber.
DDS	direct digital synthesis.
DRO	dielectric resonator oscillator.
EDFA	Erbium-doped fiber amplifier.
ESR	equivalent series resistance.
FEL	free electron laser.
GR	generation-recombination.
GRIN	graded index.
HNLF	highly nonlinear fiber.
IF	intermediate frequency.
LiNbO ₃	lithium niobate.
LNOI	lithium niobate-on-insulator.
LO	local oscillator.
LTI	linear time-invariant.
MLL	mode-locked laser.
MMLL	monolithic mode-locked laser.
MUTC	modified uni-traveling carrier.
MZM	Mach-Zehnder modulator.
NLTL	nonlinear transmission line.
OEO	optoelectronic oscillator.
OEPLL	optoelectronic phase-locked loop.
OFD	optical frequency division.
OpAmp	operational amplifier.

OPLL	optical phase-locked loop.
PIC	photonic integrated circuit.
PLL	phase-locked loop.
PPLN	periodically poled lithium niobate.
PSD	power spectral density.
SA	saturable absorber.
SAW	surface acoustic wave.
SC	supercontinuum.
SHG	second harmonic generation.
SiP	silicon photonics.
SLCO	sapphire-loaded cavity oscillator.
SNR	signal to noise ratio.
SRD	step recovery diode.
SUT	signal under test.
UTC	uni-traveling carrier.
VCO	voltage controlled oscillator.
YIG	Yttrium Iron Garnet.

Chapter 1

Introduction

Low-jitter frequency references have a wide range of applications from wireless and wireline communications, high-speed analog-to-digital converter (ADC), and digital-to-analog converter (DAC) to fundamental research facilities, such as large array telescope systems and free electron lasers (FELs) [1]. Depending on the operating principle of these frequency references, their output could be either in the electrical or in the optical domain. In the electrical domain, oven-controlled quartz oscillators and SAW oscillators can offer phase noise levels down to (-120, -140) dBc/Hz at (1 kHz, 100 kHz) offset frequencies normalized to a 10-GHz carrier [2–4] (Please see Appendix A for mathematical modeling of phase noise). Sapphire-loaded cavity oscillators (SLCOs) exhibit better phase noise performance by approximately two orders of magnitude but with higher manufacturing cost and size [5, 6]. The so-called optoelectronic oscillators (OEOs) use a continuous wave (CW) laser and a feedback loop in a mixed electro-optical domain and have better phase noise than quartz and SAW oscillators, but their output signal is spurious because of their long cavity [7]. The coupled optoelectronic oscillators (COEOs) replace the CW laser with another optical feedback loop consisting of an optical amplifier and an optical filter. The smaller delay of the feedback path in COEO increases the intervals of the spurs in the frequency spectrum of the RF output and enhances the spectral purity [7]. Using this technique, Matsko *et al.* [8] reported a 10-GHz COEO with a phase noise of (-125, -145) dBc/Hz at (1 kHz, 100 kHz) offset frequencies and Ly *et al.* [9] reported a COEO-based millimeter-wave signal generation at 90 GHz with a phase noise of (-104, -129) dBc/Hz at (1 kHz, 100 kHz) offset frequencies. In the optical domain, medium-priced and compact MLLs achieve a phase noise performance better than quartz and SAW oscillators at offset frequencies above 1 kHz [10–12]. Further improvement of MLL phase noise (beyond or comparable with SLCOs) has been achieved using different techniques such as optical frequency division (OFD) in which one of the MLL optical comb lines is locked onto an ultrastable CW laser [6, 13]. Recently, Kalubovilage *et al.* [14] demonstrated a compact monolithic mode-locked laser (MMLL) with an exceptional open-loop phase noise performance comparable to OFD systems. Figure 1.1 compares the phase noise of the state of the art for different types of reference oscillators normalized to 10-GHz carrier frequency. The phase noise scaling is based on an ideal frequency multiplier without any additive phase noise.

In addition to the phase noise performance of these oscillators, the temporal and spectral properties of their output signals should be considered according to the application. Especially, if such an oscillator is used as a reference oscillator in a PLL, a waveform with high harmonic content is desired, as it enables the designer to lock a tunable oscillator on any of these harmonics in order to maximize the output frequency range of the PLL. Quartz and SAW oscillators have usually sinusoidal output waveforms. The harmonic content of their output signals barely exceeds

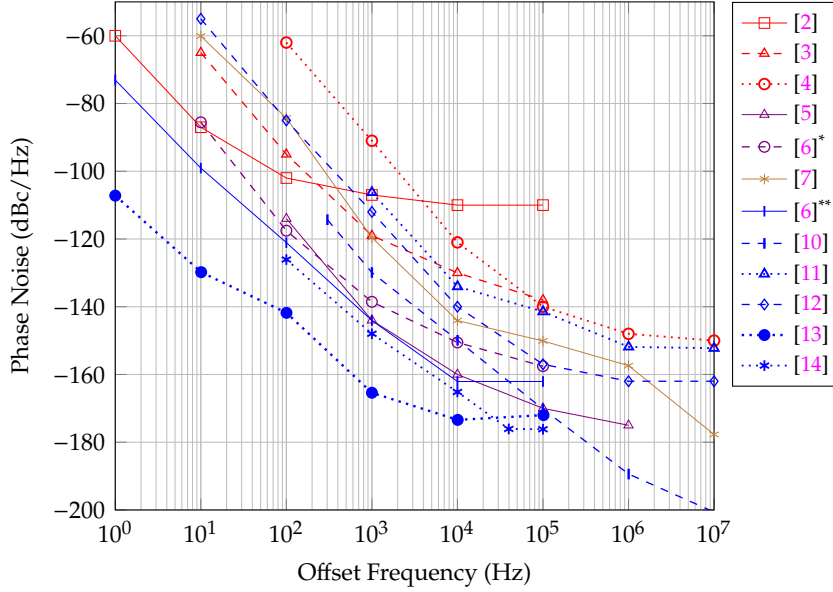


FIGURE 1.1: Comparison of the phase noise of the state of the art, normalized to 10 GHz carrier frequency: (red) quartz and SAW oscillators, (brown) coupled optoelectronic oscillator, (violet) sapphire loaded cavity oscillators and (blue) optical sources. [6]^{*} and [6]^{**} correspond to the phase noise of the sapphire loaded cavity oscillator and the mode-locked laser reported in [6], respectively.

a few gigahertz because of their narrowband resonator and limited bandwidth of their electronic components. Therefore, higher harmonic content is usually generated using step recovery diodes (SRDs) or nonlinear transmission lines (NLTLs) [15, 16]. The harmonic content of a COEO is limited by the bandwidth of its electronic components and the optical filter used in the feedback loop. Therefore, the spectral width of COEO is in the range of a few nanometers (less than 100 GHz) [8, 9]. In contrast to these electronic and optoelectronic reference oscillators, MLLs achieve subpicosecond pulsewidths and THz-wide optical frequency combs [10, 13, 17]. These frequency combs correspond to a harmonic rich intensity (optical cycle averaged intensity) waveform and are therefore well suited for microwave signal generation.¹

1.1 Frequency synthesizer

The main objective in designing a frequency synthesizer is to translate the frequency of a low noise reference signal to an RF signal with the desired frequency. This translation is ideally without introduction of additional noise. This is illustrated in Figure 1.2 at an abstract level with the phase noise power spectral densities. The phase noise of the reference is scaled by the frequency multiplication factor. Any additional noise above this level is considered as additive phase noise of the frequency synthesizer.

The simplest approach to translate the reference frequency to the desired frequency is using a nonlinear device that generates harmonics of its input signal, known as the frequency multiplier. The additive phase noise of frequency multipliers is dependent on their technology and generally with proper device selection

¹Partial results of this section have been published in [18].

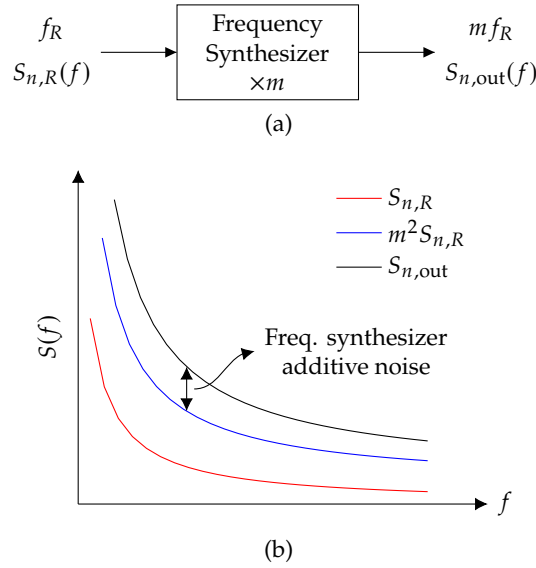


FIGURE 1.2: (a) Abstract representation of frequency synthesizer and (b) its phase noise plots; f_R , reference frequency; $S_{n,R}(f)$, reference phase noise; m , frequency multiplication factor; $S_{n,out}(f)$, frequency synthesizer phase noise.

and design can be below the input signal phase noise. The main drawback of this technique is that the available frequencies are limited only to the harmonics of the reference signal and non-integer multiplication factors are not possible. Besides, the output signal of frequency multipliers contains both leakage of the input signal as well as other undesired harmonics. High quality RF generation would then require post-multiplication filtering and suppression of undesired harmonics. This can be more complicated for wideband frequency synthesizers, as the output signal has a wide frequency range and a tunable filter is required.

The standard approach for wideband frequency synthesis from a low phase noise reference signal is using a PLL. On the one hand, the frequency of the reference signal of a PLL is usually in the megahertz range and the output frequency is in the gigahertz range. On the other hand, the PLL requires equal frequencies at the input of its phase detector. In order to match these frequencies, there are two fundamental approaches:

1. Reducing the frequency of the output signal, illustrated in Figure 1.3(a).
2. Increasing the frequency of the reference signal, illustrated in Figure 1.3(b).

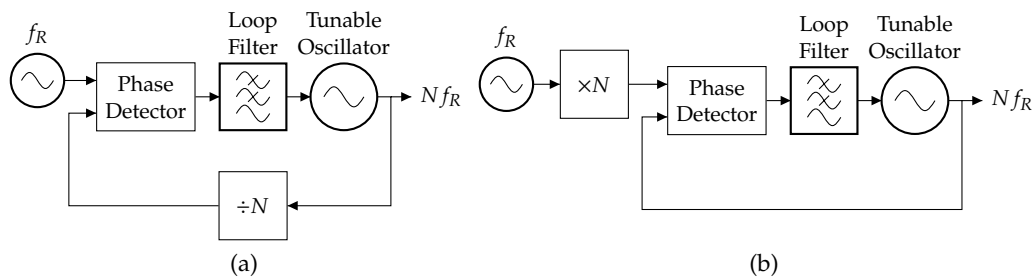


FIGURE 1.3: Block diagram of PLL with (a) loop frequency divider and (b) reference frequency multiplier.

The first method, reducing the frequency of output signal, is a popular technique in low-cost commercial frequency synthesizers. By using a digitally programmable fractional frequency divider, the output frequency can be tuned in fine frequency steps [19]. The main drawback of this method is that the additive phase noise of the PLL scales with the loop division factor and surpasses the phase noise of the ultralow noise frequency references.

The second method, increasing the frequency of the reference signal, does not have a loop divider to reduce the frequency of the RF signal. Therefore, it has lower additive phase noise compared to the first method. The drawback is that the frequency of the reference signal is increased using harmonic generators and only integer multiples of the reference frequency are available. In order to improve the frequency resolution, the output frequency of the PLL is mixed with the signal from a fine-step secondary PLL, using direct mixing or offset phase-locked loop scheme.

The low noise optical pulse trains of MLLs have shown a great potential for low noise RF generation. The phase noise of these optical references can be better than their electronic counterparts by 3 orders of magnitude. This has led to efforts to generate a low noise microwave signal from an MLL [20–24]. Among these methods, phase locking of a microwave oscillator onto an MLL using BOMPD is a cost-effective and relatively compact solution, as its only electro-optical components are an intensity modulator and one pair of photodetectors [24, 25]. In addition, the RF signal is sampled with the optical reference using an intensity modulator which has a significantly higher bandwidth compared to double-balanced mixers that are typically used in high-performance fully electronic phase-locked loops. The downside of such an OEPLL is the requirement for phase adjustment of its microwave signal paths and relatively sophisticated microwave setup. An alternative topology for a BOMPD proposed by [26] significantly simplifies the architecture and does not require microwave phase shifters, bandpass filters, and balanced mixers by using an electro-optical balanced intensity modulator (BIM). Using this method, Jung *et al.* [27] locked a dielectric resonator oscillator (DRO) at 8 GHz onto an MLL with a residual rms-jitter of 838 as integrated from 1 Hz to 1 MHz.

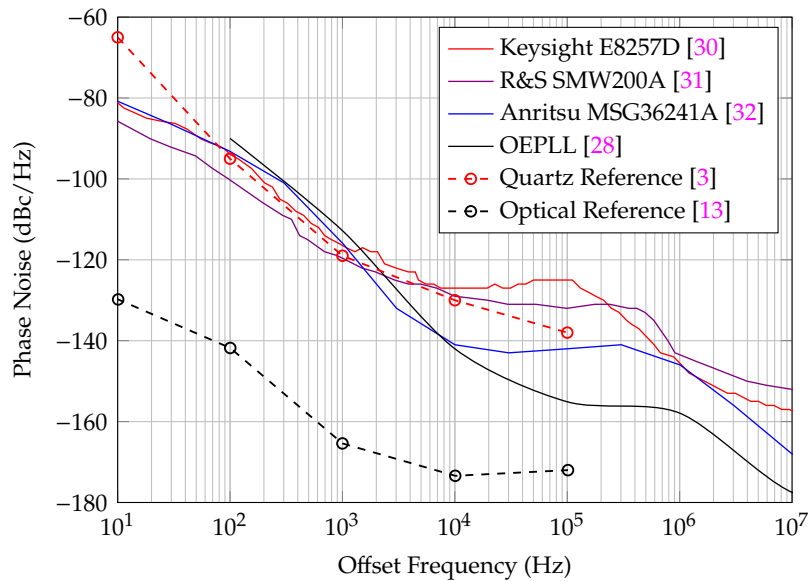


FIGURE 1.4: Phase noise comparison of microwave frequency synthesizers at 10 GHz and frequency references normalized to 10 GHz carrier frequency.

The results from [27, 28] demonstrate the potential of OEPLLs for ultralow-phase-noise frequency synthesis. However, the small bandwidth of the DRO makes the approach impractical for broadband frequency synthesis. In addition, the fiber-based Sagnac-modulator is bulky, expensive, and sensitive to mechanical vibrations. Currently most OEPLL systems operate only at a single frequency or a very limited frequency range. Therefore, more research is needed toward microwave OEPLL frequency synthesizers with a large output frequency range and compact size. Nejadmalayeri *et al.* [29] replaced the fiber Sagnac-modulator with a lithium niobate (LiNbO₃) MZM and the DRO with a microwave instrument. This allowed to reduce the size and increase the output frequency range but [29] did not achieve the performance of [27].

The OEPLLs have the potential for wideband frequency synthesis, since the MHz wide loop bandwidth can filter the optical reference harmonics. The phase noise of the current state-of-the-art frequency synthesizers currently is limited by their Quartz and SAW based reference they use. Figure 1.4 compares the phase noise of the state-of-the-art wideband frequency synthesizers (from Keysight, Rohde & Schwarz and Anritsu [30–32]) with the OEPLL reported in [28]. It can be seen that at offset frequencies above approximately 1 kHz the OEPLL outperforms traditional fully electronic frequency synthesizers, thanks to the clean reference signals of MLLs. The phase noise of OEPLLs at close-in offset frequencies below approximately 10 kHz can further be improved if a better optical reference is used. Therefore, the OEPLLs can have better phase noise by approximately 3 orders of magnitude.

1.2 RF Generation Using Mode-Locked Lasers

In the previous sections, we demonstrated that the phase noise of MLLs can be better than that of traditional frequency references such as Quartz and SAWs oscillators. In addition, we discussed that the role of frequency synthesizer is to generate an arbitrary frequency that is phase-locked to the low-noise frequency reference. In this section, we discuss state-of-the-art RF frequency generation techniques based on MLL optical reference.

1.2.1 Direct detection

The simplest approach for MLL-based RF generation is direct detection of MLL pulses using a photodiode, illustrated in Figure 1.5(a). Since the generated photocurrent is harmonic rich, a bandpass filter is required to select the desired harmonic.

The signal to noise ratio (SNR) of this type of RF generator is limited by the thermal noise of output termination load and the maximum achievable RF power from the photodiode. The output power of the photodiode is also limited by high energy MLL pulses mainly due to the nonlinear space-charge effect [33–36]. The main limitation of this technique is the bandwidth of the photodiode. High frequency photodiodes can easily achieve tens of gigahertz bandwidth when stimulated with low-pulse-energy optical beams. However, high peak power optical stimulation of photodiodes, which is required for low noise RF generation, limits the photodiode bandwidth due to the nonlinear space-charge effects, illustrated in Figure 1.5(b). High energy pulses of MLLs generate many charge carriers (electron-hole pairs) in the active region of photodiode. The Coulomb interaction between these charge carriers creates an electric field, E_i , that counteracts the device built-in electric field, E_b . This counteracting field reduces the charge carrier velocities and consequently leads to an

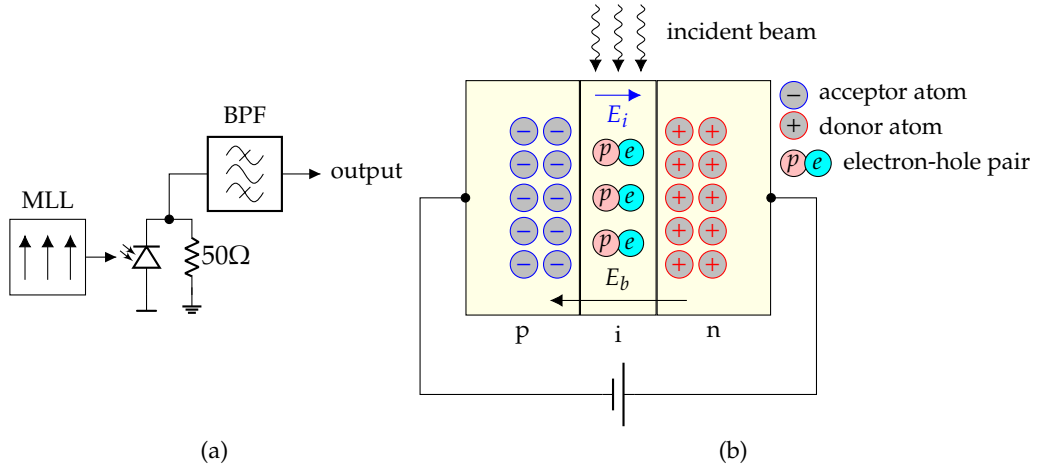


FIGURE 1.5: (a) Schematic of optical pulse direct detection and (b) illustration of space-charge effect in PIN photodiode.

increase of the transit time of charge carriers and the response time and reduction of the photodiode bandwidth [37]. While the thermal noise floor remains at the same level, the decrease of the photodiode bandwidth leads to reduction of the desired harmonic power and lower signal to noise ratio. Another undesired phenomenon caused by the nonlinear space-charge effects is the conversion of the optical pulse amplitude noise to photocurrent phase noise [38]. Both these mechanisms lead to degradation of phase noise of the generated RF signal.

In order to mitigate the photodiode space-charge effect, uni-traveling carrier (UTC) photodiode and modified uni-traveling carrier (MUTC) photodiode use an undepleted p-layer to absorb light to inject the electrons into the drift region and reduce the transit time and the space-charge effect [39, 40]. The illumination condition has also been optimized through beam shaping using a graded index (GRIN) lens coupling which increases the illumination cross section and reduces the peak magnitude of the optical field [41, 42]. It has been shown that increasing the optical beam diameter leads to a more uniform distribution of mobile carriers in the device and reduction of the counteracting electric field [34, 35, 43].

1.2.2 Pulse interleaving rate multiplier

One can mitigate the nonlinear space-charge effects by reducing the energy of the optical pulses. This method can be realized in a lossless fashion by increasing the repetition rate of the optical pulses using pulse interleaving technique illustrated in Figure 1.6(a) for a 3-stage $\times 8$ multiplier [6, 13, 23, 44, 45]. The optical pulses are interleaved via 3 segments, where each segment divides the optical beam into two paths and one of the paths adds a delay equal to half of the period of the pulses and then both paths are recombined, increasing the repetition rate by a factor of 2 at the output of each segment. Figure 1.6(b) shows the effect of rate multiplication on the generated RF power at the photodiode.

State-of-the-art MLL-based RF generators use this technique to enhance the photodiode output power and increase the SNR [6, 13, 44]. The main drawback of this method is the output frequencies that can be achieved. While the intensity of the output of MLL has harmonics of f_R , where f_R is the repetition rate of the pulses, the interleaved pulses has harmonics of Nf_R , where N is the rate multiplication factor.

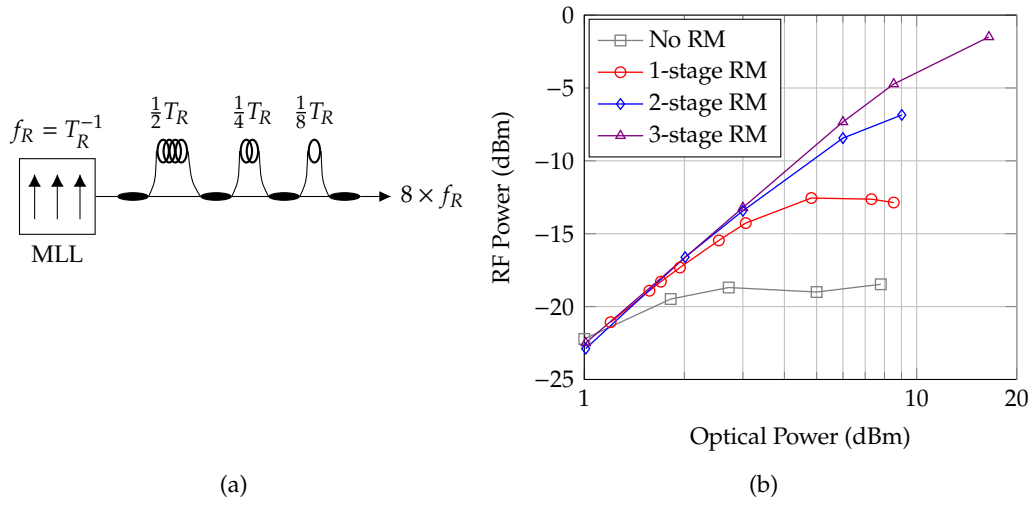


FIGURE 1.6: (a) Schematic of a 3-stage rate multiplier and (b) the effect of rate multiplication on generated RF power at 10 GHz characterized with an MLL with a repetition rate of 250 MHz [44]; RM, rate multiplier.

Therefore, using a rate multiplier enhances the SNR and phase noise of the RF signal, but it comes at the cost of higher frequency steps in the RF generator.

1.2.3 Spectral filtering rate multiplier

Another technique to increase the repetition rate of the optical pulses is combine filtering using a Fabry-Perot cavity shown in Figure 1.7 [44, 46]. Such a cavity has a transmission frequency response with multiple pass-bands located at integer multiples of the fundamental frequency pass-band. Therefore, by adjusting the length of the cavity with a Piezo stage, various rate multiplication factors can be achieved. One drawback compared to pulse interleaving technique is that more optical power budget is needed, as the optical power reflected from the cavity is dissipated. In addition, controlling the cavity length makes the setup more complicated compared to static pulse interleaver and the moving Piezo stage leads to acoustic vibrations and phase noise degradation at close-in offset frequencies below 1 kHz [44].

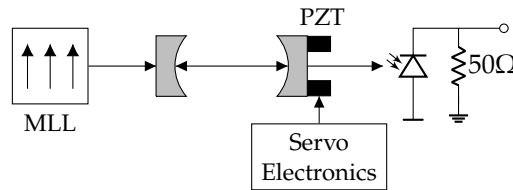


FIGURE 1.7: MLL rate multiplier based on combine filtering using Fabry-Perot cavity [46].

1.2.4 Heterodyne mixing and optical phase-locked loop

Rate multipliers can be seen as optical filters with a periodic transfer response that pass combines that have a certain frequency difference. The periodicity of the transfer function of these filters means the photocurrent generated at the photodiode

still has many harmonics. If the periodicity feature of these filters is removed and only two desired comb lines are allowed to pass, then the generated photocurrent would be just a single tone. A practical implementation of this idea is shown in Figure 1.8(a), known as heterodyne mixing. First, two comb lines with optical frequencies of f_1 and f_2 are selected via comb selection optics tuned at these frequencies. The selected comb lines are then combined and the intensity of the resulting optical field is detected via a photodiode. The frequency of the RF signal at the photodiode output is the frequency difference between the selected comb lines.

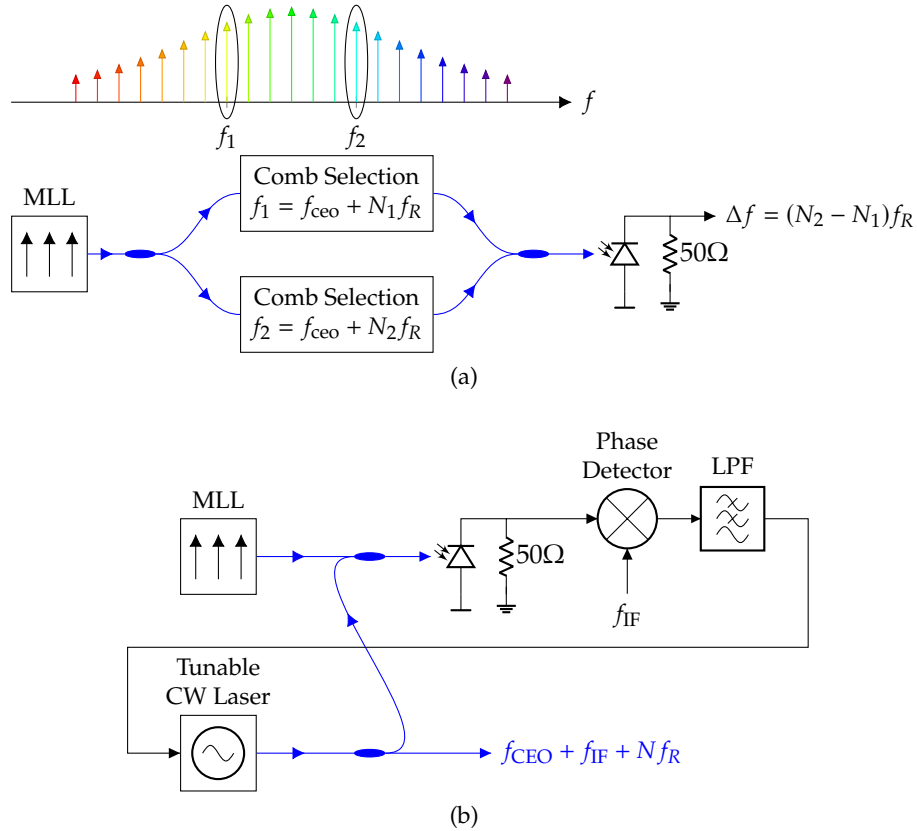


FIGURE 1.8: (a) Schematic of RF generator based on heterodyne mixing of two MLL comb lines. (b) Combine selection using optical phase-locked loop technique (optical connections are shown in blue and electrical connections are shown in black).

One approach for comb line selection is filtering the two desired wavelengths from the MLL spectral lines [47, 48]. This technique requires extremely narrowband optical filters with high quality factors to filter the undesired neighboring comb lines only a few hundreds of megahertz away from the desired comb line. Fabrication and wavelength tuning of such optical devices is a tedious task. In addition, wideband RF frequency synthesis requires tunability of these filters which makes the realization of a frequency synthesizer using this technique even more complicated.

An Alternative approach for optical comb selection would be an optical phase-locked loop (OPLL), illustrated in Figure 1.8(b) [49–52]. The MLL comb lines are combined with the output beam of a tunable CW laser which has an offset frequency, f_{IF} , relative to the target comb line. This relative offset frequency is then detected via a photodetector and is stabilized using an optical phase-locked loop. The optical PLL uses a phase detector and a stable intermediate frequency (IF) to generate an error signal which is then filtered and fed back to the tunable CW laser to stabilize it.

1.2.5 Optoelectronic phase-locked loop

One problem arising in direct photodetection, whether a rate multiplier is used or not, is the excess noise caused by conversion of amplitude noise of the optical pulses to phase noise [23, 24, 38]. Kim *et al.* [24] suggested extracting the timing information of the optical pulses in the optical domain, before photodetection, and use this timing information to control a microwave tunable oscillator. This idea led to the development of a new class of electro-optical systems, the balanced optical microwave phase detector (BOMPD) and optoelectronic phase-locked loop (OEPLL), illustrated in Figure 1.9 [18, 24, 25, 27, 53, 54].

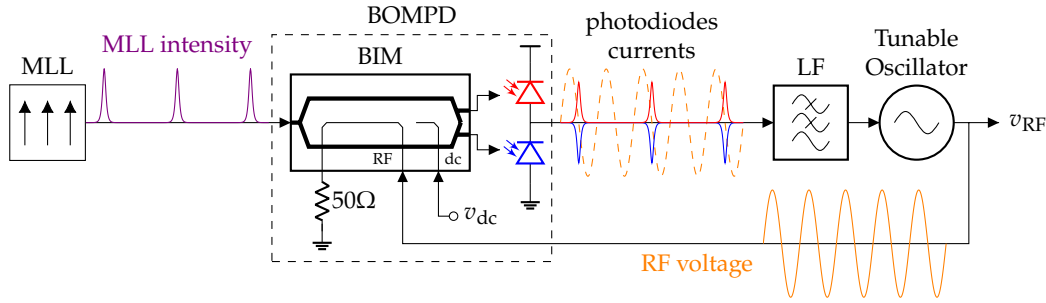


FIGURE 1.9: Simplified block diagram of the OEPLL.

In this approach, the optical pulses of the MLL are modulated by the RF signal using a balanced intensity modulator (BIM). The modulated optical pulses carry information about the relative timing between the optical pulses and the microwave signal. This information is then converted into an electrical current by a pair of photodiodes and is used to adjust the microwave signal timing with that of the optical pulse train. It is noteworthy to mention that the OEPLL is similar to its fully electronic counterpart and the BOMPD operates similar to a balanced mixer that is used in many PLLs as a phase detector. However, the phase detector of the OEPLL has to operate in a mixed electro-optical domain. Since the intensity of the optical pulse train is harmonic rich, the OEPLL can potentially lock on any harmonic of the optical reference repetition rate.

1.2.6 Comparison and conclusions

Now that we investigated various techniques of RF generation using optical pulses of MLLs, one might ask which method is preferred. The answer to this question mainly lies in the application. Here we focus on wideband versatile frequency synthesizer and, based on this application, compare these methods.

Figure 1.10 compares the phase noise performance of these methods [13, 27, 28, 44, 47, 49]. Direct detection method can be used to generate any harmonic of the reference repetition rate. However, the RF signal power generated at the photodiode decreases as the pulse energy increases. For a given average optical power, this means higher repetition rates are desired. Although increasing the repetition rate is possible, using a pulse interleaver or a Fabry-Perot cavity, the frequency resolution of the RF generator increases, and fewer frequencies are available at the photodiode output. In addition, for many RF applications the signal purity is important and filtering the subharmonics² is necessary. This can be difficult from two aspects; firstly, a tunable bandpass filter is required to select the desired harmonic; secondly,

²Note that the undesired harmonics of the reference repetition rate are considered as the subharmonics of the desired RF frequency.

sufficient suppression (usually more than 60 dBc) of undesired harmonics is difficult to achieve, as they can be very close to the desired harmonic (for instance 250 MHz away from a 10 GHz carrier).

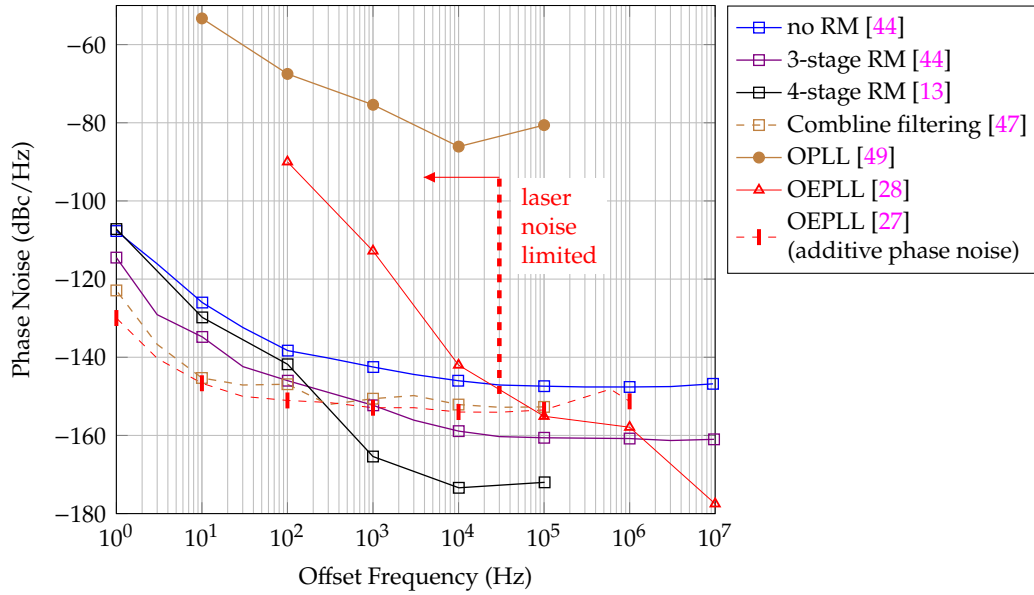


FIGURE 1.10: Phase noise comparison of different RF generation methods using MLL optical pulses; RM, rate multiplier.

The heterodyne mixing approach with filtering the comb lines has practical difficulties due to tunability and high quality-factor requirement for the optical filters. For instance, an optical filter at 200 THz with a bandwidth of 200 MHz requires a quality factor of 10,000 which is hard to achieve. The alternative heterodyne-mixing technique, the OPLL, shows a poor phase noise performance and has a high additive phase noise. Possible reasons could be high phase noise of the tunable laser source and failing to sufficiently suppress it in the OPLL. Another possible reason could be the high noise of the CEO frequency of the MLL. A simple first order analysis suggests the CEO noise is canceled after recombination of the locked optical tones. However, it is possible the CEO noise is not perfectly canceled due to small delay mismatch in the OPLLs, or the noise can undergo a nonlinear transformation at the baseband components or due to nonlinear characteristic curve of the tunable CW laser. This transformed noise is not canceled during the photodetection process and shows itself as additive phase noise. These mechanisms include the phase noise of the optical carriers which is orders of magnitude higher than that of microwave signals. Therefore, the leakage of the optical carrier phase noise to the phase of the generated microwave signal can have a strong adverse effect on its phase noise.

The OEPLL has interesting features that make it a viable candidate for low-noise and wideband frequency synthesis. From the phase noise perspective, the OEPLL reported by Jung *et al.* [28] has a phase noise performance similar to the state-of-the-art multi-stage repetition rate multipliers. The phase noise at offset frequencies below approximately 30 kHz is limited by the MLL and is expected to improve if an MLL with higher spectral purity is used. The additive phase noise of the same setup has also been reported in [27] and proves that the OEPLL performance is limited by the MLL at those offset frequencies. Although Jung *et al.* [28] uses a narrowband dielectric resonator oscillator (DRO) as the tunable oscillator, there is wide range of microwave oscillators with various bandwidths and phase noise performance available. The

balanced intensity modulators (BIMs) with tens of gigahertz bandwidth are standard devices and available. Therefore, the OEPLL does not have the practical limitations of other techniques while having a phase noise performance comparable to state-of-the-art RF generators. Therefore, the OEPLL is well suited for wideband microwave signal generation using the optical pulses of MLLs.

1.3 Scope of the thesis

In this report, for the first time, we provide a mathematical foundation for OEPLL analysis. At the system level, the classical PLL theory is adapted to OEPLL. This provides a systematic approach for OEPLL design. At the component level, we derive the characteristic function of the phase detector and calculate the phase detector gain which is required for system level analysis. In order to find the additive phase noise of OEPLL, various noise sources in OEPLL are identified and their effect on the phase noise are shown. To explore the limitations of OEPLL, the nonlinear mechanisms that affect the OEPLL performance are investigated and their effect on the phase detector gain and additive noise of OEPLL are discussed. This nonlinear analysis reveals a new operating regime in OEPLL which can be used to lock on the interharmonics (non-integer harmonics) of the optical reference. This comprehensive analysis which addresses the noise processes and nonlinear mechanisms in OEPLL is the first of its kind. Finally, two wideband OEPLLs are presented. The first OEPLL uses a semiconductor VCO and has a frequency range of 5–10 GHz. The second OEPLL uses a YIG oscillator which has lower phase noise and higher frequency range, 2–20 GHz, compared to semiconductor VCO. To the author's knowledge, these works are the only reported wideband OEPLLs. The results of our work have been published in peer reviewed journals and been confirmed by the scientific community [18, 53–56].

This report is organized as follows. In Chapter 2, the operating principle of mode locked laser is explained. Two fundamental types of MLLs are introduced and their governing equations and their solutions are discussed. A popular and Nobel prize winning scheme of optical frequency stabilization using $f - 2f$ interferometry is presented which has paved the way for extremely low-noise optical reference generation and optical frequency metrology. In Chapter 3, RF generation using OEPLL scheme is discussed and the relevant equations are derived. In Chapter 4, different noise sources as well as nonlinear mechanisms that affect the performance of OEPLL are shown and the results are discussed. Chapter 5 shows two practical examples of OEPLL and the measurement results are compared with the theory explained in Chapter 3 and Chapter 4. Finally, in Chapter 6, the measurement results are compared with the current low-noise state-of-the-art phase-locked loops.

Chapter 2

Mode-Locked Laser

Optical pulses from mode-locked lasers have attracted attention for a wide range of applications because of their special properties such as extremely short pulse width, high peak power and excellent jitter. Extremely wideband pulses of MLLs have made optical frequency metrology down to Hertz resolution possible and connected the frequency measurement link between microwave domain and optical domain [57–59]. In addition, MLLs have found their way in a wide range of applications such as frequency comb spectroscopy, optical sampling, photonic analog-to-digital converters (ADC), photonic radar, and ultra low noise microwave signal generation [6, 13, 22, 28, 60–69]. Since mode-locked laser is used as the reference of OEPLL, a basic understanding of its operation and the properties of its output optical pulse train is necessary. In this chapter, we investigate basic theory of mode-locking and properties of MLL optical pulses. Note that the MLLs have various operating regimes depending on their structure. The materials presented in this chapter are not intended to be a comprehensive analysis of MLLs, but rather to provide a basic understanding of mode-locking theory and mathematical modeling of MLL optical pulses.

Mode-locked laser is basically a laser with many longitudinal (or axial) modes which have a frequency difference equal to the inverse of the laser cavity roundtrip time

$$f_{n+1} - f_n = \frac{1}{T_R}, \quad (2.1)$$

where f_{n+1} is the frequency of the $n + 1^{\text{th}}$ mode, f_n is the frequency of the n^{th} mode and T_R is the roundtrip time. This is illustrated graphically in Figure 2.1(a). These interlocked combines correspond to an optical pulse with a period of T_R in the time domain, illustrated in Figure 2.1(b).

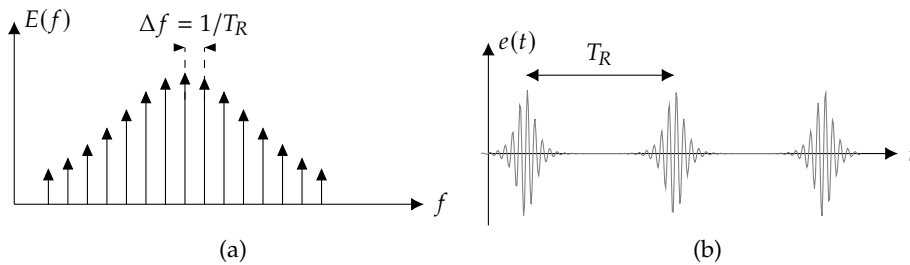


FIGURE 2.1: Electric field of mode-locked laser output signal (a) in the frequency domain and (b) in the time domain.

The generation of these locked modes is achieved by placement of an element in the laser cavity that is not linear time-invariant (LTI), as illustrated in Figure 2.2. Such a non-LTI element can favor generation of axial modes locked to each other. After

each roundtrip of light in the laser cavity, the number of generated modes increases until the light reaches the steady state and a stable pulse is generated. Depending on the type of non-LTI element used in the laser cavity, MLLs are divided into two main categories, active MLLs and passive MLLs. We explain these two fundamental types of MLLs in the following sections. For the analysis of passive MLL, we only consider mode-locking with fast saturable absorber (SA). Detailed analysis of various mode-locking techniques can be found in [70–72].

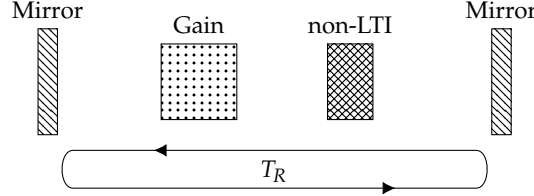


FIGURE 2.2: Schematic of mode-locked laser (adopted from [70]).

2.1 Active mode-locked laser

Figure 2.3 shows the schematic of active MLL. In active mode-locking, generation of locked-modes is achieved by placing a time varying element, a modulator, in the laser cavity which is stimulated by a periodic external source.

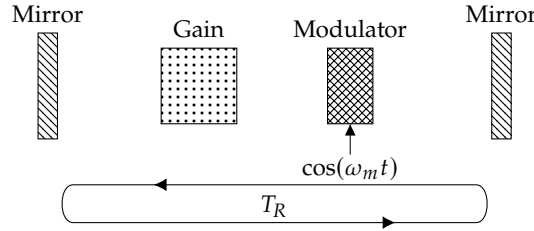


FIGURE 2.3: Schematic of active mode-locked laser (adopted from [70]).

We assume the stimulation waveform is sinusoidal with a angular frequency of ω_m and the modulator introduces the following time-varying loss to the cavity

$$\text{Modulator Loss} = e^{-\Delta_m [1 - \cos(\omega_m t)]}, \quad (2.2)$$

where Δ_m is the modulation constant. Assuming $\Delta_m \ll 1$, the modulator loss can be approximated as

$$\text{Modulator Loss} \approx 1 - \Delta_m [1 - \cos(\omega_m t)] = 1 - \Delta_m + \frac{1}{2}\Delta_m e^{-j\omega_m t} + \frac{1}{2}\Delta_m e^{j\omega_m t}. \quad (2.3)$$

The modulator loss as function of time is illustrated in Figure 2.4(a). Equation (2.3) shows that the modulator reduces the amplitude of the original spectral line by $\tilde{E}\Delta_m$ and increases the amplitude of neighboring spectral lines by $\tilde{E}\frac{1}{2}\Delta_m$, where \tilde{E} is the field *amplitude* of the input of the modulator and the upper tilde (\sim) denotes the lowpass equivalent of a bandpass signal. For further details about the relation between bandpass and lowpass transformation of signals in time and frequency domain please see Appendix B.

The laser mode-locking mechanism can be explained via generation of modulation sidelobes each time the light makes a roundtrip in the cavity. Initially, there is

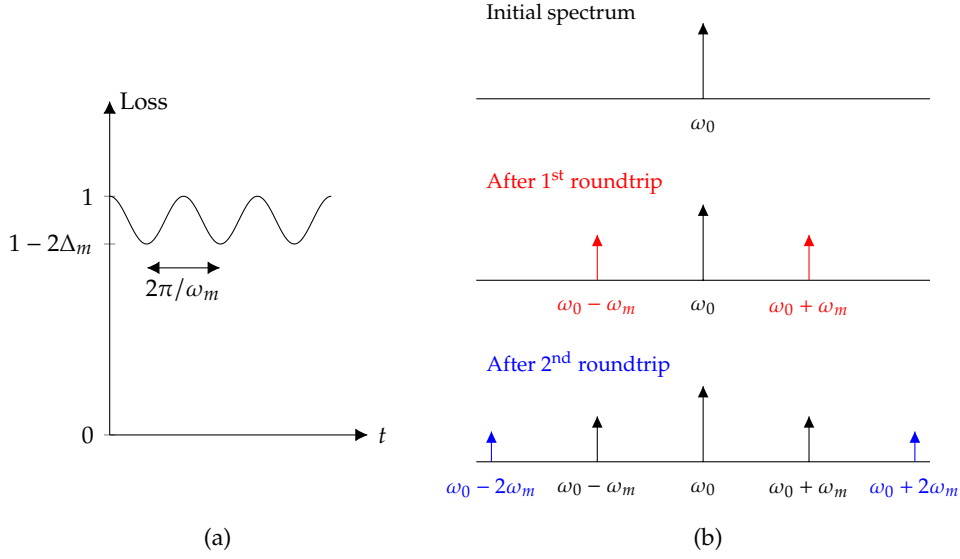


FIGURE 2.4: (a) Modulator loss as a function of time and (b) evolution of active MLL spectral lines after each roundtrip.

just one spectral line of light in the cavity at the cavity center angular frequency ω_0 . After the first roundtrip, two sidelobes are formed at $\omega_0 \pm \omega_m$ around the initial spectral line. After the second roundtrip, each of the 3 spectral lines formed after the second roundtrip are modulated again and five spectral lines are formed at $\omega_0, \omega_0 \pm \omega_m, \omega_0 \pm 2\omega_m$. This process continues until the MLL reaches the steady state. A stable locking requires the roundtrip time T_R to be matched to the modulation angular frequency ω_m . Hence it is assumed

$$\omega_m = \frac{2\pi}{T_R}. \quad (2.4)$$

In order to formulate the active MLL master equation, it is assumed that the gain medium has a saturated *Lorentzian* line shape around the center angular frequency ω_0 as

$$G^+(\omega) = \frac{g_0}{1 + \left(\frac{\omega - \omega_0}{\Omega_g}\right)^2}. \quad (2.5)$$

where the superscript + sign denotes only the positive frequencies of the spectrum. The master equation of active mode locked laser is derived by finding the variation of the field amplitudes of the cavity axial modes after each round trip.

$$\Delta \tilde{E}_n = \left\{ \frac{g_0}{1 + \left(\frac{n\omega_m}{\Omega_g}\right)^2} - l \right\} \tilde{E}_n + \frac{1}{2} \Delta_m (\tilde{E}_{n-1} - 2\tilde{E}_n + \tilde{E}_{n+1}), \quad (2.6)$$

where \tilde{E}_n is the amplitude of the n^{th} combline, $\Delta \tilde{E}_n$ is its change after one roundtrip and l is the cavity loss. The first term in (2.6) is the sum of gain and cavity loss after one round trip. The second term is the variation of the n^{th} mode due to modulation of the mode itself and its neighboring modes after one roundtrip according to (2.3). The discrete difference equation (2.6) can be turned into a differential equation with the following approximations [70]

- The discrete angular frequencies are replaced by a continuous spectrum $\omega \approx n\omega_m$.
- First order polynomial approximation of gain as $G^+(\omega) \approx g_0 \left[1 - \left(\frac{\omega - \omega_0}{\Omega_g} \right)^2 \right]$.
- Replacing the term $\tilde{E}_{n-1} - 2\tilde{E}_n + \tilde{E}_{n+1}$ with its continuous equivalent $\omega_m^2 \frac{d^2 \tilde{E}}{d\omega^2}$.

With these assumptions, (2.6) can be rewritten in a continuous fashion as

$$\Delta \tilde{E}(\omega) = (g_0 - l)\tilde{E}(\omega) - g_0 \left(\frac{\omega}{\Omega_g} \right)^2 \tilde{E}(\omega) + \frac{1}{2} \Delta_m \omega_m^2 \frac{d^2 \tilde{E}}{d\omega^2}. \quad (2.7)$$

In steady state, the complex field spectrum does not change and $\Delta \tilde{E}(\omega) = 0$. The solution of (2.7) is therefore a Gaussian pulse [70]

$$\tilde{E}(\omega) = E_0 e^{-\tau^2 \omega^2}, \quad (2.8)$$

where

$$\tau^4 = \frac{2g_0}{\Delta_m \omega_m^2 \Omega_g^2}. \quad (2.9)$$

The complex amplitude of the optical pulse in time domain can be found by taking the inverse Fourier transform of (2.8) as

$$\tilde{e}(t) = e_0 e^{-(t/2\tau)^2}. \quad (2.10)$$

Therefore, active MLL can produce a stable optical pulse with a Gaussian shape. It should be noted that active MLL requires an external oscillator which controls the time-variant cavity loss. This external stimulation of the laser cavity leads to synchronization of the MLL optical pulse train with the external source. Consequently, the phase noise performance of active MLL cannot exceed that of the stimulation source, and active MLL has the same noise limitations as traditional electronic frequency references.

2.2 Passive mode-locked laser

In active MLL, generation of locked axial modes is realized via a time varying element controlled by an external sinusoidal source. Another possibility to generate short optical pulses is using a nonlinear element in the cavity that favors high intensities, the so-called saturable absorber. After each roundtrip of light in the cavity, the low-intensity intervals of the optical pulse are attenuated more than the high-intensity intervals. This leads to pulse shortening and spectral broadening of the optical signal. The shortened pulse is then amplified in the next roundtrip, effectively with higher peak power than that of the previous roundtrip.

The passive MLL master equation is derived similar to (2.6), but in the time domain. Therefore, the cavity components are now modeled in the time domain.

Saturable absorber The intensity dependent loss of a fast saturable absorber, $s(t)$, can be written as

$$s(t) = \frac{s_0}{1 + I(t)/I_{\text{sat}}}, \quad (2.11)$$

where s_0 is the unsaturated loss of the SA, $I(t)$ is the instantaneous intensity of the optical field and I_{sat} is the saturated intensity of the SA. Assuming an effective area of A_{eff} for the optical field, the intensity can be written as

$$I(t) = \frac{|\tilde{e}(t)|^2}{A_{\text{eff}}}, \quad (2.12)$$

where $\tilde{e}(t)$ is the optical field amplitude. The saturable absorber equation in (2.11) can be approximated by its first order polynomial expansion as

$$s(t) \approx s_0 \left(1 - \frac{I(t)}{I_{\text{sat}}} \right) = s_0 - \gamma |\tilde{e}(t)|^2, \quad (2.13)$$

where $\gamma = s_0/A_{\text{eff}}I_{\text{sat}}$.

Gain medium The gain medium described in (2.5) has a bandpass behavior around ω_0 . The pulse complex amplitude is affected by the complex lowpass equivalent of the gain medium transfer function

$$\tilde{G}(\omega) = G^+(\omega + \omega_0) = \frac{g_0}{1 + \left(\frac{\omega}{\Omega_g} \right)^2}. \quad (2.14)$$

This lowpass equivalent is approximated by its first order polynomial expansion as

$$\tilde{G}(\omega) \approx g_0 \left(1 - \frac{\omega^2}{\Omega_g^2} \right). \quad (2.15)$$

The inverse Fourier transform of $\tilde{G}(\omega)$ which acts on the complex pulse amplitude can consequently be found as

$$\tilde{g}(t) \approx g_0 \left(1 + \frac{d^2}{dt^2} \right). \quad (2.16)$$

Passive MLL master equation Now the master equation of passive MLL with fast SA can be found as the change of the optical pulse complex amplitude after one roundtrip. In addition to transfer characteristics of the gain medium and SA, it is assumed that the cavity has a loss of l . The change of the optical field complex amplitude after one roundtrip can therefore be written as [70]

$$\frac{1}{T_R} \frac{\partial}{\partial T} \tilde{e} = (g_0 - l) \tilde{e} + \frac{g_0}{\Omega_g^2} \frac{\partial^2}{\partial t^2} \tilde{e} + \gamma |\tilde{e}|^2 \tilde{e}. \quad (2.17)$$

The solution of (2.17) is a hyperbolic secant function

$$\tilde{e}(t) = E_0 \operatorname{sech} \left(\frac{t}{\tau} \right), \quad (2.18)$$

where the pulse duration and amplitude are related via

$$\tau^2 = \frac{2g_0}{\gamma A_0^2 \Omega_g^2} \quad (2.19)$$

and

$$l - g_0 = \frac{g_0}{\Omega_g^2 \tau^2} . \quad (2.20)$$

Unlike active MLL, passive MLL does not require an external source to get synchronized with, and the intensity-dependent loss is realized using a saturable absorber. Passive MLLs have fine noise properties that go far below the noise of traditional electronic references. By controlling various classical noise sources in passive MLLs, they can reach the theoretical limitation imposed by laws of quantum physics [73–75].

Figures 2.5(a) and 2.5(b) show the output of a passive MLL with a center wavelength of 1560 nm and a repetition rate of 250 MHz [12]. The MLL has a pulse width of 185 fs and a of 14 nm corresponding to approximately 1.7 THz. Such high bandwidths are much more than what electronic circuits can achieve.

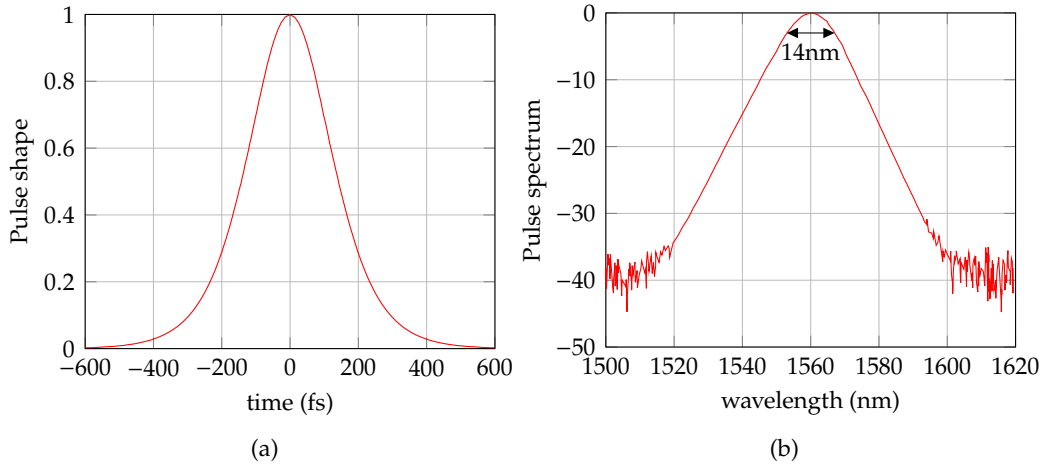


FIGURE 2.5: Measured MLL pulse in (a) time and (b) frequency domain [12]; traces are normalized to maximum; time domain trace is from autocorrelator output.

2.3 Properties of mode-locked laser signals

The extremely high bandwidth available in the optical domain, compared to the electrical domain, has paved the way for subpicosecond and even femtosecond pulse widths. The mathematical formalism provided in the previous sections describes the complex amplitude of the optical pulse generated in MLLs. However, the relation between the amplitude and phase of the generated combines still needs to be addressed. This is an important question in the theory of MLL, since the relation between these combines is the key to describe the relation between their amplitude and phase noise. The power spectral density (PSD) of various MLL noise mechanisms has been well studied in the literature [73–75] and here we only try to add these noise mechanisms to MLL optical pulse at an abstract level. In order to achieve this goal, first the complex amplitude of the optical pulse train is modeled and its Fourier transform is calculated. Using the complex amplitude of the pulse train, the

MLL optical pulse field is derived. After this step, the relevant noise terms are included and the amplitude and phase of individual comb lines are derived. The result expresses the noise of individual MLL comb lines and their different noise terms.

The Fourier transform of the complex amplitude of the MLL pulse can be written as

$$\tilde{E}(\omega) = \mathcal{F}\{\tilde{e}(t)\} = \frac{1}{2\pi} \int_{-\infty}^{\infty} dt \tilde{e}(t) e^{-j\omega t}, \quad (2.21)$$

where $\mathcal{F}\{\}$ denotes the Fourier transform and $\tilde{e}(t)$ is the complex amplitude of the pulse. Note that $\tilde{e}(t)$ is generally a complex-valued function and thus $\tilde{E}(\omega)$ does not necessarily have Hermitian symmetry. The complex amplitude of the output pulse train of MLL can be written as

$$\tilde{e}(t, T_R) = \sum_{m=-\infty}^{\infty} \tilde{e}(t - mT_R). \quad (2.22)$$

If we assume the temporal overlap of optical pulses can be neglected, $|\tilde{e}(T_R)| \ll |\tilde{e}(0)|$, the Fourier series coefficients of the complex amplitude of the optical pulse train e_k can be written as

$$e_k = \frac{1}{T_R} \int_{-T/2}^{T/2} dt \tilde{e}(t, T_R) e^{-jk\omega_R t} = \frac{2\pi}{T_R} \tilde{E}(k\omega_R), \quad (2.23)$$

where $\omega_R = 2\pi/T_R$. The electric field of the optical pulse train in the time domain can be calculated using its complex amplitude as

$$E(t) = \text{Re} \left\{ \tilde{e}(t, T_R) e^{j\omega_c t} \right\}, \quad (2.24)$$

where $\text{Re}\{\}$ denotes the real part of a complex number and ω_c is the optical carrier angular frequency. Equations (2.21) to (2.24) can be used to find the electric field of individual comb lines and their relative phases. Now we add the phase noise terms to the optical pulse train in (2.24). The phase noise of the pulse train on the one hand originates from the cavity length fluctuations which affect the timing of the optical pulse trains, and on the other hand is due to the line shape of the optical carrier. Therefore, two different noise terms are added to (2.24) as

$$E(t) = \text{Re} \left\{ \sum_{m=-\infty}^{\infty} \tilde{e} \left(t - mT_R + \frac{T_R}{2\pi} \phi_{n,R}(t) \right) e^{j\omega_c t + j\phi_{n,ceo}(t)} \right\}, \quad (2.25)$$

where $\phi_{n,R}(t)$ is the phase noise due to cavity length fluctuations and $\phi_{n,ceo}$ is the phase noise of the optical carrier. The repetition rate phase noise $\phi_{n,R}(t)$ is normalized by a factor of $T_R/2\pi$ to convert phase noise to timing jitter. Using the Fourier series expansion of the complex amplitude in (2.23), the electric field of the optical pulse train can be written as

$$\begin{aligned} E(t) &= \text{Re} \left\{ \sum_{k=-\infty}^{\infty} e_k e^{jk\omega_R t + jk\phi_{n,R}(t)} e^{j\omega_c t + j\phi_{n,ceo}(t)} \right\} \\ &= \sum_{k=-\infty}^{\infty} |e_k| \cos \left((k\omega_R + \omega_c)t + \phi_k + k\phi_{n,R}(t) + \phi_{n,ceo}(t) \right), \end{aligned} \quad (2.26)$$

where

$$\phi_k = \arctan\left(\frac{\text{Im}\{e_k\}}{\text{Re}\{e_k\}}\right), \quad (2.27)$$

and $\text{Re}\{\}$ & $\text{Im}\{\}$ denote the real part & imaginary part of a complex number, respectively. Equation (2.26) is known as the elastic tape theory [75]. It shows the relation between the frequency of different comb lines as well as their phase noise. The smallest k such that $k\omega_R + \omega_c$ is a positive angular frequency corresponds to the so-called carrier envelope offset (CEO) angular frequency

$$k_{\min} = \left\lceil \frac{\omega_c}{\omega_R} \right\rceil, \quad (2.28)$$

where $\lceil \cdot \rceil$ denotes the mathematical ceiling function. The carrier envelope offset angular frequency ω_{ceo} can then be written as

$$\omega_{\text{ceo}} = \omega_c - \left\lceil \frac{\omega_c}{\omega_R} \right\rceil \omega_R. \quad (2.29)$$

The electric field given in (2.26) can have as many as infinite number of comb lines. One must keep in mind that the above approach is purely mathematical and many of these comb lines lie outside the wavelength range in which the laser is capable of generating light. The CEO frequency is in the microwave frequency range and is not a physically generated comb line. It is used conventionally to express the frequency of the individual comb lines with respect to it. Neglecting the terms with a negative frequency, the frequency of the k^{th} comb line can be written with respect to ω_{ceo} as

$$\omega_{k'} = \omega_{\text{ceo}} + k'\omega_R \quad k' > 0. \quad (2.30)$$

The overall phase noise of the k^{th} comb line can also be written as

$$\phi_{n,k'}(t) = \phi_{n,\text{ceo}}(t) + k'\phi_{n,R}(t). \quad (2.31)$$

Therefore, the phase noise of individual comb lines can be expressed in terms of repetition rate phase noise and CEO phase noise. Equation (2.31) goes beyond modeling the phase noise of the MLL intensity waveform, and is of basic importance for stabilization techniques that stabilize two individual comb lines of the MLL.

The elastic tape theory has been shown to be valid using the perturbation theory and is also verified by experiment [75, 76]. The correlation between the frequency and phase noise of the individual comb lines is the key to measure CEO frequency using the Nobel prize winning $f - 2f$ interferometry technique. This technique connected the measurement of optical and microwave frequencies and paved the way for optical frequency metrology [57–59].

2.4 $f - 2f$ interferometry

The optical frequencies are at least two orders of magnitude higher than the microwave frequencies. The gap between microwave and optical frequencies cannot be easily filled due to lack of components operating in the THz frequency range. One might try to measure an optical frequency relative to another optical frequency where their frequency difference lies in the microwave range, however, the absolute value

of the optical frequency still remains unknown. The advent of high-energy coherent pulses with extremely wide spectral combs helped to solve this problem using the gold-standard $f - 2f$ interferometry technique. The operating principle of this technique is illustrated graphically in Figure 2.6(a).

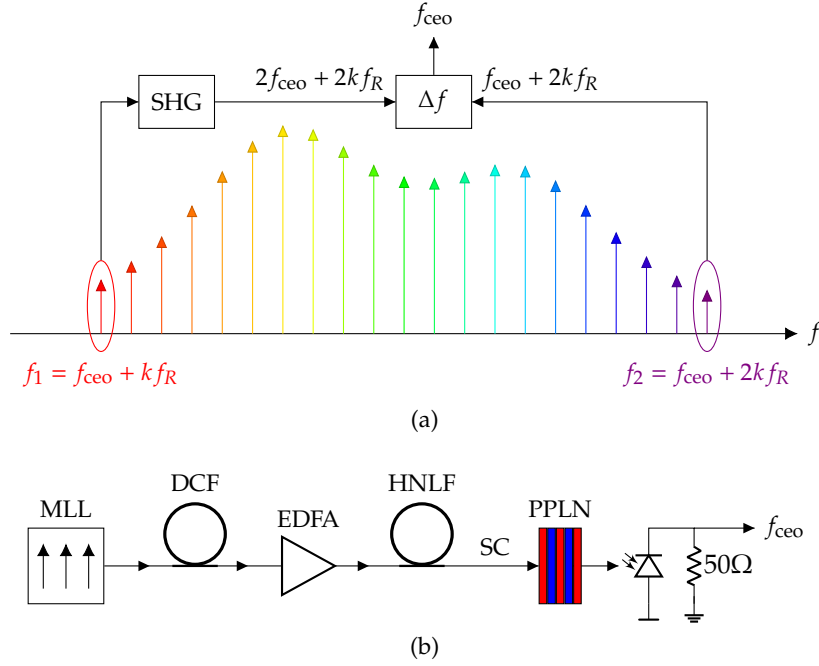


FIGURE 2.6: (a) Illustration of $f - 2f$ interferometry operating principle and (b) block diagram of an $f - 2f$ interferometry implementation (adopted from [77]). DCF, dispersion compensation fiber; EDFA, Erbium-doped fiber amplifier; HNLF, highly nonlinear fiber; SC, supercontinuum; PPLN, periodically poled lithium niobate; SHG, second harmonic generation.

In order to explain the principle of $f - 2f$ interferometry, we assume the MLL spectral lines cover an octave of bandwidth, a so-called supercontinuum (SC). The frequency of one of the comblines at the lower end of the frequency can be written as

$$f_1 = f_{\text{ceo}} + kf_R, \quad (2.32)$$

and the frequency of one of the comblines at the higher end of the frequency range is

$$f_2 = f_{\text{ceo}} + 2kf_R. \quad (2.33)$$

The combline with the lower frequency is applied to a second harmonic generation (SHG) crystal and its frequency difference with the combline with the higher frequency is detected, which is the CEO frequency. This is an elegant technique which can be used to determine the frequency of every single spectral line with very high precision.

Figure 2.6(b) shows an implementation of $f - 2f$ interferometric setup [77]. In order to generate supercontinuum, the optical pulses of MLL are first amplified using an Erbium-doped fiber amplifier (EDFA) to reach high pulse energy levels. A dispersion compensation fiber (DCF) is placed before the amplifier to compensate

for its dispersion. The high energy pulses then drive a highly nonlinear fiber (HNLF) and generate a supercontinuum optical pulse. Applying this optical pulse to a periodically poled lithium niobate (PPLN) generates the second harmonic of the comb, among them f_1 in (2.32). The output of PPLN includes both leakage of f_2 and the second harmonic of f_1 . Photodetection of the PPLN output then discriminates f_{ceo} .

2.4.1 Optical frequency division

An important application of $f - 2f$ interferometry is generation of extremely low phase noise optical pulses synchronized to a precise CW optical reference, a so-called optical frequency division (OFD) technique. This can be explained by rearranging (2.31) as

$$\phi_{n,R}(t) = \frac{1}{k} [\phi_{n,k}(t) - \phi_{n,\text{ceo}}(t)] . \quad (2.34)$$

Since the optical frequencies are at least 3 orders of magnitude higher than microwave frequencies, using (2.30) k is approximated as

$$k \approx \frac{f_k}{f_R} . \quad (2.35)$$

If the phase noise of CEO is sufficiently below that of the k^{th} combline, then the noise properties of the k^{th} combline are transferred to the repetition rate by the rule of an ideal frequency divider

$$\phi_{n,R}(t) \approx \frac{f_R}{f_k} \phi_{n,k}(t) . \quad (2.36)$$

This relation is the key to generation of extremely low noise clock signals using the optical frequency division (OFD) technique. In this technique, on the one hand the k^{th} combline is locked to an ultralow noise optical reference and on the other hand, f_{ceo} is stabilized to a microwave reference.

Figure 2.7 shows the effect of stabilization on the phase noise of a commercial MLL [77]. The phase noise of non-stabilized f_{ceo} is up to 6 orders of magnitude higher than that of an ultralow noise optical reference (from Menlo Systems). Although the stabilization has improved the f_{ceo} noise at offset frequencies below 10 kHz, it has not provided sufficient suppression of f_{ceo} noise and it is still higher than the phase noise of the ultrastable laser. For a perfect division, one has to sufficiently suppress the CEO noise such that $\phi_{n,\text{ceo}}$ in (2.34) can be neglected and consequently (2.36) holds.

2.5 Summary and conclusion

In this chapter, we looked at the operating principle of mode-locked lasers and the properties of their output signals. A basic understanding of MLL is necessary for the generation of low noise microwave signal from optical pulses of MLLs. The active MLL uses a modulator to incorporate a time-dependent loss in the laser cavity and shape the optical pulse. Since the modulator is excited with an external periodic signal, the noise properties of active MLL are determined by the noise properties of the excitation signal. Therefore, active MLLs have similar phase noise performance to quartz and SAW oscillators. In contrast, passive MLLs use a nonlinear element in

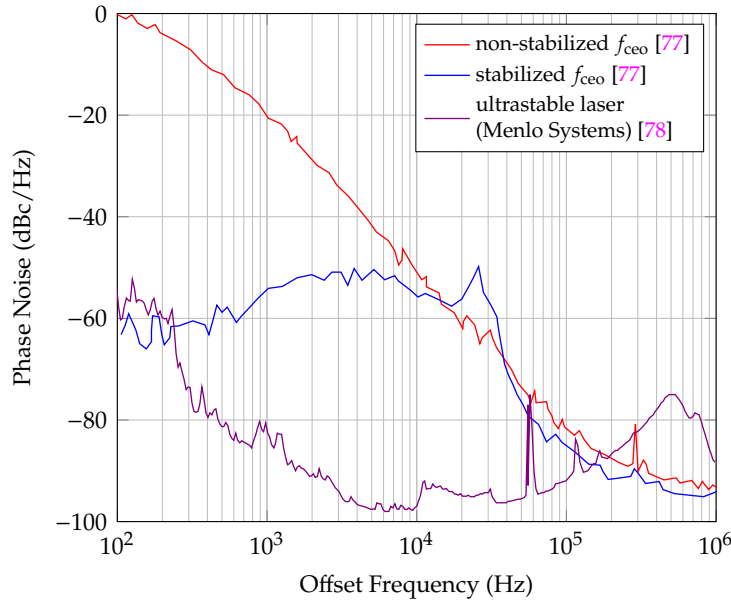


FIGURE 2.7: (red) Phase noise of non-stabilized f_{ceo} of an MLL, (blue) phase noise of stabilized f_{ceo} of the same MLL [77] and (violet) phase noise of an ultrastable cavity laser at 1542 nm [78].

the laser cavity to shape the optical pulse and the phase noise of the generated optical pulse becomes a function of the geometry of the cavity and material properties of its components. Consequently passive MLLs have been optimized to have better phase noise by orders of magnitude compared to quartz and SAW oscillators.

The phase noise of MLL intensity waveform is transferred to the OEPLL (inside loop bandwidth) and therefore improvement of MLL phase noise directly affects the phase noise of the generated RF signal. As we will see later, for the OEPLL it is necessary to just model the intensity of these optical pulses. However, improvement of the phase noise of the intensity waveform depends on the stabilization technique. The state-of-the-art stabilization technique known as optical frequency division requires more information than just the intensity of the optical pulses and modeling the optical field of individual comblines is necessary. In addition, some RF generation techniques such as heterodyne mixing also require this modeling. The theory of MLLs and optical-domain modeling of MLL pulses open the way for more innovative techniques for microwave signal generation based on MLLs.

Chapter 3

Theory of Optoelectronic Phase-Locked Loop

In previous chapters the theory of MLL and different RF generation techniques have been discussed. It was shown that among different MLL-based RF generation methods, the OEPLL is best suited for versatile RF frequency synthesis. In this chapter, we provide a detailed analysis of the OEPLL. First, an abstract model of PLL is presented which is then analyzed at system level. This abstract model is then adapted to OEPLL concept. In order to provide the component level specifications required for this system level analysis, the BOMPD has to be characterized. Therefore, the governing equations of BOMPD are derived and the behavior of BOMPD in dynamics of OEPLL is discussed. It is noteworthy that the theory presented in this chapter has been published in high-ranked journals and conferences [author's publication, 18, 53, 54].

3.1 Generic theory of phase-locked loop

Figure 3.1 shows the generic diagram of a PLL at an abstract level. For our phase noise discussions, we also include relevant noise sources to this abstract model. Now we provide a mathematical model for signals and various blocks of Figure 3.1.

Reference signal The PLL reference input is a sinusoidal signal

$$x_R(t) = x_0 \cos(\omega_0 t + \phi_0 + \phi_{n,R}(t)), \quad (3.1)$$

where x_0 is its amplitude, ω_0 is its angular frequency, ϕ_0 is its offset phase and $\phi_{n,R}(t)$ is its phase noise.

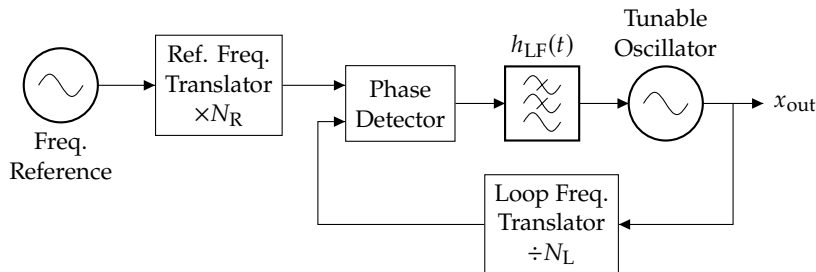


FIGURE 3.1: Generic block diagram of phase-locked loop.

Frequency translators The PLL requires equal frequencies at the inputs of the phase detector to phase-lock the tunable oscillator to the reference. In order to match these frequencies, the frequency of the reference should match the frequency of the tunable oscillator. This is realized by using frequency translators in the reference

path and the feedback path. Both these frequency translators are included in our model in Figure 3.1 and their effect on the phase noise will be compared. We assume ideal noiseless frequency translators without additive noise and insensitive to their input amplitude. The transfer characteristic of the frequency translator $T_N\{\cdot\}$ can therefore be written as

$$T_N\{x_1 \cos(\phi(t))\} = a_N \cos(N\phi(t)) \quad (3.2)$$

where N is the frequency translation factor, ϕ is the instantaneous phase of the input signal, x_1 is the amplitude of the input signal and a_N is the amplitude of the output signal. Although an ideal frequency translator does not add any noise to the original signal, the phase noise of the original signal is boosted by the frequency translation factor, N , and if the PSD of the phase noise is concerned, the PSD is boosted by a factor of N^2 . Note that this noise is not additive and if another frequency translator with a translation factor of $1/N$ is used to recover the signal, the original signal with its phase noise is restored.

Phase detector The phase detector generates an output that is proportional to the instantaneous phase difference between its inputs. The phase detector output is then filtered and generates an error signal which aligns the tunable oscillator phase with the reference phase. We assume the phase detector properties are insensitive to its input levels, but we incorporate its noise in our model. The phase detector characteristic function $T_{PD}\{\cdot\}$ consequently can be written as

$$T_{PD}\{x_1 \cos(\phi_1(t)), x_2 \cos(\phi_2(t))\} = K_\phi(\phi_1(t) - \phi_2(t) + \phi_{n,PD}(t)), \quad (3.3)$$

where x_1 and x_2 are the amplitudes of the phase detector inputs, ϕ_1 and ϕ_2 are the instantaneous phase of the inputs, K_ϕ is the phase detector gain and $\phi_{n,PD}$ is the noise of the phase detector.

Tunable Oscillator The tunable oscillator generates a sinusoidal waveform whose instantaneous frequency is proportional to its input tuning voltage. Since the instantaneous phase of a sinusoidal signal is equal to the integral of its instantaneous frequency, transfer characteristic of the tunable oscillator can be modeled as

$$T_{TO}\{x_1(t)\} = x_{TO} \cos\left(\omega_0 t + \phi_{n,TO}(t) + K_V \int dt x_1(t)\right), \quad (3.4)$$

where x_1 is the input signal of the tunable oscillator, ω_0 is its nominal angular frequency, x_{TO} is its amplitude, K_V is its tuning sensitivity and $\phi_{n,TO}$ is its phase noise. We also assumed that the oscillation amplitude x_{TO} is independent of the input tuning voltage $x_1(t)$.

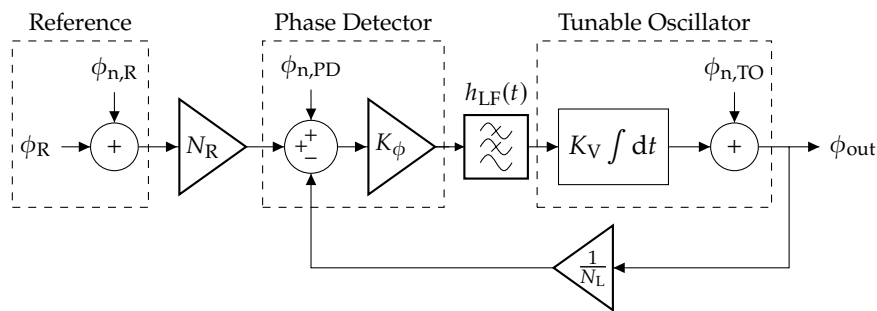


FIGURE 3.2: Linear model of phase-locked loop in the phase domain.

Under these assumptions, the nonlinear blocks of PLL can be linearized in the phase domain as illustrated in 3.2. Using linear control theory mathematical toolbox, the open loop transfer function of the PLL is defined as the transfer function of all loop components multiplied

$$H_{OL}(s) := \frac{1}{N_L} K_\phi H_{LF}(s) \frac{K_V}{s}, \quad (3.5)$$

where $H_{LF}(s)$ is the Laplace transform of loop filter impulse response $h_{LF}(t)$. It can be seen that $H_{OL}(s)$ is inversely proportional to the loop division factor N_L which consequently affects all loop parameters. This reduction of gain can be compensated by a higher gain for the loop filter or higher phase detector gain. Therefore, for comparing the effect of different frequency translators on the PLL phase noise, we assume H_{OL} is designed for a fixed loop bandwidth and phase margin, and the open loop gain is compensated by a proper loop design and is independent of loop division factor.

Now we look at the loop filter requirements. An interesting choice for the loop filter is an integrator with a transfer function of

$$H_{LF}(s) = \frac{s_0}{s}. \quad (3.6)$$

This type of loop filter has practical advantages. It results in an infinite steady-state gain for the loop filter and an average-zero error signal at the phase detector output, regardless of the level of the dc signal required by the tunable oscillator. This is especially interesting since in practice phase detector transfer characteristic is dependent on its output operating point and it is desired to operate the phase detector around a certain point. Although the loop filter transfer function in (3.6) has practical advantages, an ideal integrator as the loop filter makes the loop unstable. This problem can be solved by placing a zero at the loop filter transfer function

$$H_{LF}(s) = \frac{\kappa s + s_0}{s}. \quad (3.7)$$

where κ is a constant. Placing this zero is usually realized by a simple series RC-circuit or using an operational amplifier. We now define the closed-loop transfer function as

$$H_{CL}(s) := \frac{H_{OL}(s)}{1 + H_{OL}(s)}. \quad (3.8)$$

This definition simplifies other transfer functions of the system with respect to different inputs and is especially beneficial in understanding how different noise sources affect the overall phase noise. In this discussion, we assume the PLL is stable and limit the scope of our analysis to offset frequencies sufficiently above and below the loop cut-off frequency. Further details on the stability of the loop can be found in the reference books [19, 79]. The open loop and closed-loop transfer functions, $H_{OL}(s)$ and $H_{CL}(s)$, are plotted in Figure 3.3. On the one hand, at frequencies well below the loop cut-off frequency $H_{OL}(s)$ diverges to infinity and it causes $H_{CL}(s)$ to converge to 1. On the other hand, at frequencies well above the loop cut-off frequency $H_{OL}(s)$ converges to 0 and it causes $H_{CL}(s)$ to also converge to 0. These behaviors at low and high frequencies can also directly be observed in equations (3.5) and (3.8), assuming the loop filter has the transfer function given in (3.7).

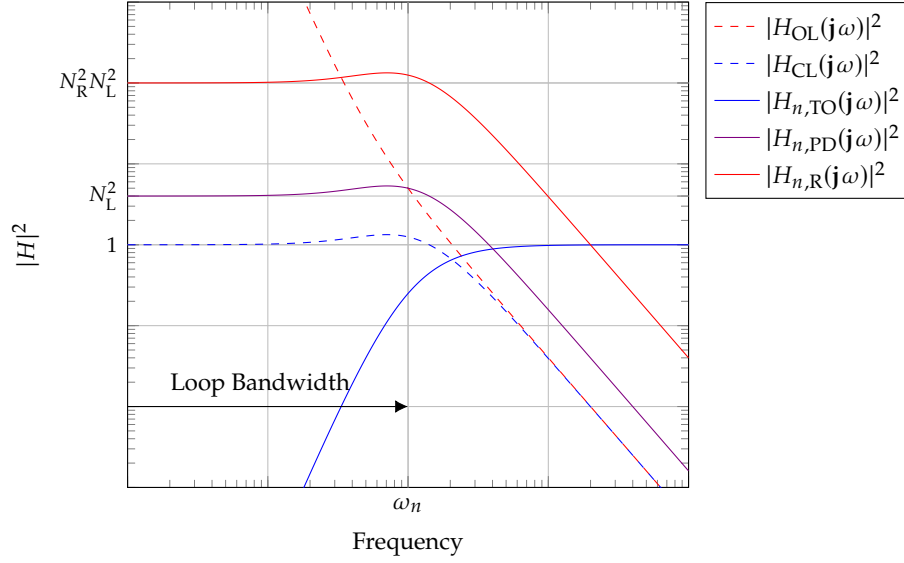


FIGURE 3.3: Open loop and closed-loop transfer functions of PLL in logarithmic scale.

TABLE 3.1: Behavior of different PLL transfer functions at close-in and far offset frequencies.

	H_{OL}	H_{CL}	$H_{n,R}$	$H_{n,PD}$	$H_{n,TO}$
$\omega = 0$ (inside loop)	∞	1	$N_R N_L$	N_L	0
$\omega \rightarrow \infty$ (outside loop)	0	0	0	0	1

Now we derive the phase transfer functions. The closed-loop transfer function of the output phase to the reference input phase can be written as

$$\frac{\Phi_{out}}{\Phi_R}(s) = N_R N_L \frac{H_{OL}(s)}{1 + H_{OL}(s)} = N_R N_L H_{CL}(s), \quad (3.9)$$

where Φ_R is the reference phase in the Laplace domain. The closed-loop transfer function of the noise sources can also be found as

$$H_{n,R}(s) = \frac{\Phi_{out}}{\Phi_{n,R}}(s) = N_R N_L H_{CL}(s), \quad (3.10)$$

and

$$H_{n,PD}(s) = \frac{\Phi_{out}}{\Phi_{n,PD}}(s) = N_L H_{CL}(s). \quad (3.11)$$

The transfer function of the output phase to the tunable oscillator phase noise can also be written in terms of the open-loop transfer function

$$H_{n,TO}(s) = \frac{\Phi_{out}}{\Phi_{n,TO}}(s) = \frac{1}{1 + H_{OL}(s)} = 1 - H_{CL}(s). \quad (3.12)$$

In our equations, we used small letters such as h and ϕ for time domain signals and capital letters such as H and Φ for Laplace domain signals.

Now we look at the shapes of these transfer functions, plotted in Figure 3.3, to

see how they affect the output signal phase noise. On the one hand, the noise of the reference and the phase detector are effective inside the loop bandwidth and are suppressed outside it. The tunable oscillator noise, on the other hand, is transferred to the output outside the loop bandwidth and is suppressed inside it. In addition, the reference noise inside the loop bandwidth is transferred to the output by a scaling factor equal to the overall frequency translation factor, $N_R N_L$. So at offset frequencies inside the loop bandwidth, $H_{n,R}(s)$ operates like an ideal frequency translator. Finally, the phase detector noise is scaled by the loop frequency translation factor N_L . This is one of the most important results of this analysis. It shows that in order to minimize the phase detector noise, the loop frequency divider should be avoided. While using a loop frequency divider is very popular in low cost PLLs, high performance laboratory grade instruments avoid it at the cost of higher overall system complexity. Table 3.1 summarizes the behavior of the PLL transfer functions at close-in and far offset frequencies.

3.2 Dynamics of optoelectronic phase-locked loop

So far, a generic theory to analyze the PLL has been presented. In this section we adapt this theory to optoelectronic phase-locked loop (OEPLL). A simplified block diagram of the OEPLL is shown in Figure 3.4(a). The tunable oscillator signal is in the electrical domain and the frequency reference is the MLL optical output. Therefore, the phase detector is required to operate in a mixed electro-optical domain, a so-called balanced optical microwave phase detector (BOMPD). The BOMPD is implemented by means of a balanced intensity modulator (BIM) which can be a balanced Mach-Zehnder modulator (MZM) or a Sagnac loop, as they both have similar transfer characteristics. The optical pulses of the MLL are intensity-modulated with the RF signal from the tunable oscillator, as illustrated in Figure 3.4(b). The modulator has two optical outputs with complementary intensities. The optical outputs of the modulator are converted to electrical currents with a pair of photodiodes and these currents are subtracted via the balanced configuration of the photodiodes. This current is then integrated at the loop filter to generate an error voltage which aligns the phase of the tunable oscillator with the phase of the envelope of the optical reference signal.

The intensities of the BIM outputs are equal when the RF signal is phase-aligned with the envelope of the optical reference, as illustrated in Figure 3.4(b) with solid red and blue colors. Therefore, when the OEPLL is phase-locked, the current difference of the pair of photodiodes will be zero. Consequently, the applied voltage to the tunable oscillator will not change and its phase is stabilized. Any change in the phase difference causes an unbalance between the output intensities of the BIM as illustrated in Figure 3.4(b) with the dashed and dotted blue and red optical pulses. These optical pulses generate a non-zero current difference in the pair of the photodiodes. This current difference can be considered as an error current which is integrated by the loop filter and realigns the tunable oscillator phase.

The optical pulses of MLLs have sub-picosecond widths which correspond to hundreds of gigahertz spectral widths. The intensity of these waveforms is therefore harmonic rich with at least hundreds of gigahertz bandwidth. Therefore, by using such a harmonic rich waveform, the reference repetition rate has already the harmonics which were generated via the reference frequency translator in our model in Figure 3.1. Since the OEPLL can potentially lock on any of the available reference

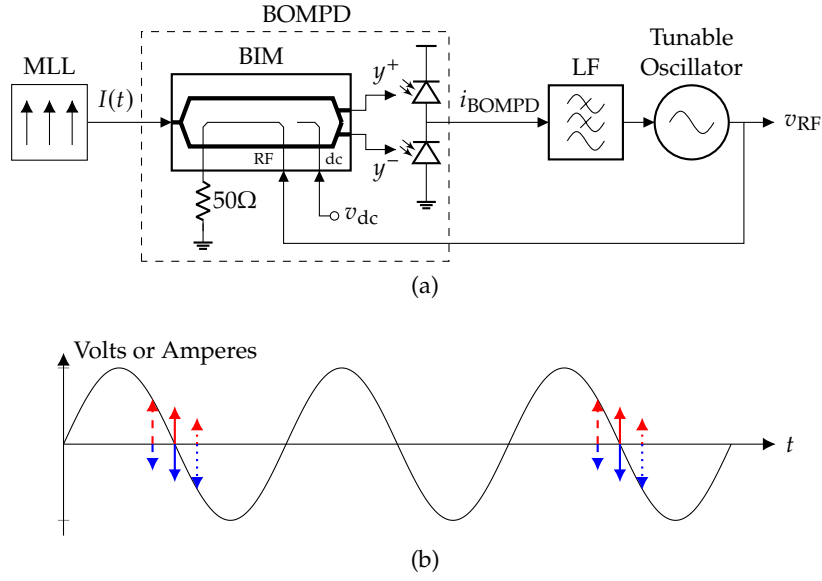


FIGURE 3.4: (a) Simplified block diagram of the OEPLL and (b) corresponding waveforms: (black) voltage waveform at the RF port of BIM, (red) upper photodiode current and (blue) lower photodiode current when (solid) the phase of RF signal and the optical intensity are aligned, (dashed) the optical intensity has a phase lead and (dotted) the optical intensity has a phase lag.

harmonics, pre-tuning of the tunable oscillator around the desired frequency is necessary. Similar to the block diagram of the generic PLL, the block diagram of OEPLL in the phase domain is illustrated in Figure 3.5(a). The optical paths are drawn in blue and electrical paths in black.

The BOMPD outputs current pulses from the pair of photodiodes and the tunable oscillator usually requires a voltage as its tuning output. So, the phase detector gain has units of A/Rad and the loop filter transfer function has units of Ohm. The simplest approach to implement a loop filter with a zero in its transfer function as (3.7) is the series RC circuit illustrated in Figure 3.5(b). The filter transfer function simply is

$$H_{LF}(s) = \frac{R_1 C_1 s + 1}{C_1 s} . \quad (3.13)$$

With this transfer function, the open loop transfer function can be written as

$$H_{OL}(s) = \frac{K_V K_\phi (R_1 C_1 s + 1)}{C_1 s^2} , \quad (3.14)$$

and the closed-loop transfer function as

$$H_{CL}(s) = \frac{K_V K_\phi (R_1 C_1 s + 1)}{C_1 s^2 + K_V K_\phi (R_1 C_1 s + 1)} . \quad (3.15)$$

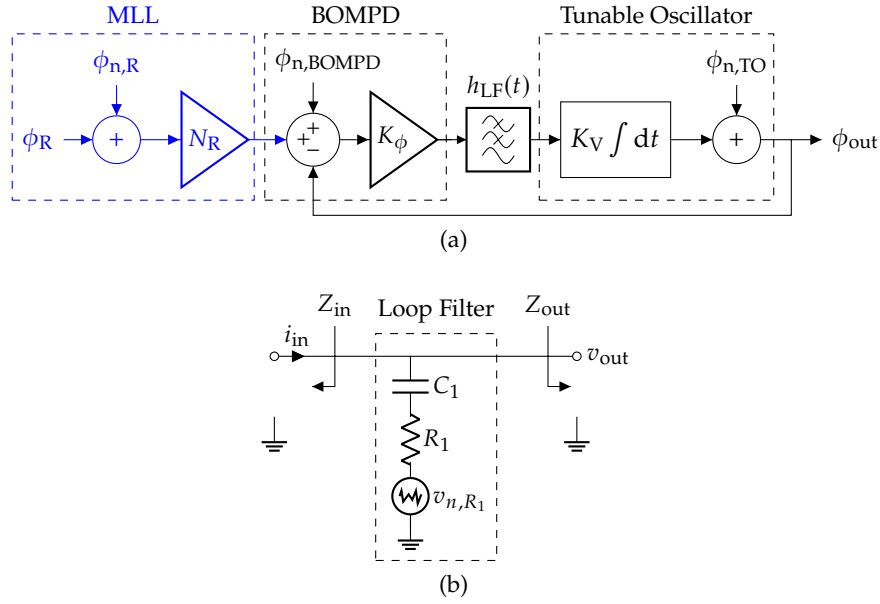


FIGURE 3.5: (a) Linear model of the optoelectronic phase-locked loop in the phase domain. (b) OEPLL loop filter including the resistor thermal noise.

Using this closed loop transfer function, the *natural angular frequency* (ω_n) and the *damping factor* (ζ) can be found as

$$\omega_n = \sqrt{\frac{K_V K_\phi}{C_1}}, \quad (3.16)$$

and

$$\zeta = \frac{1}{2} R_1 \sqrt{K_V K_\phi C_1}. \quad (3.17)$$

The closed-loop transfer function can be rewritten in a more familiar form

$$H_{CL}(s) = \frac{2\zeta\omega_n(s + \frac{\omega_n}{2\zeta})}{s^2 + 2\zeta\omega_n s + \omega_n^2}. \quad (3.18)$$

The closed-loop transfer function can consequently be used to set the desired loop parameters such as the loop bandwidth and phase margin. The desired loop filter components for a given natural frequency and damping factor can also be calculated

$$C_1 = \frac{K_V K_\phi}{\omega_n^2}, \quad (3.19)$$

and

$$R_1 = \frac{2\zeta\omega_n}{K_V K_\phi}. \quad (3.20)$$

In Chapter 2 we showed that the phase noise of MLLs can be below the phase noise of quartz and SAW oscillators by orders of magnitude. For fully electronic PLLs usually the reference phase noise is the theoretical limiting factor. In contrast,

in OEPLLs, where optical reference noise might no longer be the limiting factor, other noise sources can make a great contribution to overall phase noise. Here we only adapt a system level point of view and consider the resistor thermal noise. Although the resistor noise is not problematic for many typical PLL designs, it can affect the overall phase noise of a ultra-low phase noise OEPLL. Other noise sources are covered in Section 4.1.

Now the transfer function of the thermal noise of the resistor is derived. The contribution of the resistor voltage noise, v_{n,R_1} , to the output voltage is a function of the source and load impedances of the loop filter, Z_{in} and Z_{out} , respectively. It is a fair assumption to consider the impedances of the photodiodes and the tuning input of the tunable oscillator to be sufficiently high at frequencies below a few megahertz — which is the range of interest for analysis of loop dynamics. Therefore, the thermal noise voltage of the resistor is transferred to the node v_{out} with unity transfer function. The overall transfer function of this noise voltage to the output then is

$$H_{n,R_1}(s) = \frac{\Phi_{out}}{V_{n,R_1}}(s) = \frac{K_V s}{s^2 + 2\zeta\omega_n s + \omega_n^2}. \quad (3.21)$$

This transfer function has a bandpass shape, and the resistor noise is suppressed at frequencies well below and above loop cut-off frequency. Taking to account the PSD of the resistor thermal noise, $4kTR_1$, its contribution to the overall phase noise, $S_{\phi_{out},R_1}(f)$, can be written as

$$S_{\phi_{out},R_1}(f) = \frac{4kTR_1 K_V^2 \omega^2}{|\omega^2 + 2j\zeta\omega_n \omega + \omega_n^2|^2}, \quad (3.22)$$

where j is the unit imaginary number $\sqrt{-1}$, k is the Boltzmann's constant, T is absolute temperature and $\omega = 2\pi f$. Substituting the resistance value in (3.20) to the PSD of (3.22) results in

$$S_{\phi_{out},R_1}(f) = \frac{8kTK_V \zeta \omega_n \omega^2}{K_\phi |\omega^2 + 2j\zeta\omega_n \omega + \omega_n^2|^2}, \quad (3.23)$$

The contribution of the loop filter resistor thermal noise to the overall phase noise is proportional to K_V and inversely proportional to K_ϕ . The resistor thermal noise shows its effect as a bump around the loop cut-off frequency and in order to suppress it, phase detector gain K_ϕ can be increased or tunable oscillator tuning sensitivity K_V can be decreased.

3.3 Characteristic function of BOMPD

In the previous section, we derived the relevant characteristic functions of the OEPLL. From a system level perspective, we assumed the OEPLL phase detector, the BOMPD, has a linear gain of K_ϕ . In this section, we determine the BOMPD gain with respect to the specifications of its building blocks and its inputs.

One must keep in mind that the BOMPD operates in a mixed electro-optical domain, as its reference input is in the optical domain and its RF input as well as its output current are in the electrical domain. The BOMPD characteristic function describes its output current, the photocurrent of the pair of photodiodes, versus the phase difference between its inputs, the RF signal applied to BIM and the intensity of

the optical input. The linear phase detector gain, which is required for the analysis of the OEPLL in the phase domain, is then the slope of the characteristic function.

A simplified block diagram of OEPLL is shown in Figure 3.4(a). The intensities of the optical outputs of a loss-less MZM, I_y^+ and I_y^- , as a function of its optical input and the optical phase shift introduced by the modulation voltages can be written as (the derivation steps are given in the Appendix C.)

$$I_y^\pm = \frac{I(t)}{2} [1 \pm \sin(\psi)] , \quad (3.24)$$

where $I(t)$ is the optical cycle averaged intensity of the optical input and ψ is the total optical phase shift in the modulator arms. The phase shift ψ is proportional to the dc and the RF modulation voltages

$$\psi = \psi_{\text{RF}} + \psi_{\text{dc}} = \frac{v_{\text{RF}}\pi}{V_{\pi,\text{RF}}} + \frac{v_{\text{dc}}\pi}{V_{\pi,\text{dc}}} , \quad (3.25)$$

where ψ_{dc} is the optical phase shift introduced by the dc electrode, ψ_{RF} is the optical phase shift introduced by the RF electrode, $V_{\pi,\text{dc}}$ is the π -voltage of the dc electrode, $V_{\pi,\text{RF}}$ is the π -voltage of RF electrode, v_{dc} is the bias voltage at the dc electrode and v_{RF} is the RF modulation voltage.

The MLL output is periodic and its output intensity can be formulated as

$$I(t) = I_0 T_R \sum_{m=-\infty}^{+\infty} P\left(t - \frac{m}{f_R}\right) , \quad (3.26)$$

where I_0 is the average optical intensity of the MLL output, T_R is the period of $I(t)$, f_R is the frequency of $I(t)$ and $P(t)$ is the energy-normalized pulse shape such that

$$\int_{-T_R/2}^{+T_R/2} dt P(t) = 1 . \quad (3.27)$$

The optical pulses of the low noise MLLs have typically sub-picoseconds widths. Such low pulse widths correspond to bandwidths of at least hundreds of gigahertz which are much more than the bandwidth of many RF systems such as frequency synthesizers. Therefore, it is a good approximation to consider the intensity of MLL pulses as Dirac delta pulses, $P(t) \approx \delta(t)$. This assumption significantly simplifies the Fourier series expansion of the intensity waveform as

$$\begin{aligned} I(t) &= I_0 T_R \sum_{m=-\infty}^{+\infty} \delta\left(t - \frac{m}{f_R}\right) \\ &= I_0 \left[1 + 2 \sum_{k=1}^{+\infty} \cos(k\omega_R t) \right] . \end{aligned} \quad (3.28)$$

We assume single tone excitation of the RF electrode with an angular frequency of ω_{RF} , an amplitude of V_{RF} , and an offset phase of ϕ ,

$$v_{\text{RF}} = V_{\text{RF}} \sin(\omega_{\text{RF}} t + \phi) . \quad (3.29)$$

The output differential intensity ΔI_y which corresponds to the output current of the photodetectors pair i_{BOMPD} in Figure 3.4(a) is defined as

$$\Delta I_y := I_y^+ - I_y^- = I(t) \sin(\psi) . \quad (3.30)$$

We call $\psi_{\text{dc}} = 0$ as the *odd symmetry point* and $\psi_{\text{dc}} = \pm\pi/2$ as the *even symmetry points*, since $\Delta I_y(v_{\text{RF}})$ has odd and even symmetry versus v_{RF} around these points, respectively.

The characteristic function of the BOMPD is defined as its average output current as a function of the phase difference between the RF signal and the MLL desired harmonic

$$H(\phi) = \langle i_{\text{PD}}^+ - i_{\text{PD}}^- \rangle , \quad (3.31)$$

where $\langle . \rangle$ denotes temporal averaging and i_{PD}^+ & i_{PD}^- are the upper & lower photodiode currents, respectively. Now we assume the photodetectors in Figure 3.4(a) are linear with infinite bandwidth. This assumption significantly simplifies our derivations. In practice, the loop bandwidth of the OEPLL is in megahertz range and the photodiode bandwidth is at least a few hundreds of megahertz and the photodiode bandwidth does not affect the OEPLL performance. For the sake of a perfect analysis, we will consider the photodiode bandwidth in our photodiode noise calculations in Section 4.1. The BOMPD characteristic function can now directly be related to the BOMPD output differential intensity as

$$\begin{aligned} H(\phi) &= \langle i_{\text{PD}}^+ - i_{\text{PD}}^- \rangle \\ &= \langle R_\lambda I_y^+ - R_\lambda I_y^- \rangle \\ &= R_\lambda \langle \Delta I_y \rangle , \end{aligned} \quad (3.32)$$

where R_λ is the photodiode responsivity.

Combining (3.30) and (3.29), one can see that in low V_{RF} regime ($V_{\text{RF}} \ll V_{\pi, \text{RF}}$) and zero dc phase shift ($\psi_{\text{dc}} = 0$), the balanced MZM operates as a balanced electro-optical mixer and multiplies the intensity of the optical signal by the RF modulation amplitude. In this regime, the differential output intensity will be

$$\begin{aligned} \Delta I_y &= I(t) \sin(\psi) \approx I(t) \psi \\ &= \alpha I_0 \sin(\omega_{\text{RF}} t + \phi) \left[1 + 2 \sum_{k=1}^{+\infty} \cos(k \omega_R t) \right] , \end{aligned} \quad (3.33)$$

where

$$\alpha = V_{\text{RF}} \pi / V_{\pi, \text{RF}} . \quad (3.34)$$

The necessary condition for harmonic locking can be found from (3.33), as the BOMPD is required to generate a dc error signal which is used to lock the tunable oscillator onto the reference. Therefore, in (3.33) there should be a k such that

$$\omega_{\text{RF}} = k \omega_R . \quad (3.35)$$

This condition is called *harmonic locking condition*. The BOMPD characteristic function, $H(\phi)$, consequently can be found using Equation (3.32) as

$$H(\phi) \approx \alpha I_0 R_\lambda \sin(\phi) , \quad (3.36)$$

By increasing the RF modulation amplitude, the modulator enters the non-linear regime in which case the linear approximation of (3.33) has a high error. Finding the exact form of the BOMPD characteristic function using the Fourier series expansion of $I(t)$ and $\sin(\psi)$ is a tedious task. It is much easier to find the characteristic function of the BOMPD with direct integration and avoid the Fourier series expansion. Applying the condition of harmonic locking, $\omega_{\text{RF}} = k\omega_R$, to (3.30) results in a periodic function with a period of T_R . Therefore, it is sufficient to average over one period of this function to find the phase detector characteristic function.

$$\begin{aligned} H(\phi) &= \frac{R_\lambda}{T_R} \int_{\langle T_R \rangle} dt \Delta I_y(t) \\ &= \frac{R_\lambda}{T_R} \int_{0^-}^{T_R^-} dt I_0 T_R \delta(t) \sin [\alpha \sin(\omega_{\text{RF}} t + \phi) + \psi_{\text{dc}}] \\ &= I_0 R_\lambda \sin [\alpha \sin(\phi) + \psi_{\text{dc}}] . \end{aligned} \quad (3.37)$$

This result is identical to what is derived in [80] but our derivation is much more compact and also the dependency of the BOMPD characteristic function on the bias point variation is considered. Depending on the value of ψ_{dc} , this characteristic function will have different properties which are discussed in following sections. The argument of outer sine function in (3.37) is also defined as

$$\psi_0 = \psi_{\text{dc}} + \alpha \sin(\phi) . \quad (3.38)$$

This definition will be very useful especially in our noise derivations and will be referred to repeatedly.

3.3.1 BOMPD behavior in dynamics of OEPLL

In this section the necessary conditions of phase-locking of OEPLL shown in Figure 3.4(a) using BOMPD are discussed. The characteristic functions of the BOMPD are drawn in Figure 3.6(a) and Figure 3.6(b) for different conditions. The slope of these curves at their operating point is the phase detector gain. Using an RC loop filter shown in 3.5(b) to integrate the output current of the BOMPD (similar to type-II charge pump PLLs) forces the steady state current to be zero [19]. This makes the BOMPD operating point (ϕ) and gain independent of the required tuning voltage for the tunable oscillator. Therefore, the BOMPD should have at least one zero crossing in its characteristic function curve. From this point, when we refer to phase detector gain, we mean the phase detector gain at the zero crossing.

The characteristic function in (3.37) scales linearly with $I_0 R_\lambda$ and its shape varies with respect to two variables, α and ψ_{dc} . An important scenario is when the modulator is biased at the odd symmetry point and $H(\phi)$ becomes

$$H(\phi) = I_0 R \sin [\alpha \sin(\phi)] . \quad (3.39)$$

Equation (3.39) shows that $H(\phi)$ has odd symmetry when the modulator is biased at $\psi_{\text{dc}} = 0$ and the characteristic function has a zero at $\phi = 0$. Another feature of $H(\phi)$

can be derived from (3.37)

$$H\left(\pm\frac{\pi}{2} + \phi\right) = H\left(\pm\frac{\pi}{2} - \phi\right). \quad (3.40)$$

In other words, the characteristic function has even symmetry around $\phi = \pm\pi/2$. Therefore the zeros of the characteristic function come in pairs which are symmetric around $\phi = \pm\pi/2$. These pairs correspond to phase detection gains with equal amplitudes and opposite signs which can be seen in Figures 3.6(a) and 3.6(b) as the slope of the characteristic function at the zero crossings. Depending on the slope of the tuning characteristic curve of the tunable oscillator, the OEPLL locks either with the positive or the negative gain of BOMPD.

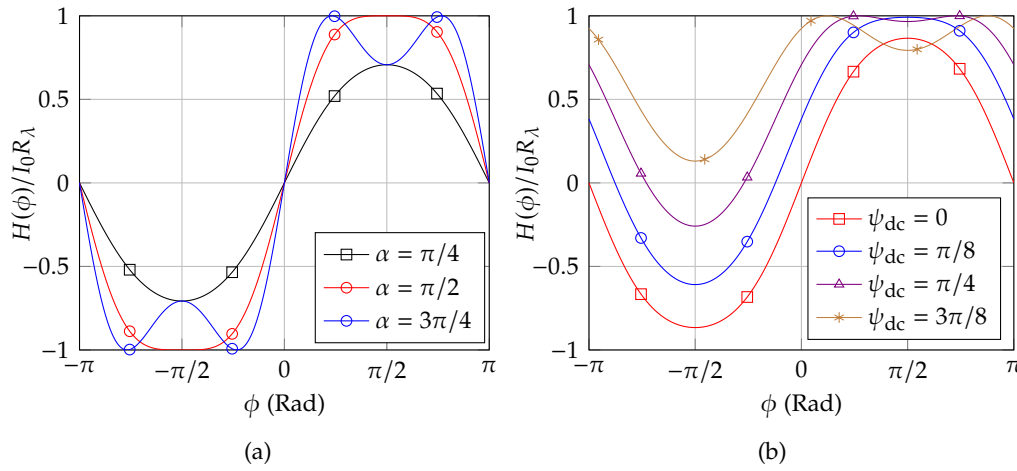


FIGURE 3.6: Phase detector characteristic curves for (a) different RF excitation amplitudes and (b) different bias points.

Another effect that can be seen in Figure 3.6(a) is that as the RF modulation amplitude increases, more zeros may appear in the characteristic function. However, these zeros correspond to relatively high modulation amplitudes. Increasing the RF amplitude to $V_{\pi,RF}$ (which corresponds to $\alpha = 1$) leads to two additional zeros at $\phi = \pm\pi/2$. The phase detector gain at these zeros is 0 or practically very low, and therefore, the loop cannot lock on these points. In addition, considering currently available LiNbO₃ modulators with V_π of approximately 4 V, an RF excitation of V_π corresponds to medium range RF power levels in the 50 Ω system which are suitable for low noise and wideband applications. We therefore avoid further discussion of additional zeros in the transfer characteristics and limit our discussion to RF excitation voltages below V_π .

Figure 3.6(b) shows the effect of the modulator's bias point variation on the BOMPD characteristic function. It can be seen that as the bias point moves toward the $\psi = \pi/2$ even symmetry point, the zero-crossing point moves toward negative values of ϕ , the function is shifted upward and its shape changes. One of the zero crossings of $H(\phi)$ can be found using (3.37) as

$$\phi_0 = -\arcsin\left(\frac{\psi_{dc}}{\alpha}\right) \quad \text{where} \quad |\psi_{dc}| \leq \alpha. \quad (3.41)$$

The other zero of $H(\phi)$ can be found using (3.40). If the absolute value of the offset phase exceeds α , then the transfer characteristic will not have any zeros and

therefore the OEPLL does not lock. One can see in Figure 3.6(b) that as the phase offset ψ_{dc} increases, the slope of $H(\phi)$ at its zero crossing decreases. Also, since the phase detector follows the relation in (3.40), its gain has the same absolute value for both zero crossings with opposite signs. It is usually desired to maximize the phase detector gain, as it minimizes the in-band (inside loop bandwidth) noise of the phase detector and other components. Changing the bias point can also be used as a degree of freedom to fine-tune the phase detector gain and consequently the loop bandwidth. The phase detector gain can be found as the derivative of $H(\phi)$ with respect to ϕ using (3.41) and (3.37)

$$\begin{aligned} K_\phi &= \alpha I_0 R_\lambda \cos(\phi_0) \cos[\alpha \sin(\phi_0) + \psi_{dc}] \\ &= I_0 R_\lambda \sqrt{\alpha^2 - \psi_{dc}^2} . \end{aligned} \quad (3.42)$$

Equation (3.42) shows that K_ϕ is affected by quite a few parameters, such as the MLL average power, photodetector responsivity, RF excitation amplitude, MZM parameters, and MZM dc bias point. Equations (3.42), (3.14) and (3.15) are used to calculate the transfer function of the OEPLL and provide a basic mathematical model of the OEPLL.

3.4 Summary and conclusion

The theory presented in this chapter provides a strong mathematical toolbox for OEPLL analysis, both at the system level and at the component level. Using this theory, the BOMPD can be designed and its phase detection gain can be calculated. The OEPLL transfer functions can consequently be derived using the system level theory and the BOMPD gain. This mathematical model is the foundation of OEPLL design using BOMPD and can be used for system level simulation and estimation of the OEPLL response in time and frequency domain.

Chapter 4

Noise and Nonlinearity in Optoelectronic Phase-Locked Loop

In the previous chapter, we provided a detailed analysis of the OEPLL at the system level and at the component level. This analysis provides a systematic approach for OEPLL design; however, it is not sufficient for OEPLL phase noise estimation and simulation. In addition, the basic model provided in the previous chapter cannot predict the OEPLL behavior in high optical pulse energies and large RF amplitudes. Therefore, additional modeling is required to take into account the noise processes and nonlinear mechanisms in BOMPD. In this chapter, different noise sources of OEPLL are modeled and their effect on the OEPLL phase noise are shown and the results are discussed. Also, the nonlinear effects in BOMPD are shown and different operating regimes of OEPLL as well as its limitations due to nonlinear effects are explained. The results presented in this chapter have been published in peer reviewed journals [author's publication, 55, 56].

4.1 Noise in BOMPD

In Chapter 3, the OEPLL has been modeled and the BOMPD characteristic function and its gain have been derived. Now we focus on modeling various noise sources in BOMPD and their effect on the BOMPD phase noise. There are three main sources of noise that affect the performance of the BOMPD: noise of the photodiodes, relative intensity noise (RIN) of the laser, and the noise of dc voltage applied to the dc electrode of MZM. These noise sources have different behaviors and transfer characteristics that are addressed in this section.

In order to formulate the effect of these noise sources on the BOMPD performance, we first quantify the power spectral density of the noise current at the output of the BOMPD. Taking into account this noise current, the output current of the BOMPD can then be written as

$$i_{\text{out}}(t) = H(\phi) + i_n(t) , \quad (4.1)$$

where $i_{\text{out}}(t)$ is the output current of the BOMPD, $H(\phi)$ is the characteristic function of the BOMPD given in (3.37), and $i_n(t)$ is the output noise current. In the proximity of operating point of the BOMPD, $H(\phi)$ can be approximated as

$$H(\phi) \approx K_\phi \times \phi . \quad (4.2)$$

Substituting this approximation into (4.1) gives

$$i_{\text{out}}(t) = K_{\phi} \left(\phi + \frac{i_n(t)}{K_{\phi}} \right). \quad (4.3)$$

The first term in parentheses in the right-hand side of (4.3) is the phase difference between the desired harmonic of the envelope of the optical pulse train and the RF signal. The second term is the output noise current of the BOMPD translated into phase domain and is called the phase noise of the BOMPD. Like many other random processes, it is practical to talk about the PSD of phase noise, rather than its instantaneous value. The PSD of the phase noise of the BOMPD can be written as

$$S_{\phi_n}(f) = \frac{S_{i_n}(f)}{K_{\phi}^2} = \frac{S_{i_n}(f)}{I_0^2 R_{\lambda}^2 (\alpha^2 - \psi_{\text{dc}}^2)}, \quad (4.4)$$

where $S_{i_n}(f)$ is the PSD of the output noise current $i_n(t)$, and $S_{\phi_n}(f)$ is the PSD of the *equivalent* phase noise caused by this current noise. We also substituted K_{ϕ} from (3.42) to (4.4). With this approach, all we have to do is to find the output noise current caused by different mechanisms in the BOMPD. The phase noise caused by these mechanisms is then found using the relation in (4.4).

4.1.1 Shot noise of photodiodes

Shot noise of photodiodes is considered to be the main source of noise in BOMPD which can not be avoided — adapting a classical point of view and assuming the light is in coherent state [81]. Although shot noise is well studied and modeled as a Poisson process, treatment of non-stationary noise due to pulsed mode stimulation of the photodiodes used in BOMPD requires further attention. This Poisson process can be estimated as a Gaussian process since in BOMPD we are dealing with a very high number of photons. In order to model the non-stationary shot noise, first the time dependent output intensities of the BOMPD are determined. From these intensities, the instantaneous variance of the non-stationary shot noise of the photodiode currents is calculated. This instantaneous variance is then decomposed into two terms: a deterministic time-variant window function multiplied by a stationary Gaussian noise. This decomposition is the key in deriving the autocorrelation function and the power spectral density of the non-stationary photodiode noise current.

The pulse widths of MLLs are typically below 1 ps which is at least 25 times shorter than the RF signal period in the microwave band up to 40 GHz frequency range. Therefore, the modulation term in (3.24), $1 \pm \sin(\psi)$, is considered approximately constant during the time interval it is sampled by the MLL pulses. The harmonic locking condition, $\omega_{\text{RF}} = M\omega_R$ for a positive integer M , leads to sampling of the modulation term at the same phase. Therefore, the modulation term in (3.24) can be considered as constant. Substituting (3.26) in (3.24) under this assumption, the output intensities of the modulator can be written as

$$I_y^{\pm} = \frac{1}{2} I_0 T_R \sum_{m=-\infty}^{+\infty} P\left(t - \frac{m}{f_R}\right), \quad (4.5)$$

where I_y^{\pm} denotes the intensity of the modulator outputs y^{\pm} in Figure 3.4(a) and ψ_0 is given in (3.38). The photodiode converts the photons into electron-hole pairs. Generation of charge carriers with photons has Poisson statistics and generates shot

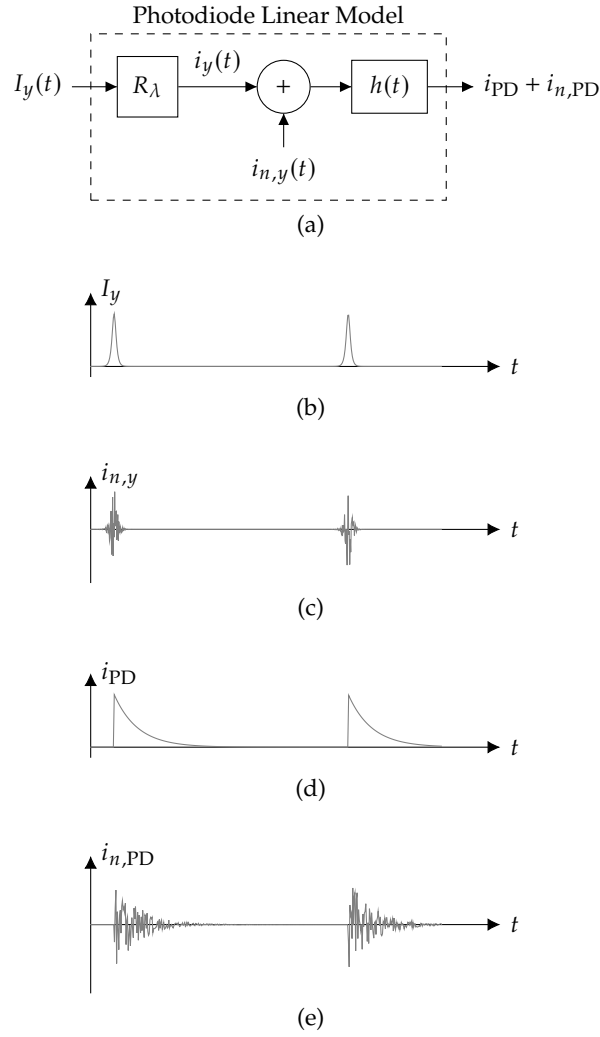


FIGURE 4.1: (a) Linear model of photodiode including shot noise, (b) intensity of the incident beam generated by a femtosecond laser, (c) generated shot noise before getting shaped by photodiode response, (d) output current pulses of the photodiode and (e) shot noise of the photodiode.

noise [81, Chapter 3]. These charge carriers travel toward the photodiode junctions with different velocities. This leads to widening of the optical pulse at the photodiode, the so-called transit-time spread [37, Chapter 17]. These mechanisms are included in the linear model of the photodiode illustrated in Figure 4.1(a). The photodiode shot noise $i_{n,y}$ is added after linear generation of charge carriers modeled by a constant responsivity R_λ . The transit-time spread is modeled by a lossless linear time-invariant block with an impulse response of $h(t)$ that does not recombine or generate charge carriers and therefore

$$\int_0^\infty dt h(t) = 1. \quad (4.6)$$

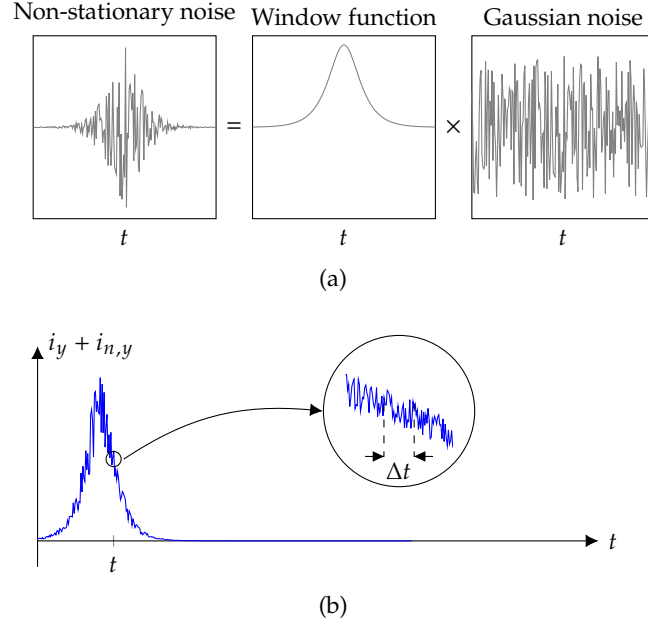


FIGURE 4.2: (a) Decomposition of non-stationary shot noise into the product of a deterministic window function and Gaussian noise, and (b) quasi-stationary approximation of the optical pulse in a short interval of Δt .

Using this linear model, the output current of the upper & lower photodiodes can be written as

$$i_{\text{PD}}^{\pm} = \frac{1}{2} I_0 T_R R_{\lambda} [1 \pm \sin(\psi_0)] \sum_{m=-\infty}^{+\infty} P(t - \frac{m}{f_R}) * h(t), \quad (4.7)$$

where $*$ denotes the convolution operation.

The optical pulses of MLL have a much lower effective temporal width than the photodiode impulse response. Therefore, the optical pulse shape $P(t)$ can be approximated as the Dirac delta function and the photodiode currents become

$$i_{\text{PD}}^{\pm} = \frac{1}{2} R_{\lambda} I_0 T_R [1 \pm \sin(\psi_0)] \sum_{m=-\infty}^{+\infty} h(t - \frac{m}{f_R}). \quad (4.8)$$

When the OEPLL is locked, the output intensities of the BOMPD become equal or equivalently $\psi_0 = 0$. The output currents of the upper and lower photodiode, i_{PD}^{\pm} , consequently become equal

$$i_{\text{PD}}^{\pm} = \frac{1}{2} R_{\lambda} I_0 T_R \sum_{m=-\infty}^{+\infty} h(t - \frac{m}{f_R}). \quad (4.9)$$

Now the photodiode currents are derived and we are ready to find the shot noise. The shot noise of the optical pulse is not stationary and its properties vary with respect to time. Therefore, we employ a quasi-stationary approach to find the PSD of the current noise. The probability of detection of a photon at a certain time is statistically independent of detection of a photon at any time earlier. Therefore, the shot noise $i_{n,y}(t)$ can be factorized as a product of a white Gaussian process, which is memoryless and models the statistical independence of detection of the photons,

and a time varying deterministic window function which models the non-stationary behavior of $i_{n,y}(t)$. This decomposition of non-stationary noise is illustrated graphically in Figure 4.2(a). If we consider a short time slot Δt in the neighborhood of t , the intensity of the pulse can be considered as constant. This assumption is also illustrated graphically in Figure 4.2(b). The instantaneous variance of the noise can then be written as

$$\begin{aligned} \mathbb{E} \left[i_{n,y}^2(t) \right] &= 2q i_y(t) \Delta f \\ &= q R_\lambda I_0 T_R \sum_{m=-\infty}^{+\infty} P\left(t - \frac{m}{f_R}\right) \Delta f, \end{aligned} \quad (4.10)$$

where $\mathbb{E}[\cdot]$ denotes the expectation value, q is the electron charge and Δf is the noise bandwidth (note that time and frequency are orthogonal, and reducing temporal resolution corresponds to increasing spectral range. In other words $\Delta f \gg (\Delta t)^{-1}$ has to be satisfied for the quasi-stationary approximation in (4.10) to be valid). We also suppressed the upper \pm index as the currents of the lower and upper photodiodes are equal and have the same stochastic properties. We decompose the noise current $i_{n,y}$ into two terms, i_n and $w(t)$ such that

$$i_{n,y}(t) = i_n(t)w(t), \quad (4.11)$$

where $w(t)$ is a deterministic window function which models the non-stationary behavior of the noise current and i_n is a white Gaussian noise current with a **single-sided** power spectral density (PSD) of $qR_\lambda I_0$. The auto-correlation function of this noise current according to Wiener–Khinchin theorem is the inverse Fourier transform of its PSD

$$R_{i_n}(t, t') = \mathbb{E} [i_n(t) i_n(t')] = \frac{1}{2} q R_\lambda I_0 \delta(t - t'). \quad (4.12)$$

Now we find the window function $w(t)$ such that the variance of the noise current in (4.11) is equal to the noise current variance in (4.10). The variance of (4.11) can be written as

$$\mathbb{E} \left[i_{n,y}^2(t) \right] = w^2(t) \mathbb{E} \left[i_n^2(t) \right] = w^2(t) q R_\lambda I_0 \Delta f. \quad (4.13)$$

By comparing (4.10) and (4.13), the time varying window function $w(t)$ can be determined

$$w(t) = \sqrt{T_R \sum_{m=-\infty}^{+\infty} P\left(t - \frac{m}{f_R}\right)}. \quad (4.14)$$

If we assume the optical pulses do not overlap, (4.14) can be further simplified

$$w(t) = \sum_{m=-\infty}^{+\infty} \sqrt{T_R P\left(t - \frac{m}{f_R}\right)}. \quad (4.15)$$

Equation (4.14) and (4.15) show the photodiode noise current is proportional to the square root of the pulse shape, $P(t)$. Now using (4.11) the auto-correlation function

of the non-stationary noise current $i_{n,y}$ can be found

$$\begin{aligned} R_{i_{n,y}}(t, t') &= \mathbb{E}[i_{n,y}(t)i_{n,y}(t')] \\ &= \frac{1}{2}qR_{\lambda}I_0\delta(t - t')w(t)w(t'). \end{aligned} \quad (4.16)$$

The dependency of $R_{i_{n,y}}(t, t')$ to t and t' rather than their difference $t - t'$ is because of non-stationary nature of the pulsed noise current $i_{n,y}$. The single-sided power spectral density of the noise current is

$$\begin{aligned} S_{i_{n,y}}(f) &= \mathbb{E} \left[\lim_{T \rightarrow \infty} \frac{1}{T} \left| \int_{-T}^{+T} dt i_{n,y}(t) e^{j\omega t} \right|^2 \right] \\ &= \lim_{T \rightarrow \infty} \frac{1}{T} \int_{-T}^{+T} \int_{-T}^{+T} dt dt' \mathbb{E}[i_{n,y}(t)i_{n,y}(t')] e^{j\omega(t-t')}, \end{aligned} \quad (4.17)$$

where $\omega = 2\pi f$. Substituting (4.16) in (4.17) and using the relation between the window function and the pulse shape in (4.15) and the normalizing condition in (3.27), the single-sided power spectral density of the noise current can be found

$$\begin{aligned} S_{i_{n,y}}(f) &= \frac{1}{2}qR_{\lambda}I_0 \lim_{T \rightarrow \infty} \frac{1}{T} \int_{-T}^{+T} dt w^2(t) \\ &= qR_{\lambda}I_0. \end{aligned} \quad (4.18)$$

Therefore, the shot noise $i_{n,y}$ has a well defined power spectral density, although it is not a stationary process. The magnitude of this PSD is equal to the PSD generated by a continuous wave optical field with an intensity of $\frac{1}{2}I_0$. The intensity of this CW optical field is equal to the average intensity of the pulsed optical field $I_y(t)$. Therefore, only the average intensity affects the shot noise power spectral density. The reason that shot noise is independent of the pulse shape is that its instantaneous variance is proportional to the photocurrent current. This consequently leads to proportionality of the window function to the *square root* of the pulse shape. The pulse shape is once again squared in derivation of its PSD, in equations (4.16)–(4.18), and then integrated. This sequence of mathematical operations that naturally occurs in the photodiode demonstrates the shot noise independence of the optical pulse shape.

The noise current $i_{n,y}$ generated in the illumination region of the photodiode is then shaped by the linear time-invariant block in Figure 4.1(a) which models the transit-time spread with an impulse response of $h(t)$. Therefore the single-sided PSD of the output noise current is

$$S_{i_{n,PD}}(f) = S_{i_{n,y}}(f)|H(f)|^2 = qR_{\lambda}I_0|H(f)|^2, \quad (4.19)$$

where $H(f)$ is the Fourier transform of $h(t)$. The result in (4.19) is identical to what has been derived by Quinlan *et al.* [82], where the detection process is treated semi-classically. In [82] the incident beam is made of photons that are detected at the photodiode with a certain probability in a short time interval. The detection probability consequently leads to randomization of detection and hence shot noise. In contrast, we employed a fully classical approach where the incident beam is an optical field (*not photons*) with a certain intensity that is detected at the photodiode. By assuming the shot noise of a CW optical field in (4.10) for our quasi-stationary approach, we avoided discretization of light. Also, the stationary assumption in (4.10)

in a short interval of Δt is equivalent to the assumption of single photon detection in a sufficiently short interval in semi-classical approach in [82]. One advantage of our fully classical approach is that it can be generalized to non-stationary processes that have a defined PSD in a short time interval. As we will see in Section 4.1.2, this approach is especially helpful to treat non-stationary generation-recombination noise.

For phase detector application, the shot noise of the photodiode is important inside the loop bandwidth which is usually below 10 MHz. The bandwidth of the photodiode is usually much higher than the loop bandwidth; therefore, $H(f)$ in (4.19) can be approximated as 1. The single-sided PSD of the output noise current of the BOMPD is the superposition of the upper and lower photodiode shot noise currents which are statistically independent

$$S_{i_{n,\text{shot}}}(f) = 2qR_{\lambda}I_0. \quad (4.20)$$

The phase noise of the BOMPD can then be found using the relation in (4.4) as

$$S_{\phi_{n,\text{shot}}}(f) = \frac{S_{i_{n,\text{shot}}}(f)}{K_{\phi}^2} = \frac{2q}{R_{\lambda}I_0(\alpha^2 - \psi_{\text{dc}}^2)}, \quad (4.21)$$

where $S_{\phi_n}(f)$ is the phase noise of the BOMPD. The photodiode dark current has a negligible effect on the phase noise, because the main contributor to the photodiode currents is the incident beam from the MLL. Taking into account the dark current, (4.20) can be rewritten as

$$S_{i_{n,\text{shot}}}(f) = 2q(R_{\lambda}I_0 + 2I_{\text{dark}}), \quad (4.22)$$

where I_{dark} is the dark current of a single photodiode. The dark current is in the range of nanoamperes while the beam induced photocurrent is in the range of at least hundreds of microamperes. So it is a fair approximation to neglect the photodiodes dark current.

Shot noise of photodiodes puts a theoretical limit on the phase noise of the BOMPD (assuming the light is in coherent state). However, there are undesired effects that can lead to phase noise degradation in the BOMPD above the shot noise limit. In the following sections, we discuss other sources of noise in the BOMPD and their transfer characteristics.

4.1.2 Generation-Recombination noise

In addition to shot noise, photodiodes have random variation of charge carriers due to generation-recombination (GR) of charge carriers. While the PSD of shot noise is proportional to the photocurrent, the GR noise PSD is proportional to the square of the photocurrent and may exceed shot noise at high optical excitation levels. The two-sided power spectral density of GR noise of an intrinsic semiconductor stimulated with a CW optical field, $S_{i_{\text{GR-CW}}}$, can be written as [83, 84]

$$S_{i_{\text{GR-CW}}}(f) = \frac{2i_{\text{PD}}^2\tau}{n_0(1 + \omega^2\tau^2)}, \quad (4.23)$$

where $\omega = 2\pi f$, i_{PD} is the photocurrent, n_0 is the number of free carriers in equilibrium and τ is the decay time.

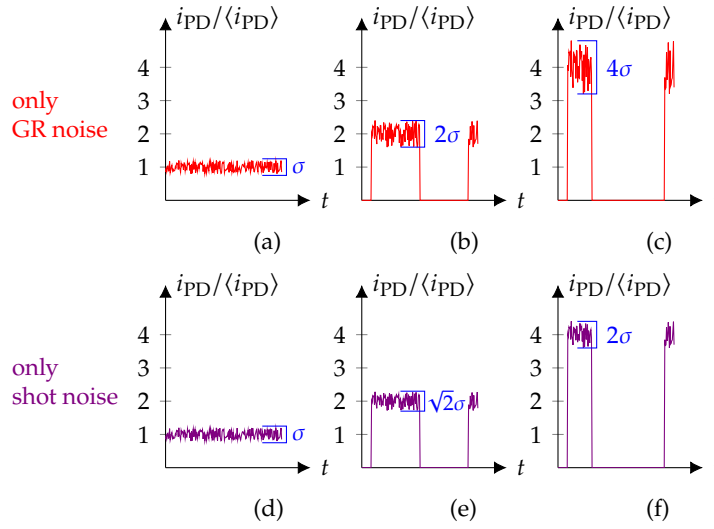


FIGURE 4.3: Qualitative illustration of the effect of duty cycle on generation-recombination noise of photodiode in comparison with the photodiode shot noise: (a) GR noise, continuous-wave, (b) GR noise, 50% duty cycle and (c) GR noise, 25% duty cycle (d) shot noise, continuous-wave, (e) shot noise, 50% duty cycle and (f) shot noise, 25% duty cycle.

When the active region of photodiode is illuminated with an optical pulse, electron-hole pairs are generated. On the one hand, the built-in electric field and the external field (caused by the external dc supply) of the photodiode separates these charge carriers and moves them toward the photodiode external junctions. This mechanism is linear, and the difference between the mobility of electrons and holes contributes to the overall photodiode transit time and limiting its bandwidth. On the other hand, the Coulomb interaction between electrons and holes creates a counter-acting electric field that attracts electrons and holes to each other. This attraction force is a function of the optical beam intensity which makes it a nonlinear mechanism and leads to dependency of the transit time to the optical intensity. Generation and recombination of charge carriers occurs at this level, where the charge carriers are still in the active region. The nonlinearity of photodiode under high excitation levels consequently makes the dynamics of generation-recombination noise both nonlinear and a function of time. This level of complexity is an obstacle in providing a general formula for generation-recombination noise under pulsed excitation, although a formula for the PSD of GR noise under CW excitation of photodiodes is available. Our aim here is to illustrate qualitatively, with some simplified assumptions, how pulsed excitation causes enhancement of GR-noise. The GR-noise enhancement consequently limits the phase noise improvement in BOMPD when the average intensity is increased, which is expected if only shot noise is taken into account.

The quadratic dependence of GR-noise PSD to the photocurrent has another undesired effect on the photodiode noise, when the excitation beam is an optical pulse. This effect is illustrated graphically in Figure 4.3 where the photodiode GR noise is shown for photocurrent waveforms with the same average but with different duty cycles (γ). On time scales longer than τ , the variance of GR noise is proportional to the instantaneous photocurrent which scales with $1/\gamma$. The PSD of GR noise, on the one hand, is proportional to the noise variance (during the presence of the optical pulse) which scales with $1/\gamma^2$ and on the other hand, is proportional to γ because

of temporal averaging. Therefore, the PSD of GR noise is inversely proportional to the pulse duty cycle γ . It is noteworthy that under the same conditions, during the presence of photocurrent, the instantaneous variance of the shot noise scales with $1/\gamma$ which makes the shot noise PSD independent of pulse shape and duty cycle, as discussed in Section 4.1.1.

The behavior of GR noise with respect to duty cycle of the photocurrent can also be shown mathematically with some simplified assumptions. We assume the photocurrent pulse train has a rectangular shape and a duty cycle of γ and has an average of $\langle i_{PD} \rangle$. The rectangular pulse shape simplified assumption is because of dependency of the GR noise variance to the square of instantaneous photocurrent according to (4.23), in contrast to shot noise variance that is proportional to the instantaneous photocurrent. This square dependency consequently leads to dependency of GR-noise PSD to the integral of the square of the normalized pulse shape. By assuming a rectangular pulse shape, we want to avoid such complications. For simplicity, we also assume the pulse width is sufficiently longer than the decay time τ such that the generation-recombination stochastic properties do not vary during the presence of photocurrent. With these assumptions, the GR noise can be treated similar to the procedure the shot noise was treated in Section 4.1.1 and can be written as the product of a Gaussian noise and a rectangular window function

$$i_{GR}(t) = i_{GR-CW}(t)\Pi(t) , \quad (4.24)$$

where $i_{GR}(t)$ is the GR-noise of the photodiode with pulsed stimulation, $i_{GR-CW}(t)$ is the GR noise of the photodiode stimulated with a CW optical field according to (4.23) which generates a photocurrent of $\langle i_{PD} \rangle/\gamma$ and $\Pi(t)$ is a periodic rectangular window function with a duty cycle of γ

$$\Pi(t) = \begin{cases} 1 & \text{for } T_R(m - 0.5\gamma) < t < T_R(m + 0.5\gamma) \\ 0 & \text{elsewhere} \end{cases} , \quad (4.25)$$

where T_R is the period of the rectangular pulse train and m is any integer. If we assume the generation-recombination noise has a white spectrum compared to the frequency spectrum of the window function ($\tau \ll \gamma T_R$), the power spectral density and autocorrelation function of the continuous-wave GR noise can be approximated as

$$S_{i_{GR-CW}}(f) \approx 2\langle i_{PD} \rangle^2 \tau / \gamma^2 n_0 \quad (4.26)$$

and

$$R_{i_{GR-CW}}(t, t') \approx 2\langle i_{PD} \rangle^2 \tau \delta(t - t') / \gamma^2 n_0 . \quad (4.27)$$

The two-sided power spectral density of the GR noise can now be found similar to the procedure used in (4.17) and (4.18) as

$$\begin{aligned} S_{i_{GR}}(f) &= \lim_{T \rightarrow \infty} \frac{1}{2T} \int_{-T}^{+T} \int_{-T}^{+T} dt dt' E[i_{GR}(t)i_{GR}(t')] e^{j\omega(t-t')} \\ &= 2\langle i_{PD} \rangle^2 \tau / \gamma n_0 , \end{aligned} \quad (4.28)$$

Therefore, for the same average photocurrent, the PSD of GR noise is inversely proportional to the duty cycle. We have to emphasize that the formalism above draws a qualitative picture on the effect of duty cycle on the overall GR noise, but

is not very accurate for stimulation of photodiodes with high energy femtosecond pulses. For instance, the assumption of uniform electric field along the intrinsic region of photodiode used in derivation of (4.23) is no longer valid due to Coulomb interaction between charge carriers and space-charge effects [33, 34, 83]. Also, the photocurrent does not have a rectangular shape and its rise/fall time considering the space-charge effect under illumination of photodiode with high-energy femtosecond optical pulses has to be taken into account.

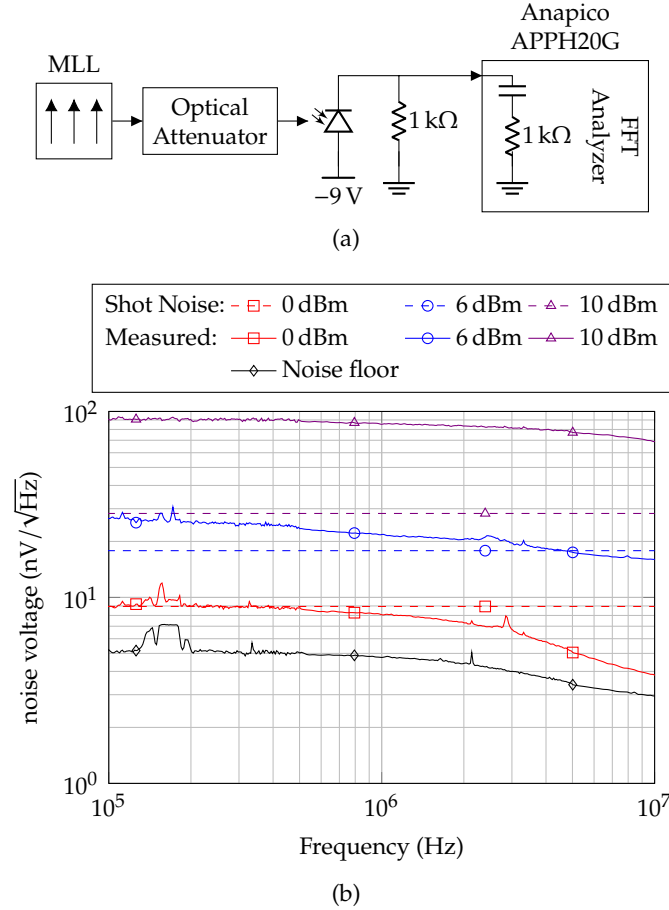


FIGURE 4.4: (a) Photodiode noise measurement setup; (b) photodiode (solid) measured noise PSD and (dashed) theoretical shot noise levels at different optical intensities; $v_n = \sqrt{2qR_\lambda I_0 R_L}$ (V/√Hz), where R_λ is the integrated responsivity taking into account its compression at high illumination levels according to (4.39), R_L is the effective load resistance (500 Ω) and I_0 is the average intensity of the optical beam.

Enhancement of GR noise under excitation of photodiode with high optical intensities can also be observed by experiment. Figure 4.4(a) shows a setup for photodiode noise measurement. An InGaAs photodiode with an active area diameter of 120 μm is illuminated with femtosecond pulses of a MLL (MENHIR1550 [12]) and an optical attenuator is used to change the intensity of the optical pulses. The optical pulses have a width of 185 fs and a repetition rate of 250 MHz. The photodiode is terminated to a 1 kΩ resistive load and connected to an FFT analyzer (Anapico APPH20G). The FFT analyzer has an input resistance of 1 kΩ (ac coupled) which makes the overall photodiode load resistance equal to 500 Ω. The 1 dB cut-off frequency of the measurement setup is approximately 2 MHz. Figure 4.4(b) shows the measured noise

voltage in $V/\sqrt{\text{Hz}}$. It can be seen that at high illumination intensities with femtosecond pulses, the GR noise becomes dominant and exceeds the shot noise. The PSD of the output noise at 0 dBm incident optical power has a good matching with the estimated shot noise. At 10 dBm incident optical power, however, the noise voltage has increased approximately by a factor of 10 which corresponds to an increase of 100 in V^2/Hz . This increase in noise PSD is a signature of GR noise because of the proportionality of its PSD to the square of photocurrent, in contrast to shot noise PSD that is proportional to the photocurrent. The enhancement of photodiode noise consequently leads to degradation of the BOMPD phase noise according to (4.21). The GR noise can be mitigated by increasing the number of equilibrium charge carriers, n_0 in (4.23), for instance by increasing the illumination area of the photodiode.

The GR noise of photodiode is an undesired effect that has to be suppressed for low-phase-noise OEPLL designs. Due to nonlinear dependency of photodiode response time to the optical intensity under pulsed excitation and also to the illumination condition, providing an exact formula for GR noise is complicated. The objective of the discussion above is to point to a strong source of noise in photodiodes when illuminated with high energy pulses that leads to phase noise degradation in the BOMPD, and to discuss the available means to suppress this undesired noise.

4.1.3 Relative intensity noise of the MLL

The relative intensity noise (RIN) is the intensity fluctuations of the light. RIN is associated with the light source, in contrast to shot noise that is due to quantum nature of light itself. While shot noise is generated during the detection process, the noise of the laser is rooted in the generation of the light and can be modeled as an amplitude noise term in the intensity of the MLL beam [75] as

$$I(t) = I_0 T_R \left[1 + a_n(t) \right] \sum_{m=-\infty}^{+\infty} P\left(t - \frac{m}{f_R}\right), \quad (4.29)$$

where $a_n(t)$ is the RIN of the optical pulse train. Now we investigate the effect of RIN of MLL on the noise performance of the BOMPD. The output currents of the photodiodes incorporating the RIN of the laser (under the OEPLL locked condition) can be written similar to (4.9) as

$$i_{\text{PD}}^{\pm} = \frac{1}{2} R_{\lambda} I_0 T_R \left[1 + a_n(t) \right] \sum_{m=-\infty}^{+\infty} h\left(t - \frac{m}{f_R}\right). \quad (4.30)$$

The RIN of the laser generates noise current in both the upper and lower photodiodes. Unlike the shot noise of the photodiodes, these noise currents in the upper and lower photodiodes are perfectly correlated and cancel out when the OEPLL is in steady state, $i_{\text{PD}}^+ = i_{\text{PD}}^-$. Therefore, the noise of the laser does not have any first-order effect on the phase noise of the BOMPD.

4.1.4 Noise of MZM bias voltage

Another source of noise in the BOMPD is the low frequency noise of the dc voltage used to bias the modulator. The noise of dc voltage, $v_n(t)$, can be incorporated in (3.25) as

$$\psi = \psi_{\text{RF}} + \psi_{\text{dc}} + \psi_n(t), \quad (4.31)$$

where

$$\psi_n(t) = \pi v_n(t)/V_{\pi,dc} . \quad (4.32)$$

Assuming the linear photodiode model of Figure 4.1(a), the output current of the BOMPD can be rewritten using (3.24) as

$$\begin{aligned} i_{\text{BOMPD}} &= R_\lambda [I(t) \sin(\psi)] * h(t) \\ &\approx R_\lambda [I(t) \sin(\psi_{\text{RF}} + \psi_{\text{dc}}) \\ &\quad + \psi_n(t) I(t) \cos(\psi_{\text{RF}} + \psi_{\text{dc}})] * h(t) , \end{aligned} \quad (4.33)$$

where we assumed $v_n(t)$ is small enough to have

$$\cos(\psi_n(t)) \approx 1 \quad \text{and} \quad \sin(\psi_n(t)) \approx \psi_n(t) . \quad (4.34)$$

The first term in the brackets on the right-hand side of (4.33) leads to the phase detector characteristic function. The second term is the noise of the bias voltage and shows the bias voltage noise is multiplied by the intensity waveform of the MLL $I(t)$, and, due to its harmonious nature, is modulated around integer multiples of the reference repetition rate. These modulated noise terms are filtered by the loop filter and only the low frequency noise term around zero frequency affects the BOMPD output noise current. The low frequency term of this noise current can be found similar to the treatment of the phase detector characteristic curves in [18] and the detailed steps are given in the Appendix D. The relation between the BOMPD noise current due to the bias voltage of the dc electrode, $i_{n,\text{bias}}$, and the noise of the dc voltage is

$$i_{n,\text{bias}}(t) = R_\lambda I_0 \cos(\psi_0) \psi_n(t) , \quad (4.35)$$

where ψ_0 is given in (3.38) and is zero at steady-state. Therefore the output noise current at steady state simply will be

$$i_{n,\text{bias}}(t) = R_\lambda I_0 \psi_n(t) . \quad (4.36)$$

The PSD of this noise current can be found by substituting (4.32) into (4.36)

$$S_{i_{n,\text{bias}}}(f) = \left(\frac{\pi R_\lambda I_0}{V_{\pi,dc}} \right)^2 S_{v_n}(f) , \quad (4.37)$$

where $S_{v_n}(f)$ is the power spectral density of v_n . The contribution of the bias voltage noise to the overall phase noise can then be found by substituting the PSD of this noise current into (4.4)

$$S_{\phi_{n,\text{bias}}}(f) = \frac{\pi^2}{V_{\pi,dc}^2 (\alpha^2 - \psi_{\text{dc}}^2)} S_{v_n}(f) . \quad (4.38)$$

This equation shows the phase noise caused by the noise of the bias voltage is independent of the average optical excitation level and the photodiode responsivity. This leaves the designer with a few degrees of freedom to suppress the noise caused by the bias voltage; using a modulator with higher π -voltage for the dc-electrode, increasing the RF power level and consequently α , and also using a dc source with lower noise levels in the first place. Since the phase noise caused by photodiodes' shot

noise is inversely proportional to the average intensity of the optical beam according to (4.21), it is necessary to reduce the noise of the bias voltage to make sure the OEPLL phase noise is not limited by the noise of the bias voltage.

4.2 Nonlinear effects in BOMPD

Extracting the phase information of a periodic signal requires a nonlinear operation which makes any phase detector a nonlinear device. Although such a device is nonlinear, it behaves linearly in the phase domain. Therefore, by nonlinearity in BOMPD, we address the mechanisms that affect the phase detector characteristic function beyond the scope of linear phase detector model. These mechanisms are a function of the excitation levels of the inputs of BOMPD: the intensity of the optical field and the RF excitation amplitude. With respect to the optical input, we assume BIM behaves linearly and limit the discussion in Section 4.2.1 to nonlinearity in photodiodes. The nonlinear effects on the BOMPD characteristic function with respect to the RF excitation amplitude are discussed in 4.2.2.

4.2.1 Saturation of the photodiodes

High energy pulses of MLLs affect the performance of photodiodes with space-charge effect and absorption saturation [33–36, 85]. The space-charge effect leads to a counteracting E-field in the illumination region of the photodiode which slows down the charge carriers and increases the transit time. This effect is especially important for high-speed and high-power photodetectors used for generation of RF signals with high signal to noise ratios (SNRs). The increase of the response time due to space-charge effect is not problematic in BOMPD, since the OEPLL loop is usually much slower than the photocurrent pulses. Therefore the approximation of $H(f) \approx 1$ is still valid.

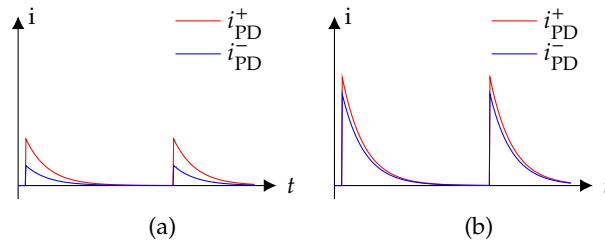


FIGURE 4.5: Qualitative illustration of the upper (red) and lower (blue) photodiode currents of the BOMPD in the presence of a small phase difference ϕ when the intensity of the input beam (a) is low and the photodiodes operate in the linear region and (b) is high and the photodiodes operate in the saturation region.

High energy pulses of MLLs also lead to saturation of charge carriers in the intrinsic zone and compression of the photodiode responsivity. This mechanism is especially important in BOMPD, as the phase detection gain is directly proportional to the photodiode responsivity. The linear BOMPD gain formula in (3.42) suggests increasing the intensity of the optical field results in more phase detector gain, however, absorption saturation of the photodiodes puts a limit on the gain enhancement. This is illustrated graphically in Figures 4.5(a) and 4.5(b) in which the photocurrent pulses

of the photodiode pair in the presence of a small phase difference ϕ for different optical excitation levels are drawn. Although the photocurrent pulses in Figure 4.5(a) have a smaller amplitude than that of the photocurrent pulses in Figure 4.5(b), they exhibit a higher average current difference as the photodiodes are still in the linear region. This current difference is an indication of the BOMPD phase detection gain. In other words, at very high optical pulse energies, the upper and lower photodiodes get saturated and generate almost equal photocurrents which leads to lower phase detection gain.

The absorption saturation of photodiodes has been modeled in [85] by defining *integrated responsivity* as a function of the pulse energy

$$R_\lambda(E) = \frac{R_{\lambda 0}}{1 + E/E_{\text{sat}}} , \quad (4.39)$$

where E is the pulse energy, $R_{\lambda 0}$ is the linear responsivity and E_{sat} is the pulse energy at which the integrated responsivity is reduced by a factor of 2. It is noteworthy that this model for saturation of semiconductor is similar to the model of saturable absorber given in (2.11). However, instead of dependency on instantaneous intensity of the optical pulse, the responsivity is a function of the pulse energy. The measured integrated responsivity of a commercial InGaAs photodiode with an active area diameter of $120 \mu\text{m}$ is shown in Figure 4.6. A commercial MLL with a center wavelength of 1560 nm and a pulse width of 185 fs is used for the characterization.

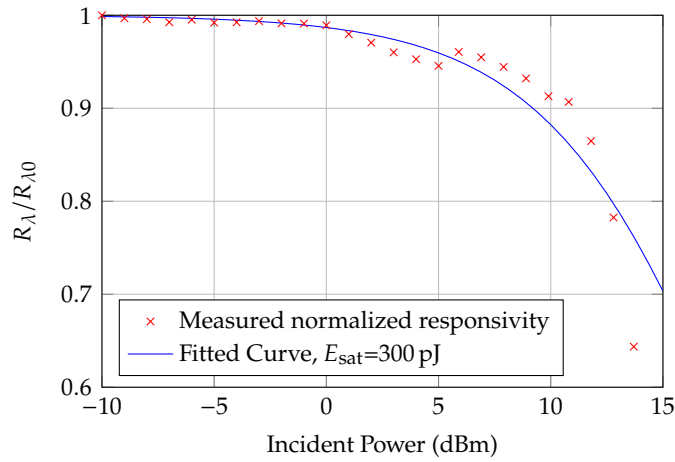


FIGURE 4.6: (red) Measured normalized integrated responsivity and (blue) fitted curve according to (4.39)

In order to formulate the effect of the absorption saturation on the BOMPD gain, the photocurrent of upper and lower photodiodes as a function of pulse energy are derived. The average of the difference of these photocurrent pulses is the BOMPD gain according to (3.31). The energy of the output optical pulses of the BOMPD can be found using (3.27) and (4.5) as

$$E_y^\pm = \frac{1}{2} I_0 T_R [1 \pm \sin(\psi_0)] , \quad (4.40)$$

where ψ_0 is given in (3.38). Using the nonlinear responsivity in (4.39), the output currents of the photodiodes can be found similar to (4.7) as

$$i_{\text{PD}}^{\pm} = \frac{1}{2} I_0 T_R R_{\lambda}(E_y^{\pm}) [1 \pm \sin(\psi_0)] \sum_{m=-\infty}^{+\infty} h(E_y^{\pm}, t - \frac{m}{f_R}), \quad (4.41)$$

where we replaced the linear impulse response $h(t)$ with nonlinear $h(E, t)$ and the linear responsivity R_{λ} with $R_{\lambda}(E)$ which are functions of the optical pulse energy. The normalization condition in (4.6) still holds for the nonlinear response since the compression of the responsivity due to absorption saturation is already included in (4.39). The average photodiode currents therefore are

$$\langle i_{\text{PD}}^{\pm} \rangle = \frac{1}{2} I_0 R_{\lambda}(E_y^{\pm}) [1 \pm \sin(\psi_0)]. \quad (4.42)$$

The BOMPD characteristic function can be found using equations (3.31) and (4.42)

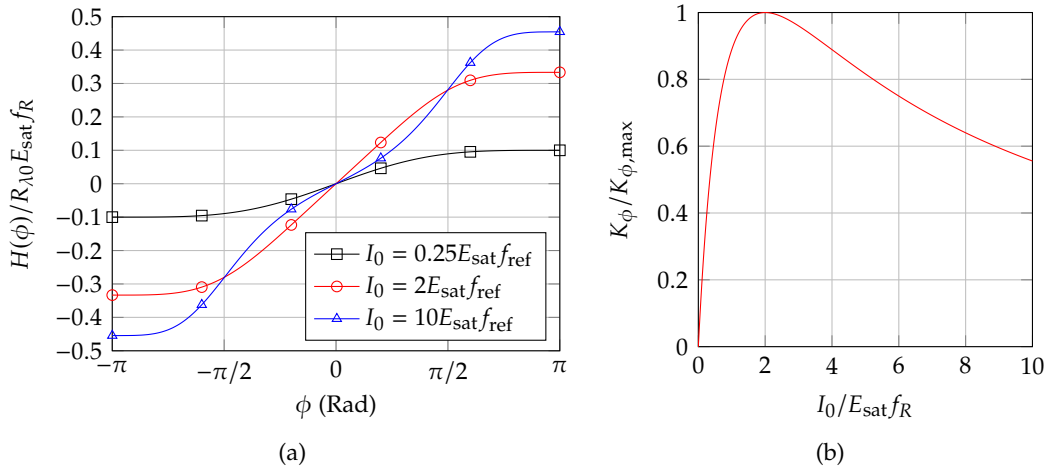


FIGURE 4.7: (a) Characteristic function of BOMPD at different optical pulse energy levels corresponding to (black) linear region, (red) maximum phase detector gain and (blue) deep saturation of photodiodes. (b) Normalized gain of BOMPD with respect to input average optical intensity.

and is plotted for pulse energies close to saturation of photodiodes in Figure 4.7(a). It can be seen that the slope of the characteristic function at the zero crossing decreases for high pulse energies, which is also shown qualitatively using Figure 4.5. The phase detector characteristic function and gain have complicated forms when described with respect to the phase difference ϕ . However, the phase detector gain K_{ϕ} at the zero crossing has a simple expression (the derivation steps are given in Appendix E)

$$K_{\phi} = \frac{R_{\lambda 0} I_0 \sqrt{\alpha^2 - \psi_{\text{dc}}^2}}{(1 + I_0 T_R / 2 E_{\text{sat}})^2}, \quad (4.43)$$

and is plotted in Figure 4.7(b). The numerator in (4.43) is same as the linear phase detector gain in (3.42) and for very low pulse energies, $I_0 \ll 2 f_R E_{\text{sat}}$, the denominator converges to 1. At very high pulse energies, the phase detector gain becomes inversely proportional to the intensity of the optical beam. The maximum of phase detector

gain is

$$K_{\phi, \max} = \frac{R_{\lambda 0} E_{\text{sat}}}{2T_R} \sqrt{\alpha^2 - \psi_{\text{dc}}^2}, \quad (4.44)$$

which occurs at the average optical intensity of

$$I_0 = 2E_{\text{sat}}/T_R. \quad (4.45)$$

This decrease of the BOMPD gain due to high energy pulses has an adverse effect on the phase noise according to (4.21). In addition to gain deterioration, high energy optical pulses of MLL increase the generation-recombination noise of the photodiodes. The GR noise variance of the photodiode is proportional to the square of the photocurrent and exceeds the shot noise at high illumination levels, as discussed in Section 4.1.2. Degradation of phase detector gain and enhancement of GR noise at high energy pulses have an adverse effect on BOMPD phase noise and for low phase noise OEPLL, using BOMPD in this operating region should be avoided.

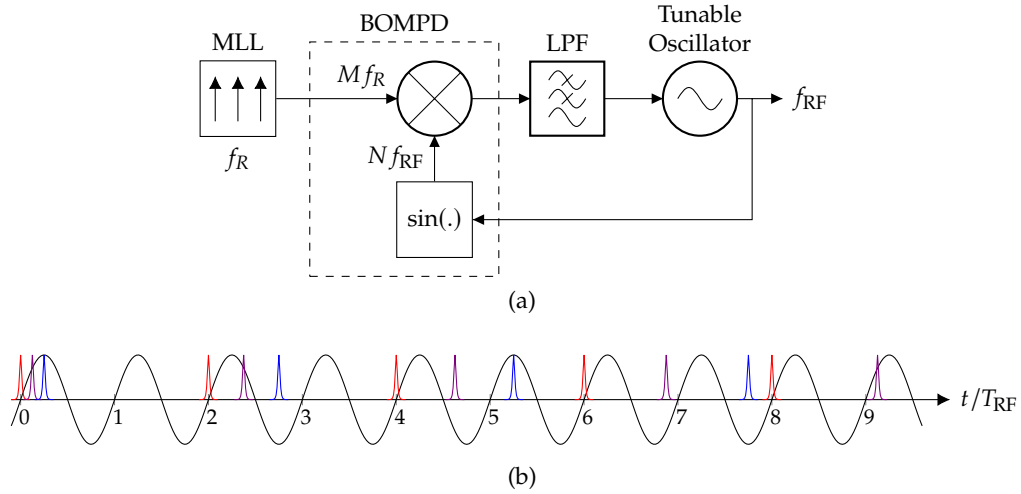


FIGURE 4.8: (a) OEPLL with nonlinear model of BOMPD, and (b) corresponding waveforms: (black) RF voltage waveform, (red) MLL pulses when $\omega_{\text{RF}}/\omega_R = 2$, (blue) MLL pulses when $\omega_{\text{RF}}/\omega_R = 2\frac{1}{2}$, (violet) MLL pulses when $\omega_{\text{RF}}/\omega_R = 2\frac{1}{4}$. The time axis is normalized to the RF signal period $T_{\text{RF}} = 1/f_{\text{RF}}$;

4.2.2 RF nonlinearity in BOMPD and interharmonic locking

Another nonlinear effect in BOMPD is the intrinsic nonlinear behavior of the BIM characteristic function. The RF voltage v_{RF} goes under a nonlinear transformation in BOMPD due to $\sin(\psi)$ term in (3.24). This nonlinear transformation leads to internal generation of harmonics of the RF signal which can be used for locking on interharmonics (non-integer harmonics) of the reference repetition rate [55]. This nonlinear behavior is illustrated in OEPLL block diagram in Figure 4.8(a) where the BOMPD is modeled with an ideal balanced frequency mixer and a nonlinear block $\sin(\cdot)$. The envelope of the MLL output contains integer multiples of its repetition rate Mf_R and the output of $\sin(\cdot)$ block contains integer multiples of the RF signal frequency Nf_{RF} . The necessary (but not sufficient) condition for phase locking is that

these frequencies are equal

$$f_{\text{RF}} = \frac{M}{N} f_R , \quad (4.46)$$

where M and N are positive integers with greatest common divisor (gcd) of 1. We call the operating regime of an OEPLL with $N = 1$ as harmonic locking and with $N > 1$ as the N 'th order interharmonic locking. Figure 4.8(b) illustrates the tunable oscillator waveform and the MLL pulses for $\omega_{\text{RF}}/\omega_R = 2, 2\frac{1}{2}$, and $2\frac{1}{4}$ corresponding to $N = 1, 2$, and 4 , respectively.

Now we derive the BOMPD characteristic function for the N 'th order interharmonic locking, $H_N(\phi)$. This can be achieved similar to what we did previously for the harmonic locking case, by imposing the interharmonic condition in (4.46) to (3.32). For the N 'th order interharmonic phase detection, the output differential intensity of BOMPD in (3.30) has a period of NT_R . Therefore, the N 'th order characteristic function of BOMPD, $H_N(\phi)$, can be written similar to (3.37) but with integration over a period of NT_R as

$$H_N(\phi) = \frac{1}{NT_R} \int_{0^-}^{NT_R^-} dt \, i = \frac{R_\lambda I_0}{N} \sum_{m=0}^{N-1} \sin \left[\alpha \sin \left(\frac{2\pi m}{N} + \phi \right) + \psi_{\text{dc}} \right] . \quad (4.47)$$

The index M in (4.47) was suppressed since we assumed $\text{gcd}(M, N) = 1$. The 1st, 2nd and 4th order characteristic functions of the BOMPD (corresponding to harmonic locking, 2nd order interharmonic locking and 4th order interharmonic locking, respectively) have a simple closed form and can be found using (4.47) as

$$H_1(\phi) = R_\lambda I_0 \sin[\alpha \sin(\phi) + \psi_{\text{dc}}] , \quad (4.48)$$

$$H_2(\phi) = R_\lambda I_0 \sin(\psi_{\text{dc}}) \cos[\alpha \sin(\phi)] , \quad (4.49)$$

and

$$H_4(\phi) = \frac{1}{2} R_\lambda I_0 \sin(\psi_{\text{dc}}) [\cos(\alpha \sin(\phi)) + \cos(\alpha \cos(\phi))] . \quad (4.50)$$

The first order characteristic function is indeed for the harmonic locking case and is the same as (3.37), but the derivation has been done again in this section for the sake of completeness. Equations (4.49) and (4.50) show that the 2nd and 4th order characteristic functions linearly scale with $\sin(\psi_{\text{dc}})$ and become zero when $\psi_{\text{dc}} = 0$. This is expected since the nonlinear characteristic function of the BOMPD in (3.30) has even symmetry with respect to v_{RF} at $\psi_{\text{dc}} = \pm\pi/2$ and odd symmetry at $\psi_{\text{dc}} = 0$. With a single tone excitation, only odd harmonics at $\psi_{\text{dc}} = 0$ and only even harmonics at $\psi_{\text{dc}} = \pm\pi/2$ are generated. The BOMPD characteristic curves for different values of α are plotted in Figures 3.6(a), (b), and (d), respectively.

The 2nd and 4th order characteristic curves do not have a zero crossing for all RF excitation amplitudes, which is necessary for type II PLLs as discussed in Section 3.1. A zero crossing can be guaranteed by proper selection of α such that the BOMPD characteristic function has a zero average. The average of $H_N(\phi)$ can be found using Jacobi-Anger expansion of (4.47) as

$$\langle H_N(\phi) \rangle_{\phi} = R_\lambda I_0 \sin(\psi_{\text{dc}}) J_0(\alpha) , \quad (4.51)$$

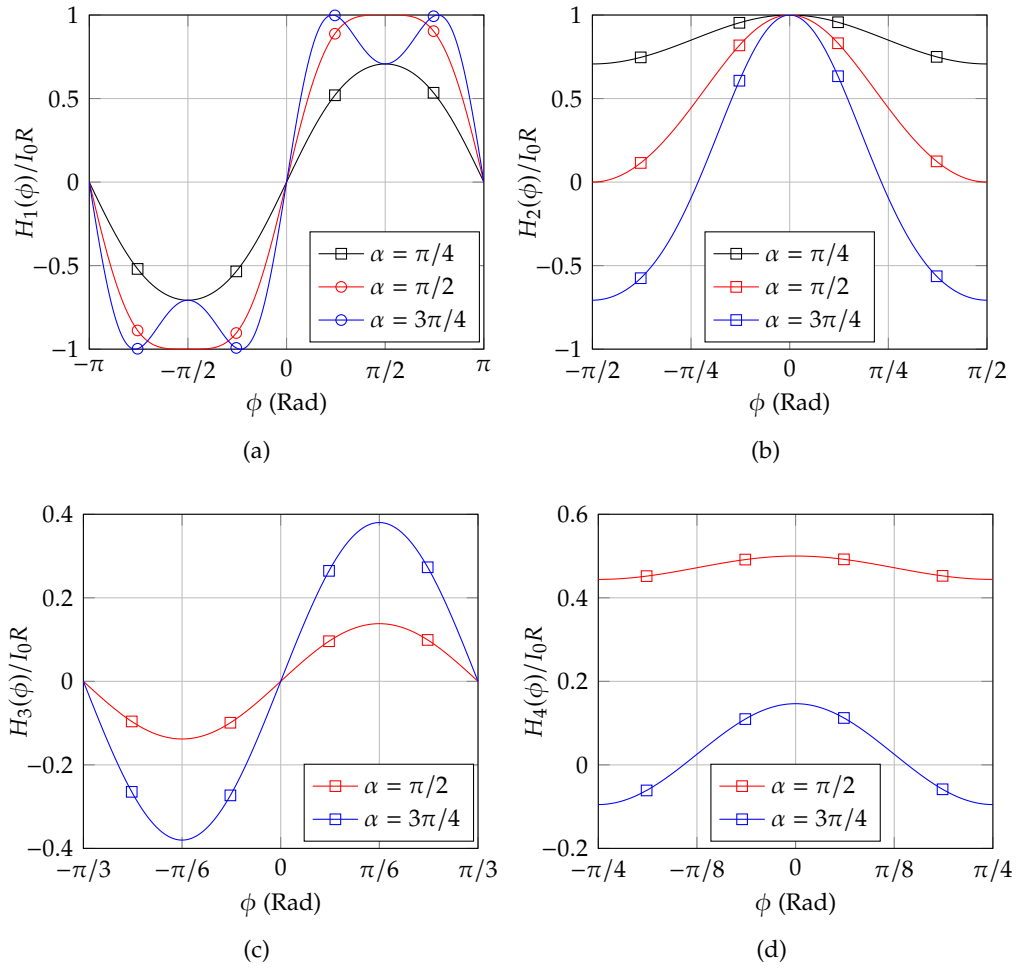


FIGURE 4.9: BOMPD characteristic curves for (a) harmonic locking at $\psi_{dc} = 0$, (b) 2nd order interharmonic locking at $\psi_{dc} = \pi/2$ and (c) 4th order interharmonic locking at $\psi_{dc} = \pi/2$ for different RF amplitudes: (black) $\alpha = \pi/4$, (red) $\alpha = \pi/2$ and (blue) $\alpha = 3\pi/4$.

where $\langle . \rangle_\phi$ denotes averaging with respect to variable ϕ and J_0 denotes the Bessel function of the first kind of order 0. A zero-average $H_N(\phi)$ guarantees a zero-crossing in the transfer characteristic which is necessary for operating the BOMPD in an OEPLL, as discussed in Section 3.1. Proper operation of the OEPLL requires coarse tuning of the tunable oscillator around the desired frequency which can be very close to another interharmonic frequency of the same or different order. Therefore, although a zero-crossing in the characteristic function can be generated by having sufficient RF amplitude, locking the OEPLL on very high order interharmonics can be practically difficult.

4.3 Summary and conclusion

In this chapter, we expanded the theory of OEPLL beyond system level simulation and characteristic functions of BOMPD which were derived in the previous chapter. Different noise sources in BOMPD were modeled and their effects of the BOMPD phase noise were discussed. The phase noise of the OEPLL can consequently be estimated using the system level transfer functions and the BOMPD phase noise. In

addition, modeling the undesired noise sources shows different mechanisms that might degrade the phase noise of OEPLL. The nonlinear analysis provided in this chapter shows the limitations of the OEPLL with respect to the intensity of the optical input and how much improvement or degradation can be expected if higher optical intensities are used. This theory provides a systematic approach to design an OEPLL and to choose various design parameters properly, such as the intensity of the optical input, photodiode selection according to its bandwidth and rated power, proper biasing of the intensity modulator and the required noise level of its biasing voltage and tunable oscillator parameters such as its tuning sensitivity and phase noise.

Chapter 5

Design, Simulation and Characterization of OEPLL

So far, the operating principle of OEPLL and the mathematical model along with the necessary equations have been introduced. In this chapter, first the BOMPD is designed and characterized. Then two OEPLLs are demonstrated with different classes of building blocks and the results are compared. Partial results presented in this chapter are published in [author's publication, 18, 53–56].

5.1 BOMPD design and characterization

In Chapter 3, the balanced optical microwave phase detector (BOMPD) was modeled using a lossless balanced intensity modulator (BIM) in (3.24). In practice, BIMs have a few dBs of insertion loss. This loss can simply be included in the BIM characteristic function as

$$I_y^\pm = \frac{I(t)}{2} L_{\text{BIM}} [1 \pm \sin(\psi)] , \quad (5.1)$$

where L_{BIM} is the modulator loss. Another approach is to incorporate this loss by referring to the total average output power, rather than the input power. Therefore, for practical reasons, in this chapter we usually refer to the average output power of BIM or the input power of the BOMPD photodiodes.

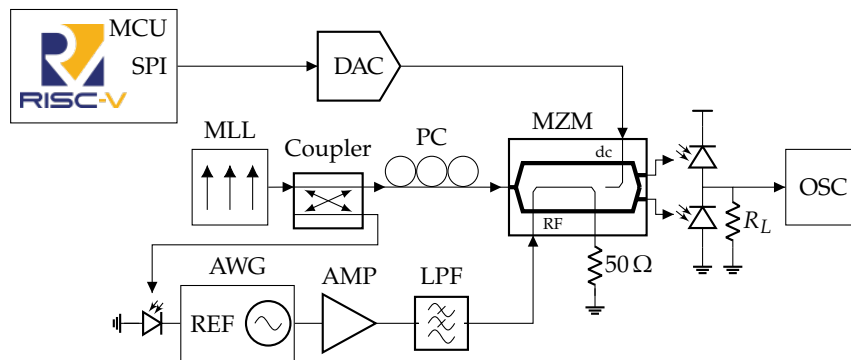


FIGURE 5.1: (a) Test setup for characterization of BOMPD. MCU, micro-controller unit; DAC, digital to analog converter; MLL, mode-locked laser; MZM, Mach-Zehnder modulator; PC, polarization controller; AWG, arbitrary waveform generator; OSC, oscilloscope; AMP, amplifier; LPF, lowpass filter.

The BOMPD is realized via a balanced MZM with complementary outputs operating at 1550 nm wavelength. The modulator has a bandwidth of 20 GHz, a π -voltage

of 5 V for the RF electrode and a π -voltage of 10 V for the DC electrode. This π -voltage corresponds to an α of 0.2π for an RF excitation level of 10 dBm in 50 Ω system according to (3.34). A pair of InGaAs photodiodes with an active area of 120 μm^2 convert the intensity of the optical outputs to an electrical current. The photodiodes have a responsivity of 1 A/W.

In order to measure the characteristic function, the RF signal applied to the RF electrode must be synchronized with the optical input. A simple approach is to convert a weak coupling of the MLL optical signal to electrical domain via a photodiode and apply it to the signal generator as its reference input. The BOMPD characteristic function describes the output current versus the phase difference between the RF signal and the desired harmonic or interharmonic of the optical reference repetition rate. Therefore, introducing a sweeping phase shift to the RF signal is necessary. This phase shift can simply be realized by an offset frequency between the RF signal and the desired harmonic or interharmonic frequency

$$f_{\text{RF}} = \frac{M}{N} f_R + \Delta f, \quad (5.2)$$

where f_{RF} is the frequency of the RF excitation signal, f_R is the reference repetition rate, Δf is the offset frequency and M and N are positive integers with $\text{gcd}[M, N] = 1$.

Figure 5.1 shows the test setup for BOMPD characterization. A low-pass filter is used to filter the harmonics of the RF signal, guaranteeing the single-tone stimulation of the modulator according to (3.29). Since the MZM is polarization sensitive, a polarization controller is used to adapt the polarization of the light with the polarization required by the modulator. A load resistance of 1 k Ω converts the BOMPD output current to a voltage which is then monitored by a real-time oscilloscope. The MZM bias point is set via a DAC which is controlled via a RISC-V microcontroller uploaded with a MicroPython firmware. The MZM bias control is performed in an open-loop fashion. The required bias voltages for the desired operating points are measured separately and stored in a lookup table inside the microcontroller.

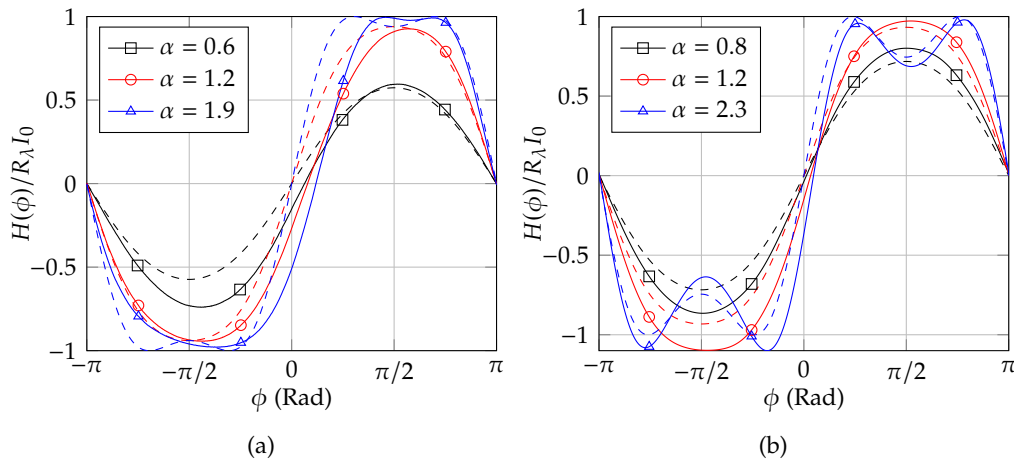


FIGURE 5.2: Phase detector characteristic curves for harmonic locking at different RF excitation amplitudes (a) without RF signal harmonic filtering and (b) with RF signal harmonic filtering.

Figure 5.2 compares the measured phase detector characteristic function for different RF excitation amplitudes with the theoretical one derived in Chapter 3. Figures 5.2(a) and 5.2(b) also compare the effect of filtering the RF harmonics on the

shape of the characteristic function. While the BOMPD curves characterized with filtered RF signal show better matching with the theory, the curves measured with unfiltered RF signal are still in agreement with the theory and BOMPD is still capable to function properly with sufficient phase detection gain at the zero crossing.

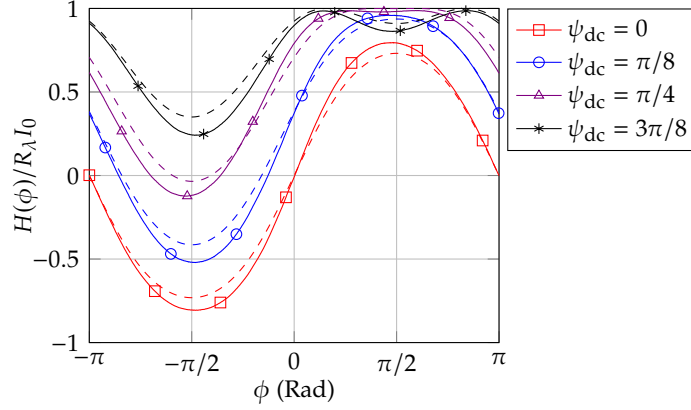


FIGURE 5.3: (solid) Measured and (dashed) theoretical phase detector characteristic curves at $\alpha = 0.8$ for different bias points.

In order to verify the theory with respect to the offset phase shift introduced by the dc electrode, the characteristic functions have been measured for different values of ψ_{dc} and are plotted in Figure 5.3. The BOMPD characteristic functions show the behavior predicted by the theory developed in Chapter 3 with respect to the independent variables ϕ and ψ .

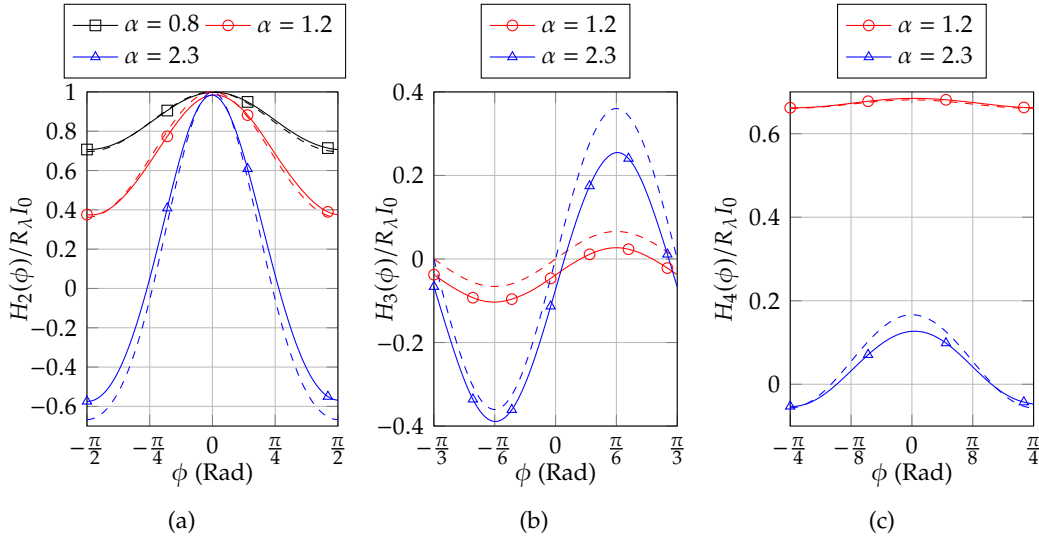


FIGURE 5.4: BOMPD characteristic curves according to (dashed) theory and (solid) measurement for (a) 2nd order interharmonic locking at $\psi_{dc} = \pi/2$, (b) 3rd order interharmonic locking at $\psi_{dc} = 0$ and (c) 4th order interharmonic locking at $\psi_{dc} = \pi/2$.

The setup illustrated in Figure 5.1 has also been used for characterization of the 2nd, 3rd and 4th interharmonic phase detection corresponding to $N = 2, 3$ and 4 in (5.2). The measurement results are plotted in Figure 5.4 and prove an excellent agreement with the theory developed in Chapter 3. The interharmonic characteristic curves show that the BOMPD gain decreases as the interharmonic order increases.

The BOMPD gain and variation of the 3rd and 4th order characteristic functions (with respect to ϕ) are very low at low RF excitation levels. The variation of the 3rd and 4th order characteristic curves is barely visible at $\alpha = 0.8$ and is not plotted.

5.2 OEPLL design and characterization

In this section two different designs of OEPLL are demonstrated. Design I uses a semiconductor VCO as its tunable oscillator and design II uses an YIG tunable oscillator. YIG oscillators generally have resonators with higher quality factors compared to semiconductor VCOs and it is expected to get better phase noise results with design II. Both tunable oscillators are selected such that they cover at least one octave of frequency range (from f_0 to $2f_0$). This condition is necessary for frequency range extension, such that any frequency can be synthesized from the tunable oscillator output using just a chain of frequency dividers and frequency multipliers, as illustrated graphically in Figure 5.5. If the frequency range of the tunable oscillator is less than one octave, there will be frequency gaps in Figure 5.5 which is undesired for ultra wideband frequency synthesizers.

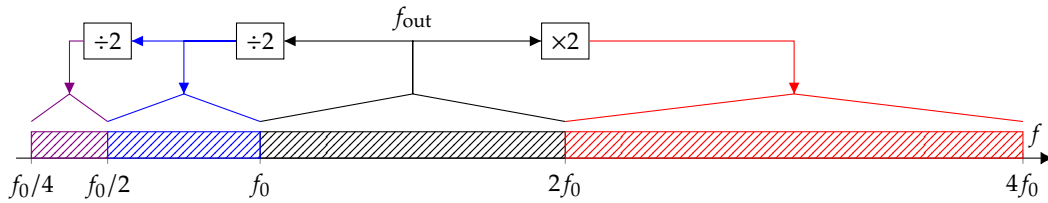


FIGURE 5.5: Extending the frequency range of frequency synthesizer using frequency multiplier and frequency divider chain.

5.2.1 Design I: OEPLL with semiconductor VCO

Figure 5.6 shows the block diagram of the OEPLL using a semiconductor VCO. The details of BOMPD implementation are given in the previous section. In Section 4.1.2 it was shown that high energy optical pulses as well as pulsed stimulation of photodiodes leads to enhancement of generation-recombination noise in photodiodes above the shot noise limit. Therefore, we limited the average output optical power of the MZM to 1 mW. The optical reference is an Origami-series femtosecond MLL from OneFive (now NKT Photonics) with a wavelength of 1550 nm, a pulse duration of 200 fs and a repetition rate of 76MHz. The MLL is also equipped with piezo actuators for repetition rate stabilization. However, if the repetition rate is not stabilized, vibration of the actuators causes phase noise degradation at close-in offset frequencies below a few kHz.

The phase noise of a similar MLL with a repetition rate of 214 MHz has been characterized by the manufacturer by selecting the 14th harmonic of its intensity waveform detected by a photodiode and is plotted in Figure 5.7(a). The measurement setup is similar to Figure 1.5(a). The phase noise is expected to further decrease at offset frequencies above 500 kHz, but it is limited to the measurement setup noise floor.

Equation (3.23) shows the phase noise contribution of the loop filter is, on the one hand, directly proportional to the tuning sensitivity of the tunable oscillator K_V , and on the other hand, is inversely proportional to the phase detector gain K_ϕ . Having a

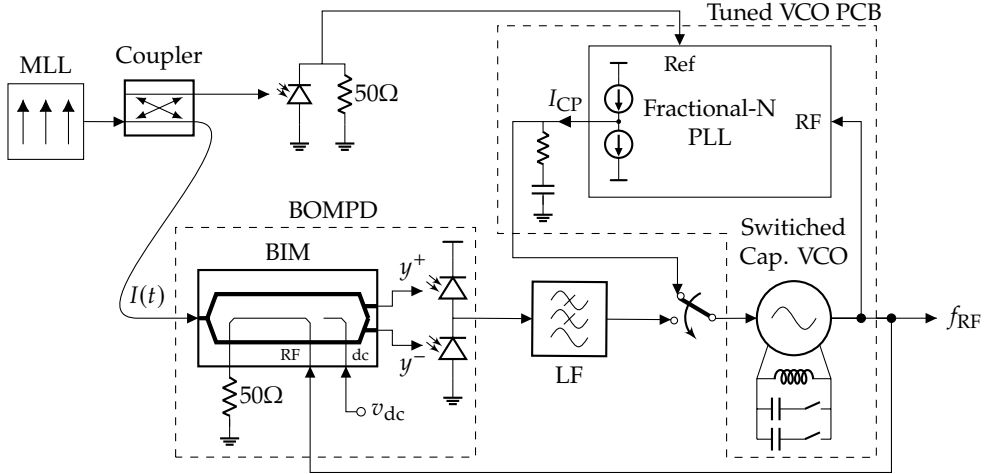


FIGURE 5.6: Block diagram of OEPLL design I with semiconductor VCO.

high K_V can also be problematic from a practical point of view. The loop filter resistor is inversely proportional to K_V according to (3.20) and a high tuning sensitivity can result in an Ohms range resistance. Such a low resistance can be within the range of the equivalent series resistance (ESR) of the loop filter capacitor. As a result, one has to model the loop filter components with higher precision which adds to the overall design complexity. Therefore, VCOs with low tuning sensitivities are desired.

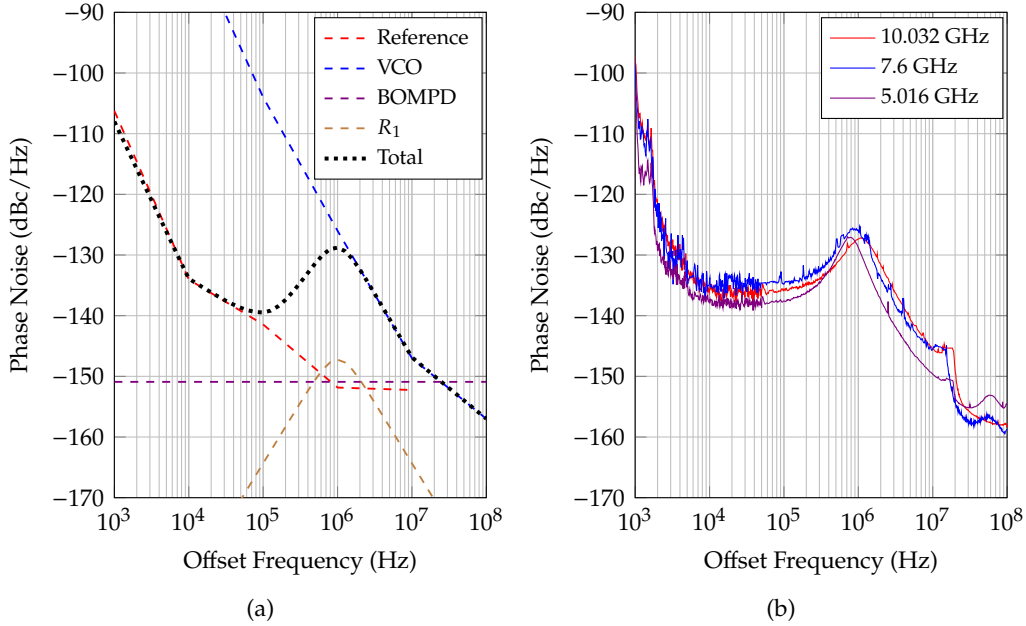


FIGURE 5.7: Phase noise of OEPLL design I with semiconductor VCO, (a) simulated and (b) measured.

Extending the frequency range of the OEPLL without any frequency gaps requires a VCO with at least one octave of frequency range. Unfortunately, such VCOs usually have high tuning sensitivities and this leads to the increase of the resistor noise contribution to the overall phase noise, as discussed in Section 3.2. While wideband VCOs have tuning sensitivities in the range of a few hundreds of megahertz per volt,

switched-capacitor VCOs offer an order of magnitude lower tuning sensitivities, as they break the frequency band into different sub-bands. Therefore, a multi-core octave-band switched capacitor VCO with a frequency range of 5–10 GHz is used to keep the tuning sensitivity below 100 MHz/V. Another advantage of this design choice is that it limits the bandwidth of each VCO core to approximately 100 MHz and the PLL can lock at maximum two of the reference harmonics, since the reference repetition rate is 76 MHz. Therefore, the designer has better control over the reference harmonic the VCO locks into.

Figure 5.7(a) shows the calculated phase noise of the OEPLL at 10 GHz carrier frequency according to the system level theory in Section 3.2. Since the MLL repetition rate is relatively low, the loop is designed for 1 MHz bandwidth to suppress the harmonics of the reference intensity waveforms. At offset frequencies approximately below 3 kHz the OEPLL phase noise is dominated by the optical reference, and at offset frequencies above 1 MHz the OEPLL phase noise is dominated by the VCO noise. The noise of BOMPD and the loop filter resistor R_1 is below that of the reference and the VCO and has negligible effect on the overall phase noise. The noise of BOMPD and the loop resistor is not very critical in this OEPLL, however it is expected to see their effect in OEPLLs which have tunable oscillators with lower phase noise levels. The measured phase noise for three carrier frequencies at the beginning, in the middle and at the end of the frequency range is plotted in Figure 5.7(b). The phase noise was measured using APPH20G phase noise analyzer from Anapico. (For an overview of phase noise measurement techniques please see Appendix F.)

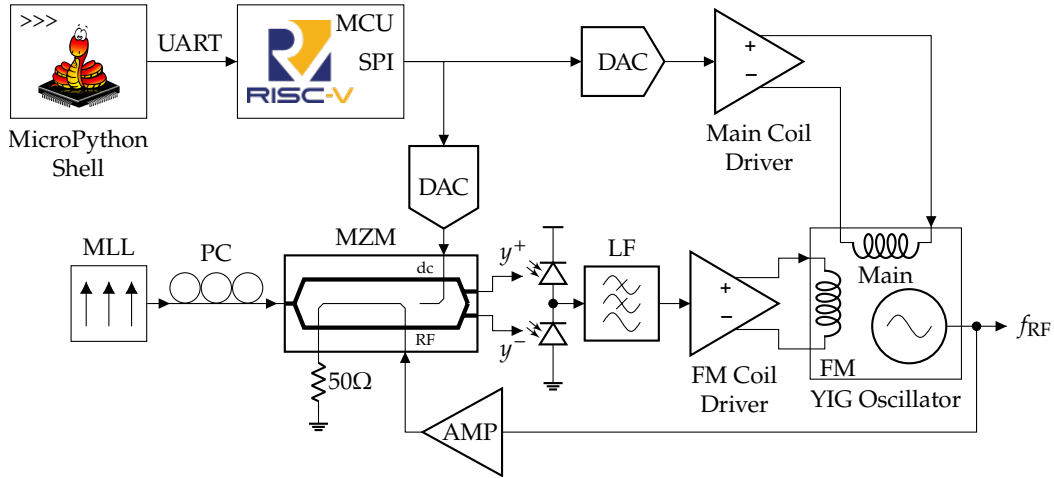


FIGURE 5.8: Block diagram of OEPLL design II with YIG oscillator; MCU, microcontroller unit; DAC, digital to analog converter; MLL, mode-locked laser; MZM, Mach-Zehnder modulator; PC, polarization controller; LPF, low-pass filter; YIG, Yttrium Iron Garnet.

5.2.2 Design II: improved OEPLL with YIG oscillator

Figure 5.8 shows the block diagram of the 2nd version of the OEPLL. The core of this diagram is similar to the basic OEPLL block diagram shown in Figure 3.4(a). The optical reference is a MLL from Menhir Photonics with a center wavelength of 1560 nm, a repetition rate of 250 MHz and a pulse width below 200 fs [12]. The BOMPD was implemented with a lithium niobate MZM with complementary outputs and a pair of InGaAs photodiodes to convert the optical output of the MZM to an electrical current. The output current pulses of the photodiode pair are then integrated via

a series RC loop filter and converted to a voltage as discussed in Section 3.2. Since the MZM performance is sensitive to the polarization of the input optical field, a polarization controller is placed between the MLL and the MZM to align the polarization of the input field with the required polarization of the MZM. The dc voltage of dc-electrode of the MZM is set via a low-noise DAC.

An Yttrium Iron Garnet (YIG) oscillator with a bandwidth of 2–20 GHz is used as a tunable oscillator, because of its high bandwidth and low phase noise. The main coil of the YIG oscillator has a high tuning sensitivity and is used to coarse-tune the frequency. The current of this coil is set via a current driver circuit and a low-noise DAC. The FM coil is driven with a low-noise operational amplifier (OpAmp) which gets its input voltage from the loop filter output voltage.

The low-noise DACs are programmed via SPI interface. The SPI commands are sent from a RISC-V open-source instruction set microcontroller. The microcontroller is loaded with MicroPython firmware and receives Python commands from a computer.

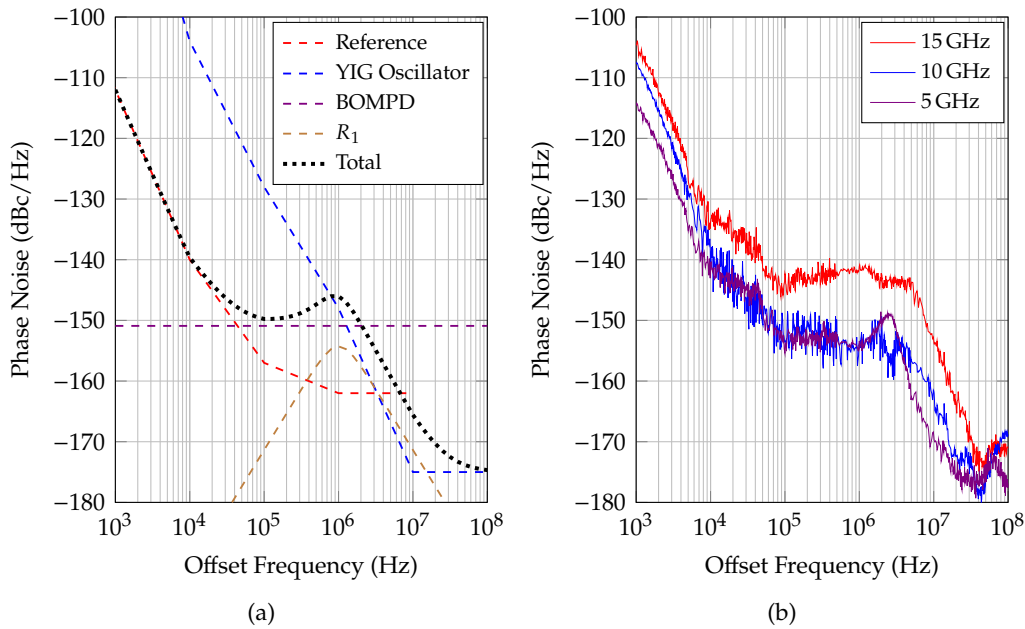


FIGURE 5.9: Phase noise of OEPLL design II with YIG oscillator, (a) simulated and (b) measured.

The PLL loop filter components were designed for a target loop bandwidth using the procedure explained in Section 3.2 similar to the charge pump PLLs [19]. The designed values were then optimized using the AC simulation engine of the Keysight Advanced Design System (ADS) tool to achieve the target loop bandwidth and phase margin. On the one hand, the in-band phase noise of the output signal is dominated by the sum of the phase noise of the frequency reference (MLL) and the phase detector (BOMPD) according to (3.10). On the other hand, the out-of-band phase noise is mainly determined by the phase noise of the tunable oscillator (YIG oscillator) according to (3.12). Therefore, a good choice of loop cut-off frequency would be at the intersection of these phase noise plots. However, the optimum loop bandwidth for minimum integrated rms-jitter could be lower than the loop bandwidth found using the procedure explained. This is mainly because the high-pass behavior of the output phase to the tunable oscillator phase transfer function is not ideal and has a transition band. The contribution of the phase noise of the BOMPD in this

transition band can be significant, since the jitter scales linearly with the frequency. As a result, shifting the loop bandwidth even by a few hundreds of kilohertz to higher frequencies would result in significant increase of the integrated rms-jitter as the phase noise of the BOMPD is higher than the phase noise of the tunable oscillator in the transition band.

Figure 5.9(a) shows the calculated phase noise of the output signal of the OEPLL at 10 GHz carrier frequency along with the open-loop phase noise of the reference, the phase detector and the YIG oscillator. The phase noise data of the MLL and the YIG oscillator have been provided by the manufacturer. The loop bandwidth is approximately 1 MHz and the cut-off frequency of the closed-loop system can be seen as a bump in the phase noise plot of the output of the OEPLL. At very low offset frequencies below 10 kHz, the phase noise is dominated by the phase noise of the reference, and the phase detector does not have a significant contribution to the overall phase noise. In the intermediate offset frequency range inside the loop bandwidth, from 10 kHz to 500 kHz, the output phase noise is mainly dominated by the phase noise of the phase detector. Outside the loop bandwidth at offset frequencies above 500 kHz, the output phase noise reaches the phase noise of the YIG oscillator. At frequencies close to the loop cut-off frequency, the output phase noise is mainly determined by the phase noise of the YIG oscillator and the phase detector. The bump at the cut-off frequency is due to higher phase noise of the YIG oscillator at the cut-off frequency.

5.3 Interharmonic OEPLL

In Section 4.2.2 the theory of a new regime in OEPLL was presented and it was shown that the OEPLL can also lock on the interharmonics of the optical reference repetition rate. This operating regime can also be confirmed in theory using the same OEPLL block diagram shown in Figure 5.8. It was discussed earlier that the phase detector requires a zero crossing in the characteristic curve. The reason is that a PLL with type II loop filter has an average zero phase detector output. This zero crossing easily achieves for 1st and 3rd order characteristic curves by setting the modulator bias point at $\psi_{dc} = 0$. However, this is not allowed for even order interharmonic locking since it entirely nulls the characteristic curve according to (4.49) and (4.50). In order to make sure this zero crossing happens, the YIG oscillator signal is first amplified and then applied to the modulator. The amplification leads to additional RF harmonic generation that might have a positive or negative effect on the phase detector gain and can shift the BOMPD characteristic curves toward positive or negative values (in reference to Figures 4.9). Therefore, an experimental approach was adapted; the modular was initially biased at $\psi_{dc} = \pi/2$ and then fine tuned around this point to achieve locking. This has been sufficient for our experiment to achieve a stable locking. It is noteworthy that other tweaking techniques are possible, such as attenuation of one of MZM outputs to shift the curves up or down, or adding a current source at the balanced photodiode output node to control its zero-crossing. The optical power is also usable as another degree of freedom to control the phase detector gain and the loop bandwidth.

Figure 5.10 shows the OEPLL output spectrum over a frequency span of 1 GHz at 10 GHz, 10.125 GHz, 10.083 GHz and 10.0625 GHz carrier frequencies corresponding to harmonic locking, 2nd, 3rd and 4th order interharmonic locking, respectively. A

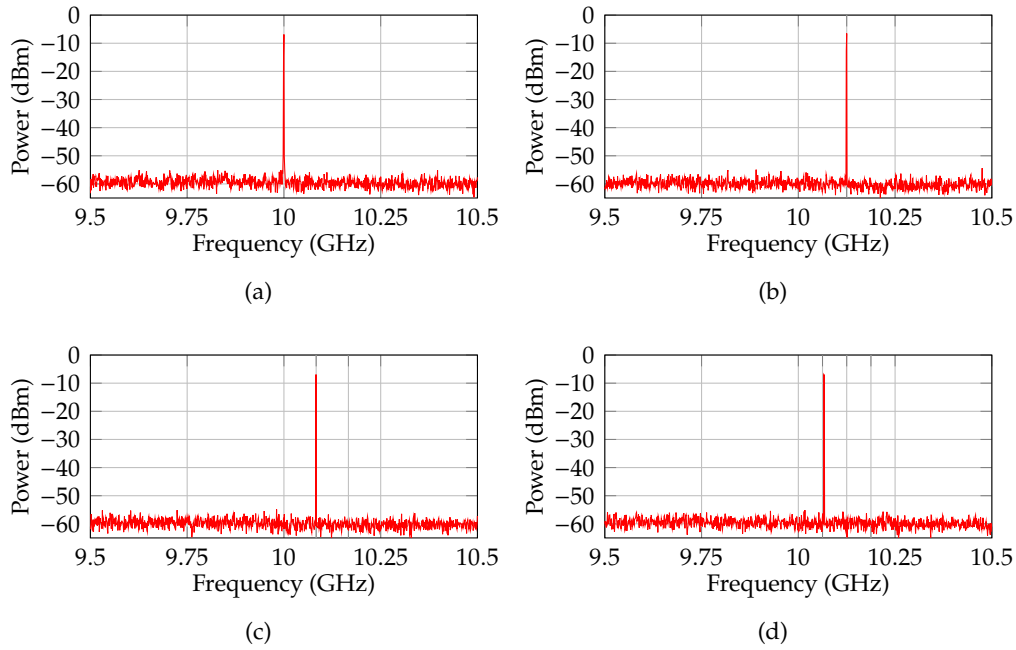


FIGURE 5.10: Power spectrum of the OEPLL output signal at (a) 10 GHz corresponding to harmonic locking, (b) 10.125 GHz corresponding to 2nd order interharmonic locking, (c) 10.083 GHz corresponding to 3rd order interharmonic locking and (d) 10.0625 GHz corresponding to 4th order interharmonic locking.

handheld spectrum analyzer from Anritsu (MS2760A) was used for the measurement. The OEPLL does not show any spurs within 50 dBc with respect to the carrier level. The measurement noise floor was limited by the noise of the spectrum analyzer.

The phase noise of the OEPLL has also been characterized at interharmonic frequencies and is plotted in Figure 5.11. The OEPLL phase noise at interharmonic frequencies is comparable to the phase noise at harmonic frequency locking. The loop bandwidth for the harmonic locking and 2nd order interharmonic locking is slightly above the optimum point around 1 MHz. This increase in the loop bandwidth shifts the PSD of the noise of the loop filter resistor R_1 (see Figure 5.9(a)) to higher offset frequencies and slightly degrades the out-of-band phase noise. The loop bandwidth can of course be adjusted by simply reducing the optical power or re-designing the loop filter. The phase noise plot for the second order interharmonic locking at 10.125 GHz shows a slight bump around 100 MHz offset frequency. The reason for this bump is not clear to us, but we expect to be able to suppress it by filtering the control voltage of the tunable oscillator after the YIG driver stage.

5.4 Summary and conclusion

In this chapter, we verified the OEPLL theory given in Chapter 3. First, a design procedure for the BOMPD was given and then the BOMPD characteristic curves with respect to different degrees of freedom were measured. The measurement results for both harmonic locking and interharmonic locking show a good agreement between the theory and the practice. We also showed two examples of OEPLL, design I with a semiconductor VCO and design II with a YIG oscillator. The design methodology was based on the system level analysis of the OEPLL given in Chapter 3. The OEPLL

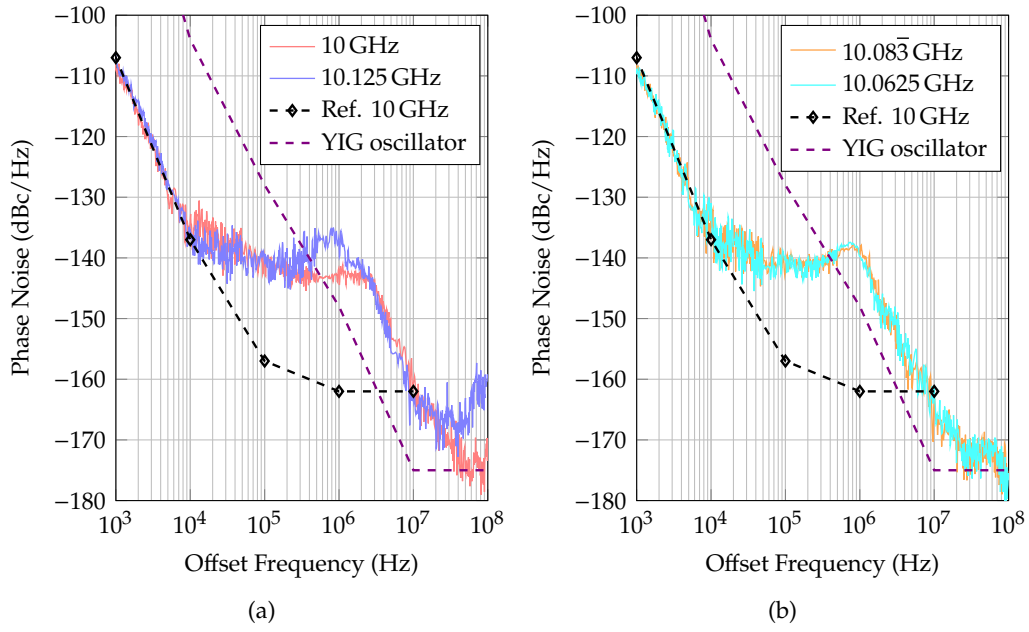


FIGURE 5.11: Measured phase noise of the OEPLL output signal at (red, left) 10 GHz, (blue, left) 10.125 GHz, (orange, right) 10.083 GHz and (cyan, right) 10.0625 GHz carrier frequencies corresponding to harmonic locking and 2nd, 3rd and 4th order interharmonic locking, respectively, (dashed black) phase noise of the MLL reference scaled to 10 GHz carrier frequency and (dashed violet) phase noise of the YIG oscillator.

with semiconductor VCO can lock on any harmonic of the optical reference in the frequency range of 5–10 GHz. The OEPLL with YIG oscillator has a wider frequency range 2–20 GHz, thanks to the high bandwidth of the YIG oscillator. In addition, the OEPLL with YIG oscillator has better phase noise performance due to lower phase noise of the YIG oscillator and its lower tuning sensitivity. Finally, design II was used to characterize the OEPLL at interharmonic frequencies. The phase noise performance of the OEPLL at interharmonic frequencies is comparable to that at harmonic frequencies. The OEPLL can lock on harmonics and up to 4th order interharmonics of the reference repetition rate within its output frequency range 2–20 GHz.

Chapter 6

Conclusion and Outlook

6.1 Comparison with the state of the art

Figure 6.1 compares the phase noise of the OEPLL (design I and II) with the best state-of-the-art laboratory signal generators as well as OEPLLs from other groups. Compared to the state-of-the-art wideband laboratory signal generators, E8257D from Keysight, SMW200A from Rohde & Schwarz and MSG36241A from Anritsu [30–32], the OEPLL shows superior phase noise performance at offset frequencies above 2 kHz, especially in the intermediate frequency range below 500 kHz which lies inside the loop bandwidth. The phase noise performance of the OEPLL and the-state-of-the-art frequency synthesizers is similar at the offset frequencies above approximately 1 MHz which is outside the loop bandwidth (at 10 GHz carrier frequency). This can be attributed to similar tunable oscillator technology for both the state of the art and the OEPLL. At offset frequencies below 2 kHz, the phase noise of the state-of-the-art instruments follows the quartz oscillator phase noise which is better than that of the MLL and consequently better than that of the OEPLL design I and II. This poor performance at lower frequencies below 2 kHz can indeed be improved by locking the MLL on a quartz reference or using more sophisticated methods such as OFD.

The OEPLL with VCO (Design I) has a slightly better in-band phase noise performance at offset frequencies in the range of 2–200 kHz compared to state-of-the-art frequency synthesizers. At close-in carrier offset frequencies below 2 kHz, the phase noise is limited by the MLL which is expected to improved if the MLL repetition rate is locked to a quartz reference or using best-in-class OFD optical sources. At offset frequencies above 200 kHz the OEPLL phase noise is limited by the semiconductor VCO phase noise. Laboratory-grade frequency synthesizers usually use YIG oscillators and have better phase noise at these offset frequencies, as YIG oscillators have resonators with higher quality factors and consequently better phase noise.

The OEPLL with YIG oscillator (Design II) has superior performance compared to the state-of-the-art frequency synthesizers almost at all offset frequencies above 2 kHz. Compared to the OEPLL with VCO (Design I) reported in [author’s publication, 53], this work has better phase noise at almost all offset frequencies. The main reason for this improvement is using a YIG oscillator instead of an integrated VCO. The phase noise of OEPLL (Design II) at other carrier frequencies can be found in Appendix G.

The phase noise performance of the OEPLL reported in [28] is similar to OEPLL with YIG oscillator at offset frequencies below 10 kHz. However, the OEPLL in [28] has lower phase noise at offset frequencies above 10 kHz. The superior performance of [28] at higher offset frequencies is mainly due to the lower open-loop phase noise of the DRO used as the tunable oscillator. Also, our OEPLL optical power budget is limited by the photodiodes and increasing the optical power has an adverse effect on the generation-recombination noise of the photodiodes. By optimizing the

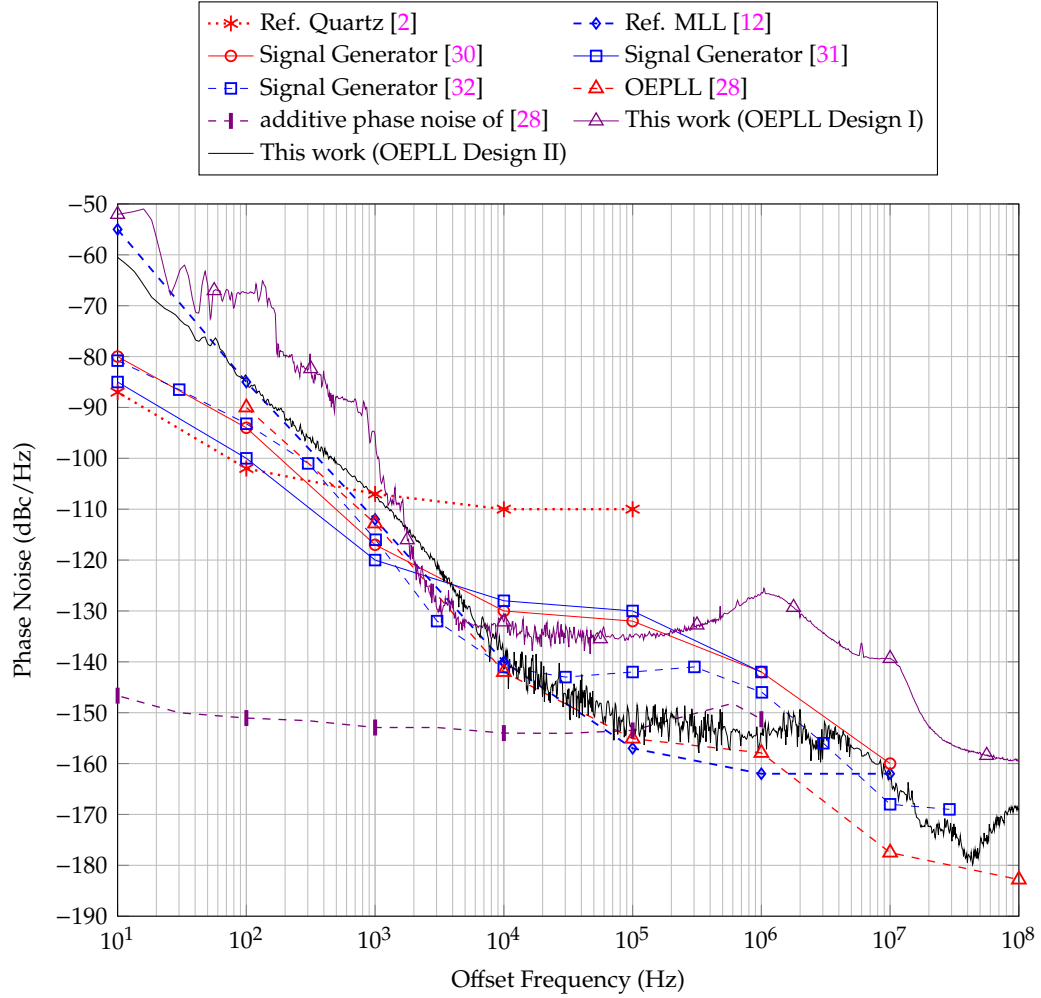


FIGURE 6.1: Phase noise comparison of microwave frequency synthesizers at 10 GHz and frequency references normalized to 10 GHz carrier frequency. OEPLL Design I uses a VCO and OEPLL Design II uses a YIG oscillator.

photodiode illumination condition or using photodiodes with larger active area, the optical power can be increased to reduce the BOMPD phase noise without being limited by the photodiode generation-recombination (GR) noise. The additive phase noise of the OEPLL reported by Jung *et al.* [28] has been measured in [27] and can be compared with that of our OEPLL. The additive phase noise of this work can be considered as the difference between the reference phase noise and the output signal phase noise. Since the phase noise of the tunable oscillator is suppressed inside the loop bandwidth, the main source of the additive phase noise is the phase detector noise. This explains the approximately flat shape of the additive phase noise in [27], as the source of the phase detector noise is the shot noise of the photodiodes. Although the additive phase noise of this work was not measured, its in-band level can be estimated to be the phase detector noise (approximately -150 dBc/Hz). The phase detector noise can be observed at lower carrier frequencies (see Appendix G), where the reference phase noise is well below the phase detector noise. The phase detector noise shows itself as a plateau in the frequency range between 20 kHz and 2 MHz. Therefore, the inside-loop additive phase noise of this work is 4 dB higher than that of the OEPLL reported in [27] which is -154 dBc/Hz normalized to 10 GHz

carrier frequency.

The phase noise of our OEPLL can be compared with other RF signal generation methods such as SLCO and direct detection of the optical pulse whose phase noise are plotted in Figure 1.1. The SLCOs reported in [5, 6] perform better than this work because of superior performance of SLCO compared to our MLL and also the phase noise of the BOMPD inside the loop bandwidth. The additive noise of the direct detection scheme is usually limited by the difference of the RF power to the thermal noise floor which can be improved by increasing the RF power using the pulse interleaving technique and high-power photodiodes. Therefore, a combination of the best-in-class MLL and a direct detection receiver has a better phase noise than that of this OEPLL by more than two orders of magnitude [6, 14]. Although these works have lower phase noise, they have a single frequency output whereas our OEPLL has an output frequency range of 2–20 GHz.

6.2 Outlook

The reported OEPLL is capable of locking on the harmonics and the interharmonics of the repetition rate of MLL. It was shown that the phase noise at close-in offset frequencies is limited by the MLL phase noise. Therefore, synchronizing the MLL with a precise quartz source can improve the phase noise at close-in offset frequencies. In addition, many modern RF systems require synchronization of multiple RF generators. Therefore, synchronization of the MLL and consequently the OEPLL with another reference seems more necessary. It is noteworthy that the OEPLL can also use state-of-the-art optical references such as the OFD system reported in by Xie *et al.* [13] or the solid-state MLL reported by Kalubovilage *et al.* [14] to improve the closer-in carrier phase noise by orders of magnitude.

In addition to phase noise improvement, the OEPLL output signal can be mixed by a sub-Hertz-resolution frequency synthesizer to improve the frequency resolution. The mixing scheme can be a simple multiplication of the OEPLL output signal by a fine-resolution frequency synthesizer which is based on fractional PLL or a direct digital synthesis (DDS) [86]. An alternative approach which is more suitable for wideband signal generation is using offset PLL architecture [87].

Finally, integration of the OEPLL on a photonic integrated circuit (PIC) chip either by using InP, silicon photonics (SiP) or lithium niobate-on-insulator (LNOI) technology platforms is an interesting possibility to reduce the overall cost and size of the system. The integrated MZMs currently do not offer excellent specifications such as the ones offered by LiNbO₃ technology, but there is wide research to improve their loss and modulation efficiency that can benefit the MLL-based frequency synthesizers.

Appendix A

Phase Noise, Timing Jitter and Amplitude Noise

A.1 Phase noise and timing jitter

Phase noise is defined as the random variations of the phase of a sinusoidal signal $x(t)$ as

$$x(t) = x_0 \cos(\omega_0 t + \phi_0 + \phi_n(t)), \quad (\text{A.1})$$

where x_0 is the amplitude, ω_0 is the angular frequency, ϕ_0 is the offset phase and $\phi_n(t)$ is phase noise. This random variations is illustrated graphically in Figure A.1.

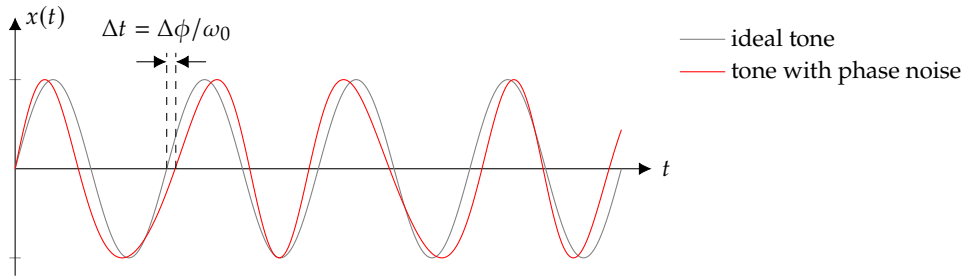


FIGURE A.1: Illustration of phase noise in a sinusoidal signal.

Like any other random process, it is meaningful to talk about the statistical properties of phase noise rather than its instantaneous value. Assuming phase noise is ergodic (that is the temporal averages are equal to the ensemble averages), the autocorrelation function of the phase noise can be written as

$$R_{\phi_n}(\tau) = E[\phi_n(t)\phi_n(t + \tau)], \quad (\text{A.2})$$

where $E[\cdot]$ denotes the expectation value. The power spectral density of the phase noise according to Wiener–Khinchin theorem is the Fourier transform of its autocorrelation function

$$S_{\phi_n}(f) = \int_{-\infty}^{+\infty} d\tau R_{\phi_n}(\tau) e^{-j2\pi f\tau}. \quad (\text{A.3})$$

The PSD of phase noise has units of Rad^2/Hz . In the literature, usually what is referred to as phase noise is the power spectral density of the phase noise.

Although describing the phase noise using equations (A.1) to (A.3) is mathematically straightforward, extracting the phase noise information from a periodic signal requires additional effort. In addition, the effect of phase noise on the spectrum of

the signal $x(t)$ has to be well understood. Therefore, we investigate the effect of phase noise on the PSD of $x(t)$. The sinusoidal signal $x(t)$ in (A.1) can be expanded as

$$x(t) = x_0 \left[\cos(\phi_n(t)) \cos(\omega_0 t + \phi_0) - \sin(\phi_n(t)) \sin(\omega_0 t + \phi_0) \right]. \quad (\text{A.4})$$

If the phase noise variations are small, $|\phi_n(t)| \ll \pi/2$, Equation (A.4) can be further simplified to

$$x(t) \approx \underbrace{x_0 \cos(\omega_0 t + \phi_0)}_C - \underbrace{x_0 \phi_n(t) \sin(\omega_0 t + \phi_0)}_N. \quad (\text{A.5})$$

Equation (A.5) shows that phase noise is modulated by a sinusoidal term in quadrature to the carrier. Now we calculate the autocorrelation function and PSD of the carrier and noise terms of (A.5). The carrier term gives a autocorrelation function of

$$R_C(\tau) = \frac{1}{2} x_0^2 \cos(\omega_0 \tau), \quad (\text{A.6})$$

and a PSD of

$$S_C(f) = \frac{1}{4} x_0^2 [\delta(f - f_0) + \delta(f + f_0)], \quad (\text{A.7})$$

where $\delta(f)$ denotes the Dirac delta function and $f = \omega/2\pi$. The noise term gives an autocorrelation function of

$$R_N(\tau) = \frac{1}{2} x_0^2 \cos(\omega_0 \tau) R_{\phi_n}(\tau), \quad (\text{A.8})$$

and a PSD of

$$S_N(f) = \frac{1}{4} x_0^2 [S_{\phi_n}(f - f_0) + S_{\phi_n}(f + f_0)], \quad (\text{A.9})$$

Equations (A.8) and (A.9) are the mathematical basis for a popular method of phase noise measurement using spectrum analyzer. Phase noise can be found by measuring the power of the carrier sideband relative to the power of the carrier itself. This method is also illustrated graphically in Figure A.2.

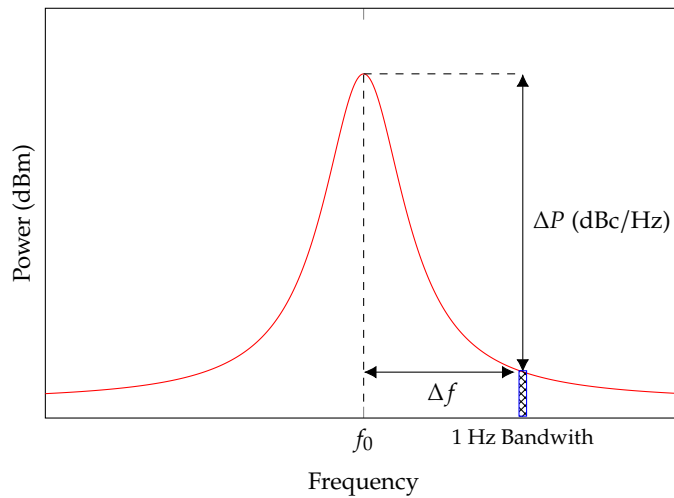


FIGURE A.2: Effect of phase noise on the signal spectrum.

A.2 Timing jitter

Another approach to model the random variations of the phase of a sinusoidal signal is to model the timing uncertainties rather than the phase uncertainties. One can simply rewrite (A.1) as

$$x(t) = x_0 \cos \left[\omega_0 \left(t + \frac{\phi_n(t)}{\omega_0} \right) + \phi_0 \right]. \quad (\text{A.10})$$

This rearrangement is the key to mathematically model the timing uncertainties of the sinusoidal signal. The jitter can consequently be defined as

$$\text{jitter} := \frac{\phi_n(t)}{\omega_0}. \quad (\text{A.11})$$

It is usually desired to find the total value of timing uncertainty over a range of offset frequencies. The rms-jitter can then be defined as the integral of PSD of the jitter over the desired offset-frequency range

$$\text{rms-jitter}(f_1, f_2) = \frac{1}{\omega_0^2} \int_{f_1}^{f_2} df S_{\phi_n}(f). \quad (\text{A.12})$$

A.3 Amplitude noise

Amplitude noise can be defined as the random fluctuations of a sinusoidal signal amplitude, illustrated graphically in Figure A.3. In a similar fashion the phase noise was included in a noiseless tone, amplitude noise of a sinusoidal signal can be modeled as

$$x(t) = x_0(1 + a_n(t)) \cos(\omega_0 t + \phi_0), \quad (\text{A.13})$$

where $a_n(t)$ is the amplitude noise. Similar to what has been done for the phase noise, the autocorrelation function and PSD of the amplitude noise can be derived

$$R_{a_n}(\tau) = E[a_n(t)a_n(t + \tau)], \quad (\text{A.14})$$

and

$$S_{a_n}(f) = \int_{-\infty}^{+\infty} d\tau R_{a_n}(\tau) e^{-j2\pi f\tau}. \quad (\text{A.15})$$

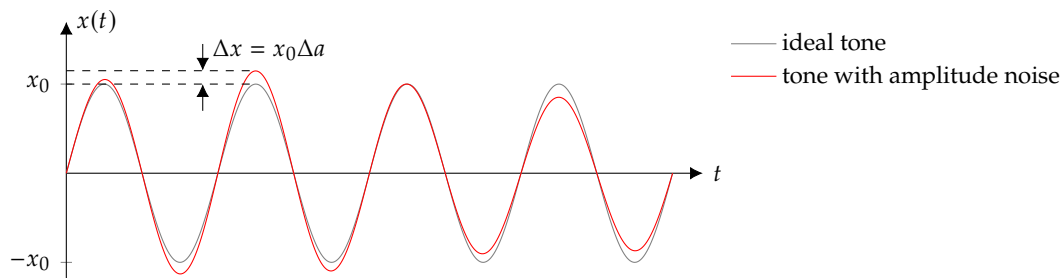


FIGURE A.3: Illustration of amplitude noise in a sinusoidal signal.

Appendix B

Fourier Transform

TABLE B.1: Fourier series; $x(t)$ is periodic with a period of T .

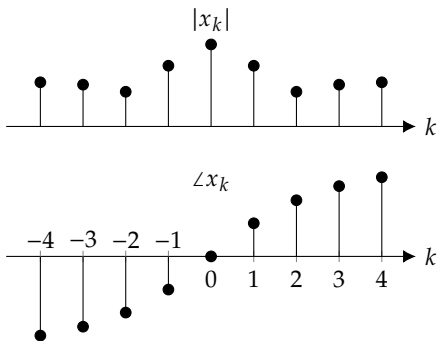
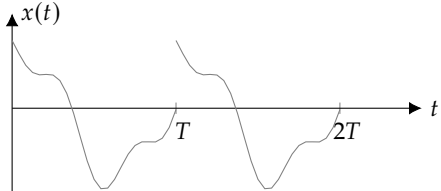
<p>Fourier series coefficients:</p> $x_k = \frac{1}{2\pi} \int_0^T dt x(t) e^{jk\omega_0 t} \quad (\text{B.1})$	
<p>Signal reconstruction:</p> $x(t) = \sum_{k=-\infty}^{+\infty} x_k e^{jk\omega_0 t} \quad (\text{B.2})$	

TABLE B.2: Fourier transform; $x(t)$ is absolutely integrable.

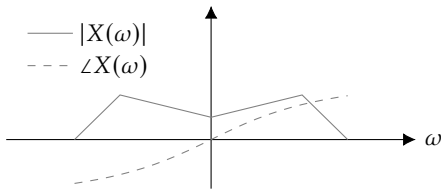
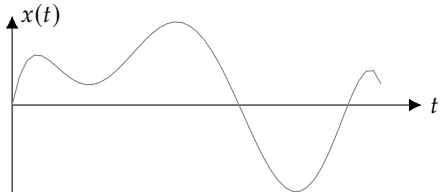
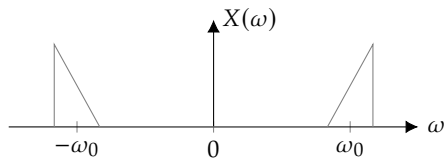
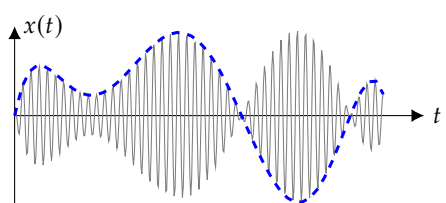
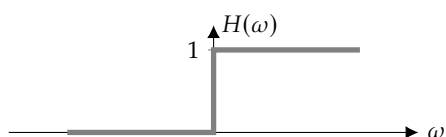
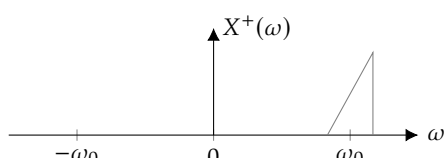
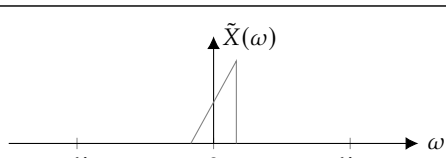
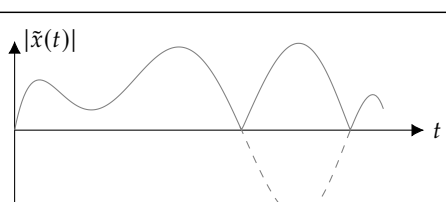
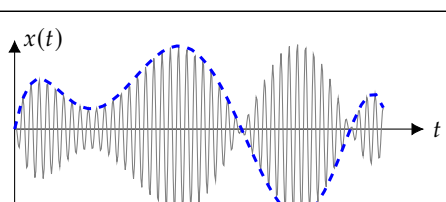
<p>Fourier transform:</p> $X(\omega) = \int_{-\infty}^{+\infty} dt x(t) e^{-j\omega t} \quad (\text{B.3})$	
<p>Inverse Fourier transform:</p> $x(t) = \frac{1}{2\pi} \int_{-\infty}^{+\infty} d\omega X(\omega) e^{j\omega t} \quad (\text{B.4})$	

TABLE B.3: Lowpass equivalent of bandpass signals.

<p>Bandpass signal Fourier transform:</p> $X(\omega) = \int_{-\infty}^{+\infty} dt x(t) e^{-j\omega t} \quad (\text{B.5})$	
<p>Bandpass signal inverse Fourier transform:</p> $x(t) = \frac{1}{2\pi} \int_{-\infty}^{+\infty} dt X(\omega) e^{j\omega t} \quad (\text{B.6})$	
<p>Heaviside step function:</p> $H(\omega) = \begin{cases} 0 & \text{for } \omega \leq 0 \\ 1 & \text{for } \omega > 0 \end{cases} \quad (\text{B.7})$	
<p>Fourier transform at positive frequencies:</p> $X^+(\omega) = H(\omega)X(\omega) \quad (\text{B.8})$	
<p>Lowpass equivalent of bandpass signal in frequency domain:</p> $\tilde{X}(\omega) = X^+(\omega + \omega_0) \quad (\text{B.9})$	
<p>Lowpass equivalent of bandpass signal in time domain:</p> $\tilde{x}(t) = \frac{1}{2\pi} \int_{-\infty}^{+\infty} dt \tilde{X}(\omega) e^{j\omega t} \quad (\text{B.10})$	
<p>Bandpass signal reconstruction from its lowpass equivalent:</p> $x(t) = \text{Re} \left\{ 2\tilde{x}(t) e^{j\omega_0 t} \right\} \quad (\text{B.11})$	

Appendix C

Characteristic function of balanced intensity modulator

As we mentioned earlier, the BIM can be implemented using a Sagnac loop or an MZM, as they both have similar transfer characteristics. We therefore choose a balanced MZM block diagram, illustrated in Figure C.1, for our analysis. Assuming the photo detectors in Figure 3.4(a) are linear, we can directly use the output intensities of the MZM and exclude the photodiode responsivity from our equations. The input optical field, x , is divided into two parts and these parts enter the upper and the lower arms of the modulator. Each part passes through two tunable phase shifters which are controlled by two separate electrodes, RF and dc. The upper and the lower phase shifters add positive and negative phase shifts to the optical signals, respectively. The phase shifted signals are then recombined using a 90-degree 2×2 coupler which obeys the following relations in the phasor domain

$$y^+ = \frac{b^+ + \mathbf{j}b^-}{\sqrt{2}} \quad \text{and} \quad y^- = \frac{b^- + \mathbf{j}b^+}{\sqrt{2}}, \quad (\text{C.1})$$

where y^+ and y^- are the output signals of the coupler, b^+ and b^- are the input signals of the coupler and \mathbf{j} is the unit imaginary number $\sqrt{-1}$.

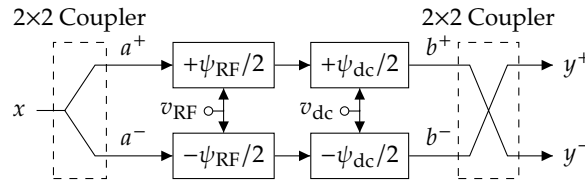


FIGURE C.1: Block diagram of Mach-Zehnder modulator with two separate electrodes for RF modulation and dc bias.

The output signals of the 1×2 coupler, a^+ and a^- , are both equal to $x/\sqrt{2}$. The outputs of the upper and lower phase shifters are then

$$b^\pm = \frac{x}{\sqrt{2}} e^{\pm \mathbf{j}\psi/2}, \quad (\text{C.2})$$

where the phase ψ follows (3.25). Combining (C.1) and (C.2), the outputs of the modulator can be written as

$$y^\pm = \frac{x}{2} [e^{\pm \mathbf{j}\psi/2} - \mathbf{j}e^{\mp \mathbf{j}\psi/2}]. \quad (\text{C.3})$$

The intensities of the optical outputs can consequently be derived as

$$I_y^\pm = I_x [0.5 \pm 0.5 \sin(\psi)] , \quad (\text{C.4})$$

where I_y^+ is the intensity of y^+ , I_y^- is the intensity of y^- and I_x is the intensity of the optical input field x .

Appendix D

Transfer Characteristic of the Bias Electrode Noise

The noise of the dc voltage applied to the dc electrode of the modulator is included in (4.31) and the modulator output considering this noise voltage is given by (4.33). The noise term in (4.33) is

$$i_{n,bias}(t) = R_\lambda [\psi_n(t)I(t) \cos(\psi_{RF}(t) + \psi_{dc})] * h(t) , \quad (D.1)$$

where $i_{n,bias}$ denotes the noise term of the output current of the BOMPD. The term in brackets shows that $\psi_n(t)$ is modulated by the modulation term (MT)

$$MT = I(t) \cos(\psi_{RF}(t) + \psi_{dc}) , \quad (D.2)$$

which has many tones. For the phase detector application, only the dc term of MT is important and the higher order harmonics are filtered by the loop filter. This dc term can be written as

$$\langle MT \rangle = \left\langle I_0 T_{ref} \sum_{m=-\infty}^{+\infty} \delta(t - \frac{m}{f_{ref}}) \cos(\psi_{RF}(t) + \psi_{dc}) \right\rangle , \quad (D.3)$$

where we used (3.26) and approximated the optical pulse shape as Dirac delta function. Assuming a single tone excitation of the RF electrode with (3.29) and applying the harmonic locking condition $\omega_{RF} = N\omega_{ref}$, the optical pulse samples the RF signal at the same phase in every cycle of the RF signal. Therefore, the average of the modulation term can be found by averaging over the first cycle of optical pulse as

$$\langle MT \rangle = I_0 \cos(\psi_0) , \quad (D.4)$$

where ψ_0 is given in (3.38). Therefore with approximation of neglecting the high frequency terms of (D.1), the output noise of the BOMPD can be written as

$$i_{n,bias}(t) \approx R_\lambda I_0 \cos(\psi_0) \psi_n(t) * h(t) . \quad (D.5)$$

Finally, taking into account the locking condition $\psi_0 = 0$ and assuming the photodiode bandwidth is much higher than the bandwidth of the voltage noise applied to the dc electrode, $h(t)$ can be approximated as Dirac delta function and (D.5) can be further simplified to (4.36).

Appendix E

Gain of BOMPD with Nonlinear Photodiode

The phase detector characteristic function is given by (3.31) and the phase detector gain is the slope of the characteristic function at the zero crossing

$$\begin{aligned} K_\phi &= \frac{d}{d\phi} \langle i_{PD}^+ - i_{PD}^- \rangle \Big|_{\psi_0=0} \\ &= \frac{d}{d\phi} \langle i_{PD}^+ \rangle \Big|_{\psi_0=0} - \frac{d}{d\phi} \langle i_{PD}^- \rangle \Big|_{\psi_0=0}. \end{aligned} \quad (E.1)$$

where $\langle i_{PD}^\pm \rangle$ is given by (4.42). Now we find the derivative of $\langle i_{PD}^\pm \rangle$ with respect to ϕ

$$\frac{d}{d\phi} \langle i_{PD}^\pm \rangle = \frac{d}{d\phi} \left[\frac{R_{\lambda 0} I_0 [1 \pm \sin(\psi_0)]}{2 + I_0 T_R [1 \pm \sin(\psi_0)] / E_{sat}} \right], \quad (E.2)$$

where we substituted (4.39) and (4.40) into (4.42). The derivative of $\langle i_{PD}^\pm \rangle$ with respect to ϕ can be found using the chain rule and (3.38) as

$$\begin{aligned} \frac{d}{d\phi} \langle i_{PD}^\pm \rangle &= \frac{d\psi_0}{d\phi} \frac{d}{d\psi_0} \left[\frac{R_{\lambda 0} I_0 [1 \pm \sin(\psi_0)]}{2 + I_0 T_R [1 \pm \sin(\psi_0)] / E_{sat}} \right] \\ &= \frac{\pm 2\alpha \cos(\phi) \cos(\psi_0) R_{\lambda 0} I_0 [1 \pm \sin(\psi_0)]}{(2 + I_0 T_R [1 \pm \sin(\psi_0)] / E_{sat})^2}. \end{aligned} \quad (E.3)$$

Imposing the zero-crossing condition, $\psi_0 = 0$, on (E.3) gives

$$\frac{d}{d\phi} \langle i_{PD}^\pm \rangle \Big|_{\psi_0=0} = \frac{\pm R_{\lambda 0} I_0 \sqrt{\alpha^2 - \psi_{dc}^2}}{2(1 + I_0 T_R / 2E_{sat})^2}. \quad (E.4)$$

Substituting (E.4) in (E.1) gives the phase detector gain in (4.43).

Appendix F

Phase Noise Measurement Techniques

F.1 Baseband PSD measurement using cross correlation

One challenge in characterization of an ultra low phase noise signal is the measurement of phase noise itself. How can one measure the PSD of a signal that is smaller than the instrument noise floor by orders of magnitude? The answer is to use 2 pieces of hardware in parallel and extract the correlated part of the measured signals. In order to illustrate this technique, we use the simplified diagram shown in Figure F.1. The mathematical formalism in this section only deals with PSD measurement of a baseband signal and we assume the phase noise of the carrier signal is extracted using the delay line method or the phase-locked loop method explained in Section F.2.

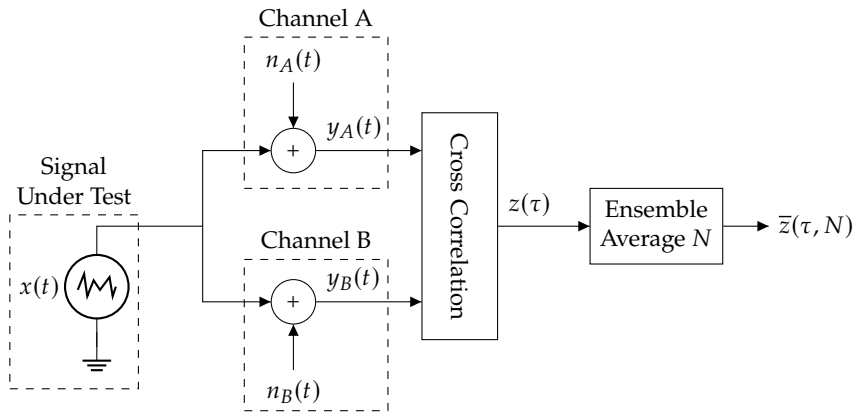


FIGURE F.1: Schematic of PSD measurement setup using cross correlation technique.

Note that we are interested in the average autocorrelation or the average Fourier transform of $x(t)$. The output signals of Channel A and Channel B can be written as

$$y_A(t) = x(t) + n_A(t) , \quad (\text{F.1})$$

$$y_B(t) = x(t) + n_B(t) , \quad (\text{F.2})$$

where $x(t)$ is the signal under test (SUT), $n_A(t)$ & $n_B(t)$ are the equivalent input noise of Channel A & B, respectively, and $y_A(t)$ & $y_B(t)$ are the outputs of Channel A & B, respectively. Applying sample cross correlation between x_A and x_B yields $z(\tau)$

$$z(\tau) = r_{y_{A,B}}(\tau) = r_x(\tau) + r_{n_A,x}(\tau) + r_{x,n_B}(\tau) + r_{n_A,n_B}(\tau) , \quad (\text{F.3})$$

with a Fourier transform of

$$Z(f) = |X(f)|^2 + N_A(f)X^*(f) + X(f)N_B^*(f) + N_A(f)N_B^*(f). \quad (\text{F.4})$$

The basic idea of cross correlation technique is to suppress the statistically independent noise terms by averaging. The more the number of averages, the more the noise terms are suppressed. This can indeed be seen in the formula (F.3). The expectation value of $r_{y_{A,B}}(\tau)$ is composed of four terms; only the first term is nonzero and all other terms are zero due to the statistical independence of $x(t)$ & $n_A(t)$, $x(t)$ & $n_B(t)$ and $n_A(t)$ & $n_B(t)$. However, expectation value means averaging over infinite sample signals which is not practically possible. Therefore, we need to find out how much suppression of the undesired noise terms is achieved as a function of number of averages. In practice, only a two-channel hardware is used and the signals are truncated over a certain period of time, then the cross correlation is performed and the cross-correlated signals are averaged. In this analysis, for simplicity, we assume that N pieces of two-channels hardware are available and ensemble averaging without signal truncation is possible.

The output of the averaging block can therefore be written as

$$\begin{aligned} \bar{z}(\tau, N) = & \frac{1}{N} \sum_{k=1}^N \{r_x(\tau)\}_k + \frac{1}{N} \sum_{k=1}^N \{r_{x,n_B}(\tau)\}_k \\ & + \frac{1}{N} \sum_{k=1}^N \{r_{n_A,x}(\tau)\}_k + \frac{1}{N} \sum_{k=1}^N \{r_{n_A,n_B}(\tau)\}_k, \end{aligned} \quad (\text{F.5})$$

with a Fourier transform of

$$\begin{aligned} \bar{Z}(f, N) = & \frac{1}{N} \sum_{k=1}^N \{|X(f)|^2\}_k + \frac{1}{N} \sum_{k=1}^N \{N_A(f)X^*(f)\}_k \\ & + \frac{1}{N} \sum_{k=1}^N \{X(f)N_B^*(f)\}_k + \frac{1}{N} \sum_{k=1}^N \{N_A(f)N_B^*(f)\}_k, \end{aligned} \quad (\text{F.6})$$

where the index k refers to the sample number in the ensemble. Now we find the mean and variance of $\bar{Z}(f, N)$. Only the first term in the right hand of (F.6) has a non-zero average and all other terms are composed of statistically independent random processes

$$\mathbb{E}[\bar{Z}(f, N)] = \mathbb{E}[|X(f)|^2] = S_x(f). \quad (\text{F.7})$$

Therefore, the average output of the cross correlator is equal to the PSD of the signal under test. Now we look at the variance of the real and imaginary parts of $\bar{Z}(f, N)$. We start by finding the variance of the real part of the second term on the right hand of (F.6). In order to do that, first we write the real part as

$$\text{Re}\{N_A(f)X^*(f)\} = N_{A,R}(f)X_R(f) + N_{A,I}(f)X_I(f), \quad (\text{F.8})$$

where the lower R and I indices denote the real part and imaginary part, respectively. Now the variance of (F.8) is

$$\begin{aligned} \mathbb{E} \left[\text{Re}^2 \{ N_A(f) X^*(f) \} \right] &= \frac{1}{2} S_{n_A}(f) \mathbb{E} [X_R^2(f)] + \frac{1}{2} S_{n_A}(f) \mathbb{E} [X_I^2(f)] \\ &= \frac{1}{2} S_{n_A}(f) S_x(f) , \end{aligned} \quad (\text{F.9})$$

where we assumed the real and imaginary parts of the noise process n_A are statistically independent. Averaging over an ensemble of N samples reduces this variance by a factor of N

$$\mathbb{E} \left[\text{Re}^2 \left\{ \frac{1}{N} \sum_{k=1}^N \{ N_A(f) X^*(f) \}_k \right\} \right] = \frac{1}{2N} S_{n_A}(f) S_x(f) . \quad (\text{F.10})$$

The variance of other terms in (F.6) can be found in a similar fashion. The final result for both the real part and the imaginary part is

$$\sigma_z^2(f, N) = \frac{1}{2N} [S_{n_A}(f) S_x(f) + S_{n_B}(f) S_x(f) + S_{n_A}(f) S_{n_B}(f)] , \quad (\text{F.11})$$

where $\sigma_z^2(f, N)$ denotes the variance of $\bar{Z}(f, N)$. Note that $Z(f)$ has already the units of power spectral density. Therefore, with respect to the desired signal power spectral density, $S_x(f)$, the noise variance is proportional to $\sigma_z(f)$. As a result, for the measurement of $S_x(f)$, the noise variance is the standard deviation of $\bar{Z}(f, N)$. The noise reduction factor can be defined relative to a single measurement without any averaging as

$$\text{NRF} = \frac{\sigma_z(f, 1)}{\sigma_z(f, N)} = \sqrt{N} , \quad (\text{F.12})$$

and in decibels as

$$\text{NRF}_{\text{dB}} = 10 \log_{10}(\text{NRF}) = 5 \log_{10}(N) . \quad (\text{F.13})$$

F.2 Single-channel phase noise measurement

In the previous section we showed how the noise floor of a baseband receiver can be suppressed using two channel cross correlation technique. Note that this technique can only be used for the measurement of PSD and statistical signal analysis, not instantaneous measurement of a signal. For phase noise analysis, the SUT has a bandpass nature and cannot directly be applied to a baseband receiver. Therefore, the phase noise of the SUT has to be first extracted and then applied to a two-channel baseband receiver. The phase noise can be discriminated using a phase detector, usually a double balanced mixer, whose input signals are in quadrature, shown in Figure F.2. For a complete two-channel phase noise analyzer, two pieces of the phase noise measurement apparatus are necessary. The output signals of these single-channel phase noise analyzers are then applied to a cross correlator to suppress the undesired noise signals by correlation and averaging.

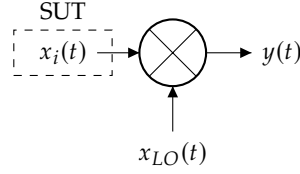


FIGURE F.2: Phase detection using double balanced mixer.

The phase detector input, $x_i(t)$, is a single tone with an angular frequency of ω_0 and an amplitude of A_i

$$x_i(t) = A_i \sin(\omega_0 t + \phi_{n,i}(t)) , \quad (\text{F.14})$$

where $\phi_{n,i}(t)$ the phase noise of the SUT. Assuming the local oscillator (LO) signal is in quadrature with the SUT, it can be written similarly as

$$x_{LO}(t) = A_{LO} \cos(\omega_0 t + \phi_{n,LO}(t)) . \quad (\text{F.15})$$

Balanced mixers are switching devices and operate in saturation regime with respect to their switching input. Hence, we assume the LO signal is close to saturation levels of the mixer and the mixer has a constant gain independent of the level of the LO signal. Assuming the mixing process has a gain of $2L$ (a gain of $2L$ corresponds to a gain of L for each output mixing term) its output $y(t)$ can be written as

$$\begin{aligned} y(t) &= 2LA_i \sin(\omega_0 t + \phi_{n,i}(t)) \cos(\omega_0 t + \phi_{n,LO}(t)) \\ &= LA_i \sin(\phi_{n,i}(t) - \phi_{n,LO}(t)) + LA_i \sin(2\omega_0 t + \phi_{n,i}(t) + \phi_{n,LO}(t)) . \end{aligned} \quad (\text{F.16})$$

The second term on the right-hand side of (F.16) has a high frequency and can be filtered. Assuming the variation of phase noise is small, $|\phi_{n,i}(t)|, |\phi_{n,LO}(t)| \ll \pi/2$, the phase detector output can be written as

$$y(t) \approx LA_i [\phi_{n,i}(t) - \phi_{n,LO}(t)] . \quad (\text{F.17})$$

The noise of the LO signal can then be suppressed by using a cross-correlation scheme, leading to extraction of the phase noise of SUT.

We have seen that phase detection using a balanced frequency mixer requires quadrature operation. The quadrature signal for LO is usually generated using two methods, delay line method and PLL method, which are explained in the following.

Delay line frequency discriminator In the delay line method, the quadrature LO signal is a delayed version of the SUT, as illustrated in Figure F.3.

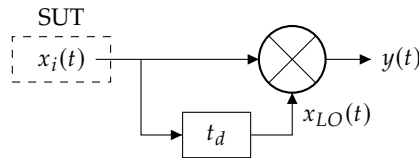


FIGURE F.3: Phase noise measurement using delay line frequency discrimination technique.

The LO signal, $x_{LO}(t)$, can be written as

$$x_{LO}(t) = x_i(t - t_d) = A_i \sin(\omega_0 t - \omega_0 t_d + \phi_{n,i}(t - t_d)) , \quad (\text{F.18})$$

where t_d is the delay time and is chosen such that

$$\omega_0 t_d = (k - \frac{1}{2})\pi, \quad (\text{F.19})$$

for a positive integer k . With this assumption, the quadrature operation of the balanced mixer is guaranteed and the phase detector output can be written as

$$y(t) = \pm LA_i [\phi_{n,i}(t) - \phi_{n,i}(t - t_d)] . \quad (\text{F.20})$$

The balanced mixer output is proportional to the difference between the phase noise and a delayed version of itself. This behavior is similar to a derivative operator and since the derivative of the phase is the frequency, this technique discriminates the frequency noise, rather than the phase noise itself. The phase noise can then be calculated by integration of the frequency noise. The impulse response $h_{\text{FD}}(t)$ and its Fourier transform $H_{\text{FD}}(\omega)$ of the frequency discriminator are

$$h_{\text{FD}}(t) = \pm LA_i [\delta(t) - \delta(t - t_d)] \quad \text{and} \quad H_{\text{FD}}(\omega) = \pm j LA_i \sin\left(\frac{\omega t_d}{2}\right) e^{-j\frac{\omega t_d}{2}} . \quad (\text{F.21})$$

The sine terms in the transfer function of delay line frequency discriminator leads to nulls at offset frequencies of $\omega = 2k\pi/t_d$. These nulls lead to limiting the maximum offset frequency range of this technique. For the measurement of phase noise at offset frequencies below the first null, $\omega \ll 2\pi/t_d$, the phase detector output can be approximated as

$$y(t) = \pm LA_i t_d \frac{d}{dt} \phi_{n,i}(t) . \quad (\text{F.22})$$

The derivation of phase noise leads to degradation of sensitivity at low offset frequencies. In addition, (F.22) shows the gain of this technique is proportional to the delay time. This technique is especially useful for measurement of relatively noisy signals with a high drift, such as the output of an open loop VCO. High drift of a signal prevents using more precise, however slower, methods such as phase detection using PLL technique.

Phase detection using PLL technique A phase detector is an inseparable block of any phase-locked loop. If a balanced mixer is used for phase detection in a PLL with an integrator as the loop filter, the dynamics of the loop causes a zero-average signal at the phase detector output (for further details see Section 3.1), which is equivalent to the quadrature operation in a balanced mixer. Figure F.4 shows the block diagram of this technique.

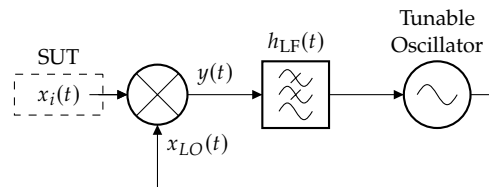


FIGURE F.4: Phase noise measurement using PLL technique.

Using the mathematical model provided in Section 3.1, the open loop transfer function similar to (3.5) can be written as

$$H_{OL}(s) = K_\phi H_{LF}(s) \frac{K_V}{s} , \quad (F.23)$$

where K_V is the tuning sensitivity of the tunable oscillator, $H_{LF}(s)$ is the transfer function of the loop filter and K_ϕ is the phase detector gain. For a balanced mixer we showed that $K_\phi = LA_i$. The transfer function of the phase detector output to the input phase can be expressed in terms of $H_{OL}(s)$ as

$$\frac{Y}{\Phi_{n,i}}(s) = \frac{K_\phi}{1 + H_{OL}(s)} . \quad (F.24)$$

This transfer function is similar to (3.12) and has a highpass behavior. This is indeed expected of any phase noise measurement system, since the LO signal of the system needs to track the signal under test. This means the LO signal has the same average phase as the SUT but with a 90-degree phase shift. The rate of tracking is also equivalent to the cut-off frequency of the transfer function given in (F.24). The noise of the tunable oscillator is also transferred to $y(t)$ with the same transfer function given in (F.24). Therefore, For phase noise measurement at offset frequencies sufficiently above the loop cut-off frequency, $|H_{OL}(\omega)| \ll 1$, the phase detector output can be approximated as

$$y(t) \approx LA_i [\phi_{n,i}(t) - \phi_{n,TO}(t)] , \quad (F.25)$$

where $\phi_{n,TO}(t)$ is the phase noise of the tunable oscillator and we replaced the phase detector gain with its equivalent value in balanced mixer.

F.3 Two-channel phase noise measurement

So far we have seen how to measure the PSD of a baseband signal that is below the noise the noise floor of a measurement system using two-channel cross correlation technique and also we demonstrated how to extract the phase noise of a carrier using delay line or PLL technique. We have now the necessary tools to demonstrate a two-channel phase noise measurement system. This system is composed of two single-channel phase noise analyzers and a two-channel cross correlator. Figure F.5 shows the block diagram of this system. If both channels are perfectly isolated, their additive phase noise are uncorrelated and can be suppressed by cross correlation and averaging according to (F.13). This method is gold-standard for phase noise measurement and is implemented in laboratory-grade phase noise test systems.

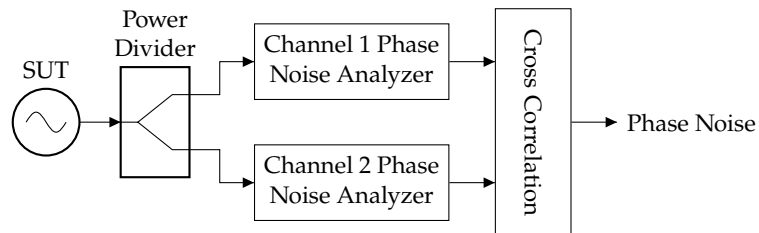


FIGURE F.5: Two-channel phase noise measurement system.

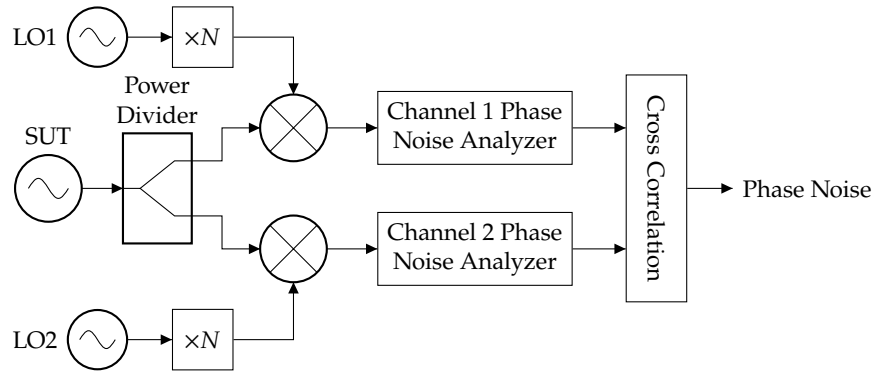
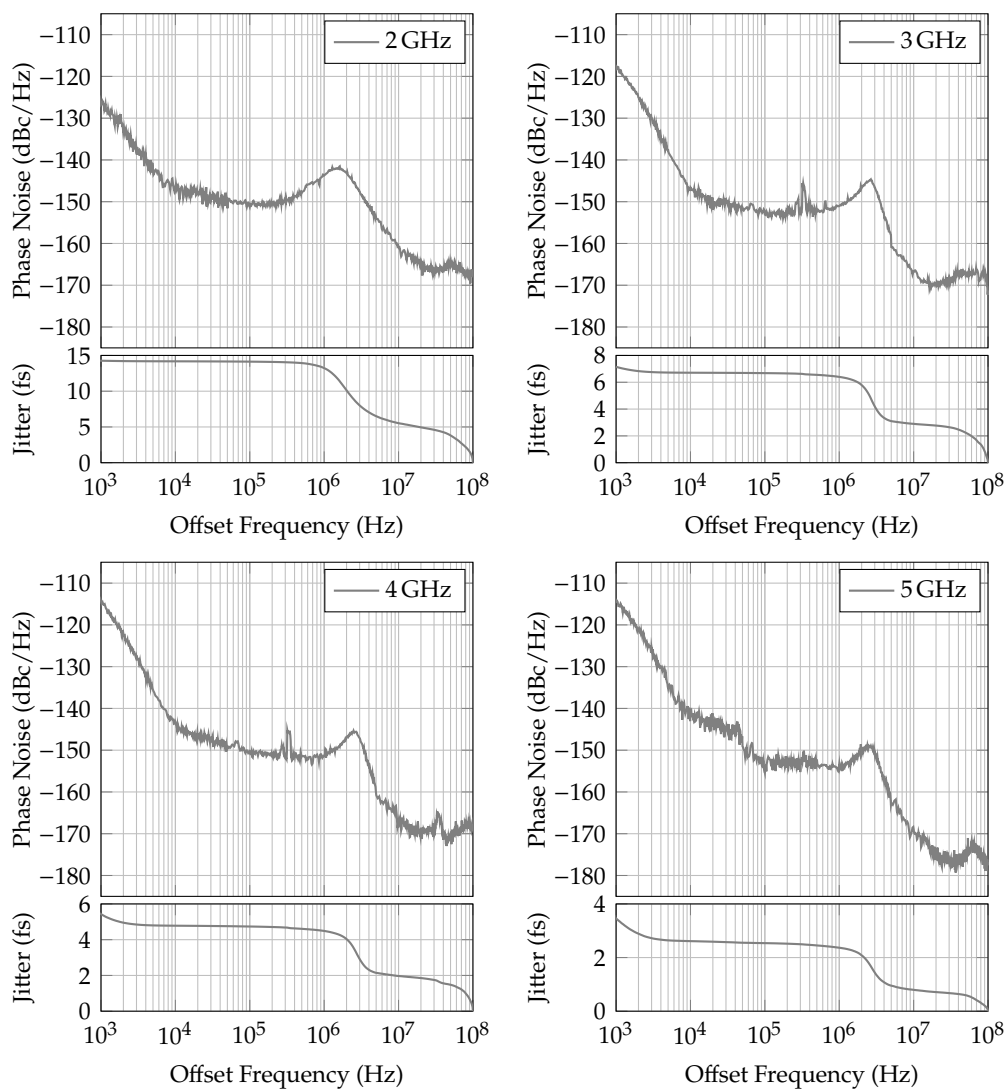


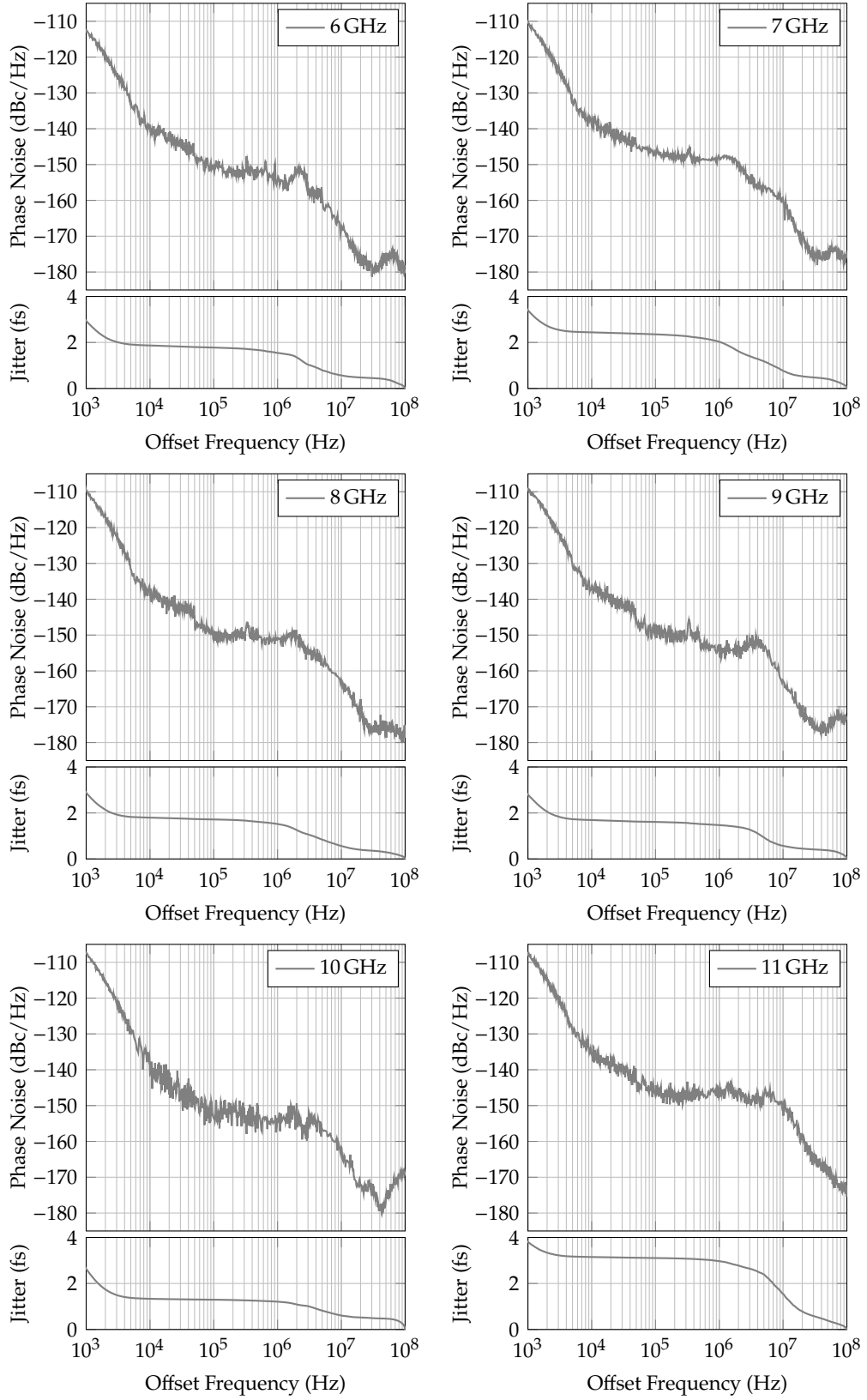
FIGURE F.6: Two-channel phase noise measurement of mmWave and terahertz signals.

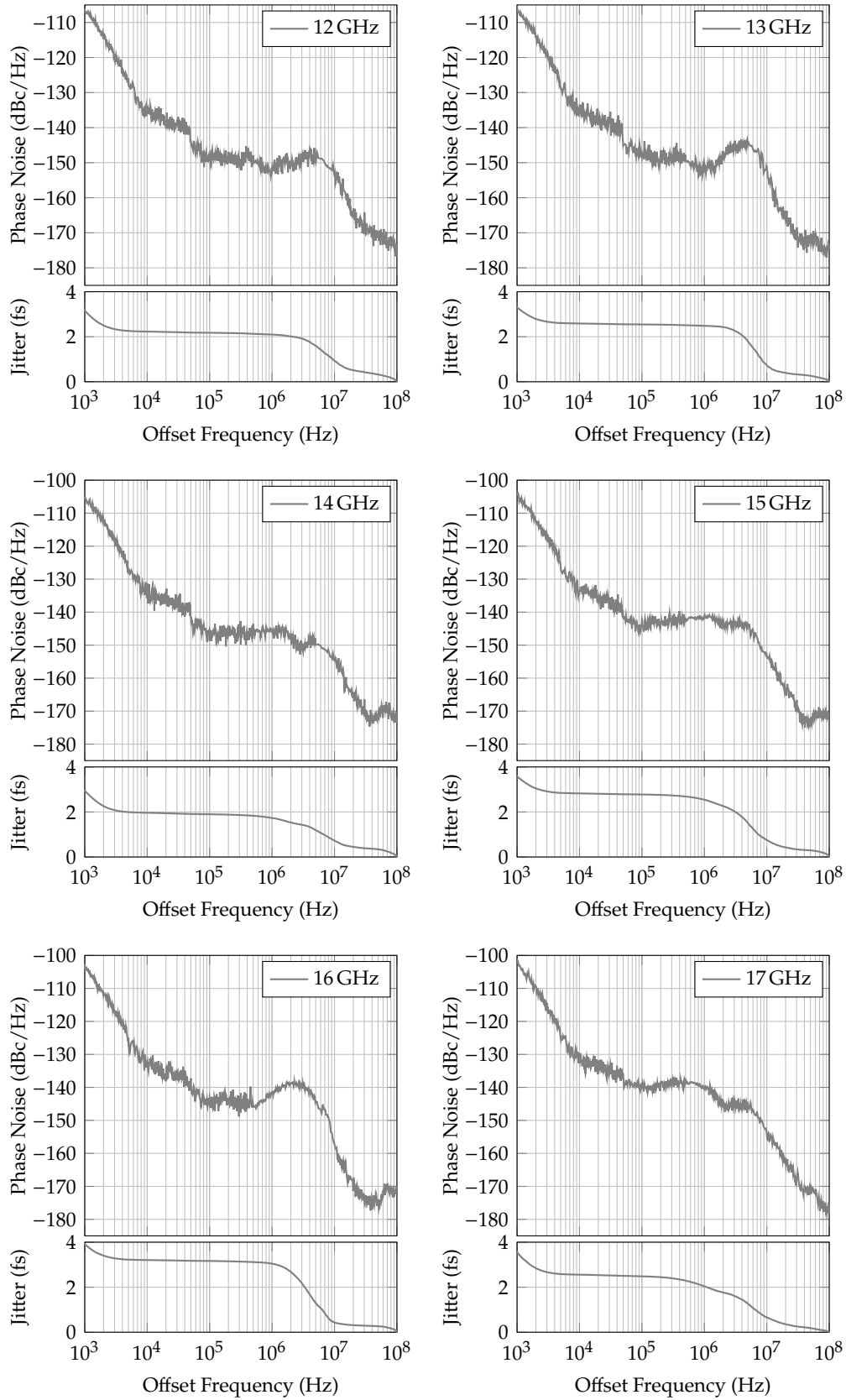
The frequency range of the two-channel test system can reach up to tens of gigahertz, due to technical limitation of RF components. Further enhancement of frequency range up to millimeter-wave and terahertz frequencies is possible using the two-channel down-conversion scheme illustrated in Figure F.6. The high frequency signal is first down-converted to a frequency that lies in the frequency range of each phase noise measurement channel. The phase noise of the down-converted signals is then extracted by each channel and their correlated part, which is the phase noise of SUT, is extracted. The LOs and the mixers also contribute to the phase noise measured by each channel. Therefore, it is necessary that the two LOs be uncorrelated so their phase noise can be suppressed by cross correlation.

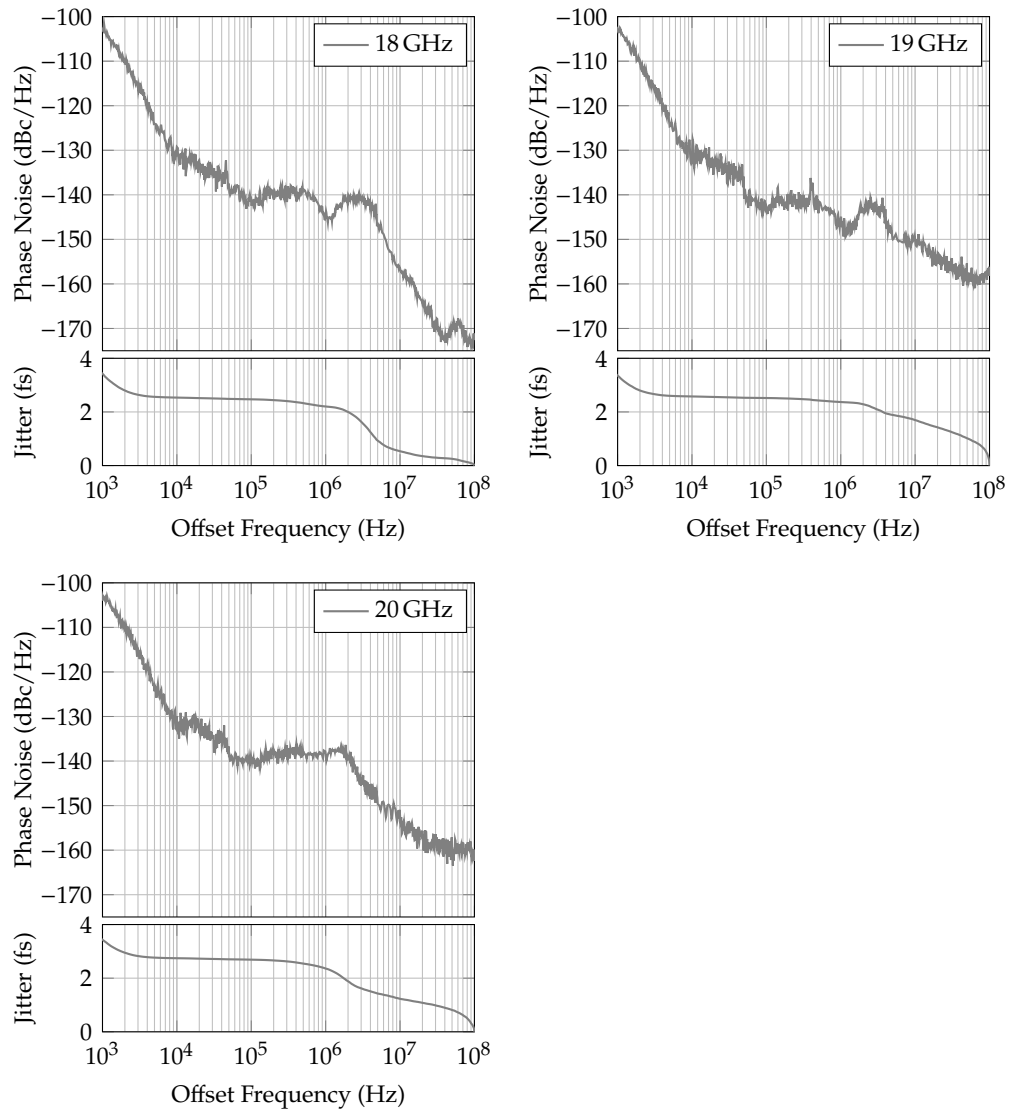
Appendix G

Phase Noise and Jitter of OEPLL with YIG Oscillator









Bibliography

- [1] J. Kim and F. X. Kaertner, "Attosecond-precision ultrafast photonics," *Laser & Photonics Reviews*, vol. 4, no. 3, pp. 432–456, 2010.
- [2] "High Performance (VC)OCXO," KVG Quartz Crystal Technology GmbH, Neckarbischofsheim, Germany, Datasheet O-40CXXXX-LPN-LGS-LF, Nov. 2017.
- [3] "Ultra Low Phase Noise Oven Controlled Crystal Oscillator," Mount Holly Springs, PA, USA, Datasheet OX-305, Nov. 2016.
- [4] "Voltage Controlled SAW Oscillator Surface Mount Model," Synergy Microwave, Paterson, NJ, USA, Datasheet HFSO1000-5, Mar. 2017, Rev. B.
- [5] "The Sapphire Loaded Cavity Oscillator (SLCO)," Poseidon Scientific Instruments, Fremantle WA, Australia, Datasheet SLCO, May 2004, Rev. 05/04.
- [6] J. W. Zobel, M. Giunta, A. J. Goers, R. L. Schmid, J. Reeves, R. Holzwarth, E. J. Adles, and M. L. Dennis, "Comparison of optical frequency comb and sapphire loaded cavity microwave oscillators," *IEEE Photonics Technology Letters*, pp. 1–1, 2019. DOI: [10.1109/lpt.2019.2926190](https://doi.org/10.1109/lpt.2019.2926190).
- [7] L. Maleki, "Optoelectronic oscillators for microwave and mm-wave generation," in *2017 18th International Radar Symposium (IRS)*, IEEE, Jun. 2017. DOI: [10.23919/irs.2017.8008133](https://doi.org/10.23919/irs.2017.8008133).
- [8] A. B. Matsko, D. Eliyahu, and L. Maleki, "Theory of coupled optoelectronic microwave oscillator II: Phase noise," *Journal of the Optical Society of America B*, vol. 30, no. 12, p. 3316, Nov. 2013. DOI: [10.1364/josab.30.003316](https://doi.org/10.1364/josab.30.003316).
- [9] A. Ly, V. Aurox, R. Khayatzaheh, N. Gutierrez, A. Fernandez, and O. Llopis, "Highly spectrally pure 90-GHz signal synthesis using a coupled optoelectronic oscillator," *IEEE Photonics Technology Letters*, vol. 30, no. 14, pp. 1313–1316, Jul. 2018. DOI: [10.1109/lpt.2018.2845747](https://doi.org/10.1109/lpt.2018.2845747).
- [10] T. K. Kim, Y. Song, K. Jung, C. Kim, H. Kim, C. H. Nam, and J. Kim, "Sub-100-as timing jitter optical pulse trains from mode-locked Er-fiber lasers," *Optics Letters*, vol. 36, no. 22, p. 4443, Nov. 2011. DOI: [10.1364/ol.36.004443](https://doi.org/10.1364/ol.36.004443).
- [11] "Ultra low timing jitter performance & characterization of Origami femtosecond laser series," Onefive, Berlin, Germany, Whitepaper P/N 09-001, Jun. 2009, Rev. 1.1.
- [12] "Menhir Photonics femtosecond laser source," Menhir Photonics AG, Rümlang, Switzerland, Datasheet MENHIR-1550, Jun. 2019.
- [13] X. Xie, R. Bouchand, D. Nicolodi, M. Giunta, W. Hänsel, M. Lezius, A. Joshi, S. Datta, C. Alexandre, M. Lours, P.-A. Tremblin, G. Santarelli, R. Holzwarth, and Y. L. Coq, "Photonic microwave signals with zeptosecond-level absolute timing noise," *Nature Photonics*, vol. 11, no. 1, pp. 44–47, Nov. 2016. DOI: [10.1038/nphoton.2016.215](https://doi.org/10.1038/nphoton.2016.215).
- [14] M. Kalubovilage, M. Endo, and T. R. Schibli, "Ultra-low phase noise microwave generation with a free-running monolithic femtosecond laser," *Optics Express*, vol. 28, no. 17, p. 25 400, Aug. 2020. DOI: [10.1364/oe.399425](https://doi.org/10.1364/oe.399425).

- [15] S. Krakauer, "Harmonic generation, rectification, and lifetime evaluation with the step recovery diode," *Proceedings of the IRE*, vol. 50, no. 7, pp. 1665–1676, Jul. 1962. doi: [10.1109/jrproc.1962.288155](https://doi.org/10.1109/jrproc.1962.288155).
- [16] E. Afshari and A. Hajimiri, "Nonlinear transmission lines for pulse shaping in silicon," *IEEE Journal of Solid-State Circuits*, vol. 40, no. 3, pp. 744–752, Mar. 2005. doi: [10.1109/jssc.2005.843639](https://doi.org/10.1109/jssc.2005.843639).
- [17] T. D. Shoji, W. Xie, K. L. Silverman, A. Feldman, T. Harvey, R. P. Mirin, and T. R. Schibli, "Ultra-low-noise monolithic mode-locked solid-state laser," *Optica*, vol. 3, no. 9, p. 995, Sep. 2016. doi: [10.1364/optica.3.000995](https://doi.org/10.1364/optica.3.000995).
- [18] M. Bahmanian and J. C. Scheytt, "A 2–20-GHz ultralow phase noise signal source using a microwave oscillator locked to a mode-locked laser," *IEEE Transactions on Microwave Theory and Techniques*, vol. 69, no. 3, pp. 1635–1645, 2021. doi: [10.1109/TMTT.2020.3047647](https://doi.org/10.1109/TMTT.2020.3047647).
- [19] B. Razavi, *RF Microelectronics*. London, U.K.: Pearson Education, Sep. 22, 2011, 960 pp., ISBN: 0137134738.
- [20] J. Millo, R. Boudot, M. Lours, P. Y. Bourgeois, A. N. Luiten, Y. L. Coq, Y. Kersalé, and G. Santarelli, "Ultra-low-noise microwave extraction from fiber-based optical frequency comb," *Optics Letters*, vol. 34, no. 23, p. 3707, Nov. 2009. doi: [10.1364/ol.34.003707](https://doi.org/10.1364/ol.34.003707).
- [21] T. M. Fortier, M. S. Kirchner, F. Quinlan, J. Taylor, J. C. Bergquist, T. Rosenband, N. Lemke, A. Ludlow, Y. Jiang, C. W. Oates, and S. A. Diddams, "Generation of ultrastable microwaves via optical frequency division," *Nature Photonics*, vol. 5, no. 7, pp. 425–429, Jun. 2011. doi: [10.1038/nphoton.2011.121](https://doi.org/10.1038/nphoton.2011.121).
- [22] F. Quinlan, T. M. Fortier, M. S. Kirchner, J. A. Taylor, M. J. Thorpe, N. Lemke, A. D. Ludlow, Y. Jiang, and S. A. Diddams, "Ultralow phase noise microwave generation with an Er: fiber-based optical frequency divider," *Optics Letters*, vol. 36, no. 16, p. 3260, Aug. 2011. doi: [10.1364/ol.36.003260](https://doi.org/10.1364/ol.36.003260).
- [23] W. Zhang, S. Seidelin, A. Joshi, S. Datta, G. Santarelli, and Y. L. Coq, "Dual photo-detector system for low phase noise microwave generation with femtosecond lasers," *Optics Letters*, vol. 39, no. 5, p. 1204, Feb. 2014. doi: [10.1364/ol.39.001204](https://doi.org/10.1364/ol.39.001204).
- [24] J. Kim, F. X. Kärtner, and F. Ludwig, "Balanced optical-microwave phase detectors for optoelectronic phase-locked loops," *Optics Letters*, vol. 31, no. 24, p. 3659, Nov. 2006. doi: [10.1364/ol.31.003659](https://doi.org/10.1364/ol.31.003659).
- [25] M. Y. Peng, A. Kalaydzhyan, and F. X. Kärtner, "Balanced optical-microwave phase detector for sub-femtosecond optical-RF synchronization," *Optics Express*, vol. 22, no. 22, p. 27 102, Oct. 2014. doi: [10.1364/oe.22.027102](https://doi.org/10.1364/oe.22.027102).
- [26] J. Kim, F. X. Kärtner, and M. H. Perrott, "Femtosecond synchronization of radio frequency signals with optical pulse trains," *Optics Letters*, vol. 29, no. 17, p. 2076, Sep. 2004. doi: [10.1364/ol.29.002076](https://doi.org/10.1364/ol.29.002076).
- [27] K. Jung and J. Kim, "Subfemtosecond synchronization of microwave oscillators with mode-locked Er-fiber lasers," *Optics Letters*, vol. 37, no. 14, p. 2958, Jul. 2012. doi: [10.1364/ol.37.002958](https://doi.org/10.1364/ol.37.002958).
- [28] K. Jung, J. Shin, and J. Kim, "Ultralow phase noise microwave generation from mode-locked Er-fiber lasers with subfemtosecond integrated timing jitter," *IEEE Photonics Journal*, vol. 5, no. 3, pp. 5 500 906–5 500 906, Jun. 2013. doi: [10.1109/jphot.2013.2267533](https://doi.org/10.1109/jphot.2013.2267533).

- [29] A. H. Nejadmalayeri and F. X. Kärtner, "Mach-Zehnder based balanced optical microwave phase detector," in *Conference on Lasers and Electro-Optics 2012*, OSA, 2012, pp. 1–2. doi: [10.1364/cleo_si.2012.ctu2a.1](https://doi.org/10.1364/cleo_si.2012.ctu2a.1).
- [30] "Microwave Analog Signal Generator," Keysight, Santa Rosa, CA, USA, Datasheet E8257D, Feb. 2016.
- [31] "Vector Signal Generator," Rohde & Schwarz, Munich, Germany, Datasheet SMW200A, Dec. 2019, Version 11.00.
- [32] "Rubidium RF/Microwave Signal Generator," Anritsu, Kanagawa, Japan, Datasheet MSG36241A, Nov. 2021, Rev. A.
- [33] P.-L. Liu, K. Williams, M. Frankel, and R. Esman, "Saturation characteristics of fast photodetectors," *IEEE Transactions on Microwave Theory and Techniques*, vol. 47, no. 7, pp. 1297–1303, Jul. 1999. doi: [10.1109/22.775469](https://doi.org/10.1109/22.775469).
- [34] K. Williams, R. Esman, and M. Dagenais, "Effects of high space-charge fields on the response of microwave photodetectors," *IEEE Photonics Technology Letters*, vol. 6, no. 5, pp. 639–641, May 1994. doi: [10.1109/68.285565](https://doi.org/10.1109/68.285565).
- [35] K. Williams and R. Esman, "Design considerations for high-current photodetectors," *Journal of Lightwave Technology*, vol. 17, no. 8, pp. 1443–1454, 1999. doi: [10.1109/50.779167](https://doi.org/10.1109/50.779167).
- [36] A. Beling, X. Xie, and J. C. Campbell, "High-power, high-linearity photodiodes," *Optica*, vol. 3, no. 3, p. 328, Mar. 2016. doi: [10.1364/optica.3.000328](https://doi.org/10.1364/optica.3.000328).
- [37] B. Saleh and M. Teich, *Fundamentals of Photonics* (Wiley Series in Pure and Applied Optics). Hoboken, NJ, USA: Wiley, 1991, ISBN: 0471839655.
- [38] W. Zhang, T. Li, M. Lours, S. Seidelin, G. Santarelli, and Y. L. Coq, "Amplitude to phase conversion of InGaAs pin photo-diodes for femtosecond lasers microwave signal generation," *Applied Physics B*, vol. 106, no. 2, pp. 301–308, Sep. 2011. doi: [10.1007/s00340-011-4710-1](https://doi.org/10.1007/s00340-011-4710-1).
- [39] A. Beling, H. Pan, H. Chen, and J. C. Campbell, "Linearity of modified uni-traveling carrier photodiodes," *Journal of Lightwave Technology*, vol. 26, no. 15, pp. 2373–2378, Aug. 2008. doi: [10.1109/jlt.2008.927184](https://doi.org/10.1109/jlt.2008.927184).
- [40] J. Klamkin, A. Ramaswamy, L. A. Johansson, H.-F. Chou, M. N. Sysak, J. W. Raring, N. Parthasarathy, S. P. DenBaars, J. E. Bowers, and L. A. Coldren, "High output saturation and high-linearity uni-traveling-carrier waveguide photodiodes," *IEEE Photonics Technology Letters*, vol. 19, no. 3, pp. 149–151, Feb. 2007. doi: [10.1109/lpt.2006.890101](https://doi.org/10.1109/lpt.2006.890101).
- [41] A. Joshi and D. Becker, "GRIN lens-coupled top-illuminated photodetectors for high-power applications," in *Microwave Photonics, 2007 International Topical Meeting on*, IEEE, Oct. 2007. doi: [10.1109/mwp.2007.4378124](https://doi.org/10.1109/mwp.2007.4378124).
- [42] A. Joshi, S. Datta, and D. Becker, "GRIN lens coupled top-illuminated highly linear InGaAs photodiodes," *IEEE Photonics Technology Letters*, vol. 20, no. 17, pp. 1500–1502, Sep. 2008. doi: [10.1109/lpt.2008.928532](https://doi.org/10.1109/lpt.2008.928532).
- [43] K. Williams, R. Esman, and M. Dagenais, "Nonlinearities in p-i-n microwave photodetectors," *Journal of Lightwave Technology*, vol. 14, no. 1, pp. 84–96, 1996. doi: [10.1109/50.476141](https://doi.org/10.1109/50.476141).
- [44] H. Jiang, J. Taylor, F. Quinlan, T. Fortier, and S. A. Diddams, "Noise floor reduction of an Er:fiber laser-based photonic microwave generator," *IEEE Photonics Journal*, vol. 3, no. 6, pp. 1004–1012, Dec. 2011. doi: [10.1109/jphot.2011.2171480](https://doi.org/10.1109/jphot.2011.2171480).

- [45] A. Haboucha, W. Zhang, T. Li, M. Lours, A. N. Luiten, Y. L. Coq, and G. Santarelli, "Optical-fiber pulse rate multiplier for ultralow phase-noise signal generation," *Optics Letters*, vol. 36, no. 18, p. 3654, Sep. 2011. doi: [10.1364/ol.36.003654](#).
- [46] S. A. Diddams, M. Kirchner, T. Fortier, D. Braje, A. M. Weiner, and L. Hollberg, "Improved signal-to-noise ratio of 10 GHz microwave signals generated with a mode-filtered femtosecond laser frequency comb," *Optics Express*, vol. 17, no. 5, p. 3331, Feb. 2009. doi: [10.1364/oe.17.003331](#).
- [47] H. Al-Taïy, S. Preußler, S. Brückner, J. Schoebel, and T. Schneider, "Generation of highly stable millimeter waves with low phase noise and narrow linewidth," *IEEE Photonics Technology Letters*, vol. 27, no. 15, pp. 1613–1616, 2015. doi: [10.1109/LPT.2015.2432464](#).
- [48] S. Preussler and T. Schneider, "Tunable generation of high quality mm- and THz-waves for wireless communications with carrier frequencies up to several THz," in *WTC 2014; World Telecommunications Congress 2014*, 2014, pp. 1–5.
- [49] Q. Quraishi, M. Griebel, T. Kleine-Ostmann, and R. Bratschitsch, "Generation of phase-locked and tunable continuous-wave radiation in the terahertz regime," *Opt. Lett.*, vol. 30, no. 23, pp. 3231–3233, Dec. 2005. doi: [10.1364/OL.30.003231](#).
- [50] L. Ponnampalam, R. J. Steed, M. J. Fice, C. C. Renaud, D. C. Rogers, D. G. Moodie, G. D. Maxwell, I. F. Lealman, M. J. Robertson, L. Pavlovic, L. Naglic, M. Vidmar, and A. J. Seeds, "A compact tunable coherent terahertz source based on an hybrid integrated optical phase-lock loop," in *2010 IEEE International Topical Meeting on Microwave Photonics*, 2010, pp. 151–154. doi: [10.1109/MWP.2010.5664138](#).
- [51] L. Ponnampalam, M. J. Fice, F. Pozzi, C. C. Renaud, D. C. Rogers, I. F. Lealman, D. G. Moodie, P. J. Cannard, C. Lynch, L. Johnston, M. J. Robertson, R. Cronin, L. Pavlovic, L. Naglic, M. Vidmar, and A. J. Seeds, "Monolithically integrated photonic heterodyne system," *Journal of Lightwave Technology*, vol. 29, no. 15, pp. 2229–2234, 2011. doi: [10.1109/JLT.2011.2158186](#).
- [52] F. Hindle, G. Mouret, S. Eliet, M. Guinet, A. Cuisset, R. Bocquet, T. Yasui, and D. Rovera, "Widely tunable THz synthesizer," *Applied Physics B*, vol. 104, no. 4, pp. 763–768, Aug. 2011. doi: [10.1007/s00340-011-4690-1](#).
- [53] M. Bahmanian, J. Tiedau, C. Silberhorn, and J. C. Scheytt, "Octave-band microwave frequency synthesizer using mode-locked laser as a reference," in *2019 International Topical Meeting on Microwave Photonics (MWP)*, IEEE, Oct. 2019, pp. 1–4. doi: [10.1109/MWP.2019.8892046](#).
- [54] M. Bahmanian, S. Fard, B. Koppelman, and J. C. Scheytt, "Ultra low phase noise and ultra wide-band frequency synthesizer using an optical clock source," in *2020 IEEE MTT-S International Microwave Symposium (IMS)*, Aug. 2020, pp. 1283–1286. doi: [10.1109/IMS30576.2020.9224118](#).
- [55] M. Bahmanian, C. Kress, and J. C. Scheytt, "Locking of microwave oscillators on the interharmonics of mode-locked laser signals," *Opt. Express*, vol. 30, no. 5, pp. 7763–7771, Feb. 2022. doi: [10.1364/OE.451894](#).
- [56] M. Bahmanian and J. C. Scheytt, "Noise processes and nonlinear mechanisms in optoelectronic phase-locked loop using a balanced optical microwave phase detector," *IEEE Transactions on Microwave Theory and Techniques*, vol. 70, no. 10, pp. 4422–4435, 2022. doi: [10.1109/TMTT.2022.3197621](#).

- [57] T. Udem, R. Holzwarth, and T. W. Hänsch, "Optical frequency metrology," *Nature*, vol. 416, no. 6877, pp. 233–237, Mar. 2002. doi: [10.1038/416233a](https://doi.org/10.1038/416233a).
- [58] T. Udem, J. Reichert, R. Holzwarth, and T. W. Hänsch, "Accurate measurement of large optical frequency differences with a mode-locked laser," *Optics Letters*, vol. 24, no. 13, p. 881, Jul. 1999. doi: [10.1364/ol.24.000881](https://doi.org/10.1364/ol.24.000881).
- [59] J. Reichert, R. Holzwarth, T. Udem, and T. Hänsch, "Measuring the frequency of light with mode-locked lasers," *Optics Communications*, vol. 172, no. 1-6, pp. 59–68, Dec. 1999. doi: [10.1016/s0030-4018\(99\)00491-5](https://doi.org/10.1016/s0030-4018(99)00491-5).
- [60] I. Coddington, W. Swann, and N. Newbury, "Coherent dual-comb spectroscopy at high signal-to-noise ratio," *Physical Review A*, vol. 82, no. 4, p. 043817, Oct. 2010. doi: [10.1103/physreva.82.043817](https://doi.org/10.1103/physreva.82.043817).
- [61] B. Bernhardt, A. Ozawa, P. Jacquet, M. Jacquy, Y. Kobayashi, T. Udem, R. Holzwarth, G. Guelachvili, T. W. Hänsch, and N. Picqué, "Cavity-enhanced dual-comb spectroscopy," *Nature photonics*, vol. 4, no. 1, pp. 55–57, 2010. doi: [10.1038/nphoton.2009.217](https://doi.org/10.1038/nphoton.2009.217).
- [62] A. Cingöz, D. C. Yost, T. K. Allison, A. Ruehl, M. E. Fermann, I. Hartl, and J. Ye, "Direct frequency comb spectroscopy in the extreme ultraviolet," *Nature*, vol. 482, no. 7383, pp. 68–71, Feb. 2012. doi: [10.1038/nature10711](https://doi.org/10.1038/nature10711).
- [63] K. Krzempek, G. Dudzik, and K. Abramski, "Photothermal spectroscopy of CO₂ in an intracavity mode-locked fiber laser configuration," *Optics Express*, vol. 26, no. 22, p. 28861, Oct. 2018. doi: [10.1364/oe.26.028861](https://doi.org/10.1364/oe.26.028861).
- [64] A. Khilo, S. J. Spector, M. E. Grein, A. H. Nejadmalayeri, C. W. Holzwarth, M. Y. Sander, M. S. Dahlem, M. Y. Peng, M. W. Geis, N. A. DiLello, J. U. Yoon, A. Motamedi, J. S. Orcutt, J. P. Wang, C. M. Sorace-Agaskar, M. A. Popović, J. Sun, G.-R. Zhou, H. Byun, J. Chen, J. L. Hoyt, H. I. Smith, R. J. Ram, M. Perrott, T. M. Lyszczarz, E. P. Ippen, and F. X. Kärtner, "Photonic ADC: Overcoming the bottleneck of electronic jitter," *Optics Express*, vol. 20, no. 4, p. 4454, Feb. 2012. doi: [10.1364/oe.20.004454](https://doi.org/10.1364/oe.20.004454).
- [65] C. Deakin and Z. Liu, "Dual frequency comb assisted analog-to-digital conversion," *Optics Letters*, vol. 45, no. 1, p. 173, Dec. 2019. doi: [10.1364/ol.45.000173](https://doi.org/10.1364/ol.45.000173).
- [66] M. Hadjloum, M. E. Gibari, H. Li, and A. S. Daryoush, "Leaky waveguide deflector for 40 GS/s and 6 bits all-optical analog-to-digital converters," *Journal of the Franklin Institute*, vol. 354, no. 18, pp. 8710–8720, Dec. 2017. doi: [10.1016/j.jfranklin.2016.10.042](https://doi.org/10.1016/j.jfranklin.2016.10.042).
- [67] P. Ghelfi, F. Scotti, A. T. Nguyen, G. Serafino, and A. Bogoni, "Novel architecture for a photonics-assisted radar transceiver based on a single mode-locking laser," *IEEE Photonics Technology Letters*, vol. 23, no. 10, pp. 639–641, May 2011. doi: [10.1109/lpt.2011.2120605](https://doi.org/10.1109/lpt.2011.2120605).
- [68] P. Ghelfi, F. Scotti, F. Laghezza, and A. Bogoni, "Photonic generation of phase-modulated RF signals for pulse compression techniques in coherent radars," *Journal of Lightwave Technology*, vol. 30, no. 11, pp. 1638–1644, Jun. 2012. doi: [10.1109/jlt.2012.2187879](https://doi.org/10.1109/jlt.2012.2187879).
- [69] P. Ghelfi, F. Laghezza, F. Scotti, G. Serafino, A. Capria, S. Pinna, D. Onori, C. Porzi, M. Scaffardi, A. Malacarne, V. Vercesi, E. Lazzeri, F. Berizzi, and A. Bogoni, "A fully photonics-based coherent radar system," *Nature*, vol. 507, no. 7492, pp. 341–345, Mar. 2014. doi: [10.1038/nature13078](https://doi.org/10.1038/nature13078).

- [70] H. Haus, "Mode-locking of lasers," *IEEE Journal of Selected Topics in Quantum Electronics*, vol. 6, no. 6, pp. 1173–1185, Nov. 2000. doi: [10.1109/2944.902165](#).
- [71] A. M. Weiner, *Ultrafast Optics*. John Wiley & Sons, Inc., Jun. 2009. doi: [10.1002/9780470473467](#).
- [72] F. X. Kärtner, U. Morgner, T. Schibli, R. Ell, H. A. Haus, J. G. Fujimoto, and E. P. Ippen, "Few-cycle pulses directly from a laser," in *Topics in Applied Physics*, Springer Berlin Heidelberg, Aug. 2004, pp. 73–136. doi: [10.1007/978-3-540-39849-3_2](#).
- [73] R. Paschotta, A. Schlatter, S. Zeller, H. Telle, and U. Keller, "Optical phase noise and carrier-envelope offset noise of mode-locked lasers," *Applied Physics B*, vol. 82, no. 2, pp. 265–273, Dec. 2005. doi: [10.1007/s00340-005-2041-9](#).
- [74] R. Paschotta, "Timing jitter and phase noise of mode-locked fiber lasers," *Optics Express*, vol. 18, no. 5, p. 5041, Feb. 2010. doi: [10.1364/oe.18.005041](#).
- [75] J. Kim and Y. Song, "Ultralow-noise mode-locked fiber lasers and frequency combs: Principles, status, and applications," *Advances in Optics and Photonics*, vol. 8, no. 3, p. 465, Aug. 2016. doi: [10.1364/aop.8.000465](#).
- [76] P.-T. Ho, "Phase and amplitude fluctuations in a mode-locked laser," *IEEE Journal of Quantum Electronics*, vol. 21, no. 11, pp. 1806–1813, 1985. doi: [10.1109/JQE.1985.1072594](#).
- [77] D. M. B. Lesko, A. J. Lind, N. Hoghooghi, A. Kowligy, H. Timmers, P. Sekhar, B. Rudin, F. Emaury, G. B. Rieker, and S. A. Diddams, "Fully phase-stabilized 1 GHz turnkey frequency comb at 1.56 μm ," *OSA Continuum*, vol. 3, no. 8, pp. 2070–2077, Aug. 2020. doi: [10.1364/OSAC.396597](#).
- [78] "Ultrastable Laser System," Menlo Systems, Martinsried, Germany, Datasheet ORS, Dec. 2021.
- [79] P. R. Gray, P. J. Hurst, and S. H. Lewis, *Analysis and Design of Analog Integrated Circuits*. Hoboken, NJ, USA: WILEY, Apr. 1, 2009, 881 pp., ISBN: 0470245999.
- [80] T. Lamb, "Laser-to-RF Phase Detection with Femtosecond Precision for Remote Reference Phase Stabilization in Particle Accelerators," Technische Universität Hamburg Harburg, Diss., 2016, Dr. Technische Universität Hamburg Harburg, Hamburg, 2017, p. 174. doi: [10.3204/PUBDB-2017-02117](#).
- [81] R. Loudon, *The quantum theory of light*. Oxford, U.K.: OUP Oxford, 2000, ISBN: 0198501765.
- [82] F. Quinlan, T. M. Fortier, H. Jiang, and S. A. Diddams, "Analysis of shot noise in the detection of ultrashort optical pulse trains," *Journal of the Optical Society of America B*, vol. 30, no. 6, p. 1775, May 2013. doi: [10.1364/josab.30.001775](#).
- [83] K. M. van Vliet, "Irreversible thermodynamics and carrier density fluctuations in semiconductors," *Phys. Rev.*, vol. 110, pp. 50–61, 1 Apr. 1958. doi: [10.1103/PhysRev.110.50](#).
- [84] W. van Roosbroeck and W. Shockley, "Photon-radiative recombination of electrons and holes in germanium," *Phys. Rev.*, vol. 94, pp. 1558–1560, 6 Jun. 1954. doi: [10.1103/PhysRev.94.1558](#).

- [85] P. W. Juodawlkis, F. J. O'Donnell, J. J. Hargreaves, D. C. Oakley, A. Napoleone, S. H. Groves, L. J. Mahoney, K. M. Molvar, L. J. Missaggia, J. P. Donnelly, R. C. Williamson, and J. C. Twichell, "Absorption saturation nonlinearity in InGaAs/InP p-i-n photodiodes", in *The 15th Annual Meeting of the IEEE Lasers and Electro-Optics Society*, vol. 2, 2002, pp. 426–427. doi: [10.1109/LEOS.2002.1159361](https://doi.org/10.1109/LEOS.2002.1159361).
- [86] J. Wei, D. Kwon, S. Zhang, S. Pan, and J. Kim, "All-fiber-photonics-based ultralow-noise agile frequency synthesizer for x-band radars," *Photonics Research*, vol. 6, no. 1, p. 12, Dec. 2017. doi: [10.1364/prj.6.000012](https://doi.org/10.1364/prj.6.000012).
- [87] P. Park, D. Park, and S. Cho, "A low-noise and low-power frequency synthesizer using offset phase-locked loop in 0.13- μ m cmos," *IEEE Microwave and Wireless Components Letters*, vol. 20, no. 1, pp. 52–54, Jan. 2010. doi: [10.1109/lmwc.2009.2035967](https://doi.org/10.1109/lmwc.2009.2035967).

Das Heinz Nixdorf Institut – Interdisziplinäres Forschungszentrum für Informatik und Technik

Das Heinz Nixdorf Institut ist ein Forschungszentrum der Universität Paderborn. Es entstand 1987 aus der Initiative und mit Förderung von Heinz Nixdorf. Damit wollte er Ingenieurwissenschaften und Informatik zusammenführen, um wesentliche Impulse für neue Produkte und Dienstleistungen zu erzeugen. Dies schließt auch die Wechselwirkungen mit dem gesellschaftlichen Umfeld ein.

Die Forschungsarbeit orientiert sich an dem Programm „Dynamik, Mobilität, Vernetzung: Eine neue Schule des Entwurfs der technischen Systeme von morgen“. In der Lehre engagiert sich das Heinz Nixdorf Institut in Studiengängen der Informatik, der Ingenieurwissenschaften und der Wirtschaftswissenschaften.

Heute wirken am Heinz Nixdorf Institut neun Professoren mit insgesamt 150 Mitarbeiterinnen und Mitarbeitern. Pro Jahr promovieren hier etwa 20 Nachwuchswissenschaftlerinnen und Nachwuchswissenschaftler.

Heinz Nixdorf Institute – Interdisciplinary Research Centre for Computer Science and Technology

The Heinz Nixdorf Institute is a research centre within the University of Paderborn. It was founded in 1987 initiated and supported by Heinz Nixdorf. By doing so he wanted to create a symbiosis of computer science and engineering in order to provide critical impetus for new products and services. This includes interactions with the social environment.

Our research is aligned with the program „Dynamics, Mobility, Integration: Enroute to the technical systems of tomorrow.“ In training and education the Heinz Nixdorf Institute is involved in many programs of study at the University of Paderborn. The superior goal in education and training is to communicate competencies that are critical in tomorrow's economy.

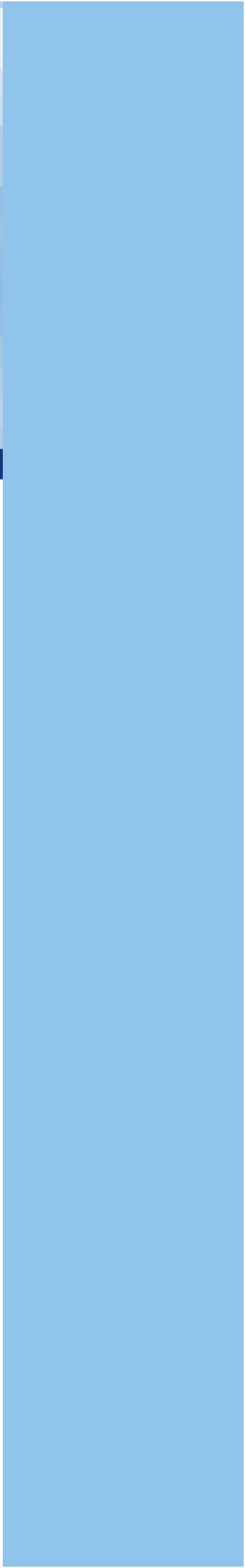
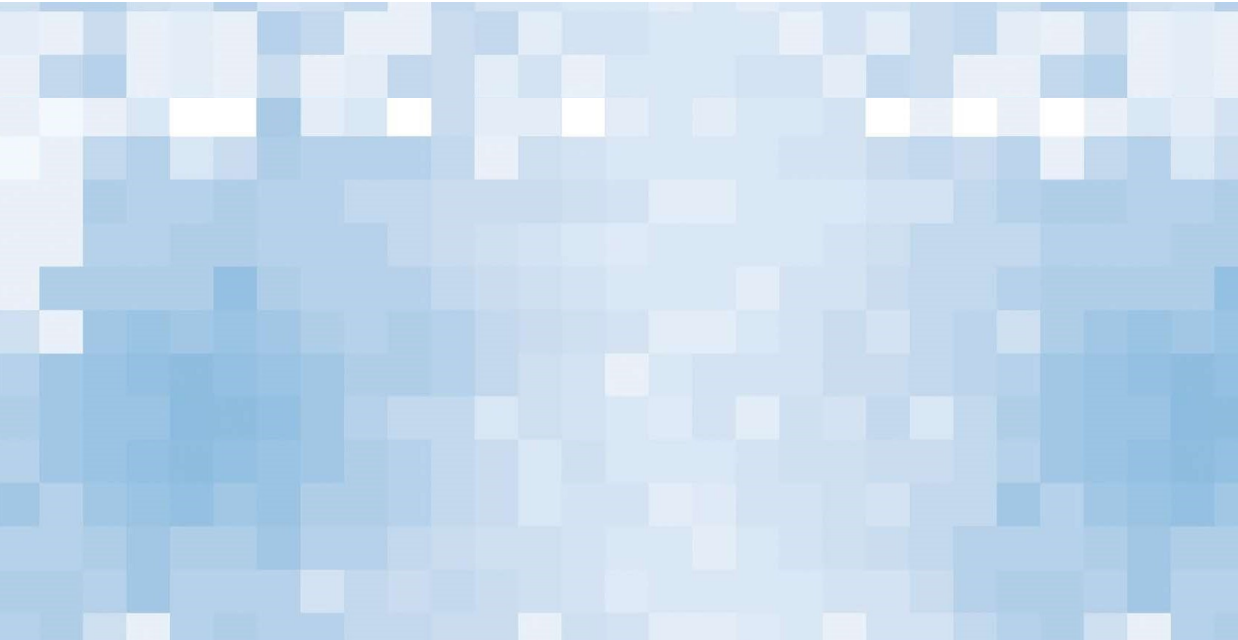
Today nine Professors and 150 researchers work at the Heinz Nixdorf Institute. Per year approximately 20 young researchers receive a doctorate.

Zuletzt erschienene Bände der Verlagsschriftenreihe des Heinz Nixdorf Instituts

- Bd. 394 LOCHBICHLER, M.: *Systematische Wahl einer Modellierungstiefe im Entwurfsprozess mechatronischer Systeme*, Dissertation. Fakultät für Maschinenbau, Universität Paderborn: Verlagsschriftenreihe des Heinz Nixdorf Instituts, Paderborn, 2020, Band 394, ISBN: 978-3-947647-13-2
- Bd. 395 LUKEI, M.: *Systematik zur integrativen Entwicklung von mechatronischen Produkten und deren Prüfmittel*, Dissertation. Fakultät für Maschinenbau, Universität Paderborn: Verlagsschriftenreihe des Heinz Nixdorf Instituts, Paderborn, 2020, Band 395, ISBN: 978-3-947647-14-9
- Bd. 396 KOHLSTEDT, A.: *Modellbasierte Synthese einer hybriden Kraft-/Positionsregelung für einen Fahrzeugachsprüfstand mit hydraulischem Hexapod*, Dissertation. Fakultät für Maschinenbau, Universität Paderborn: Verlagsschriftenreihe des Heinz Nixdorf Instituts, Paderborn, 2021, Band 396, ISBN: ISBN 978-3-947647-15-6
- Bd. 397 DREWEL, M.: *Systematik zum Einstieg in die Plattformökonomie*, Dissertation. Fakultät für Maschinenbau, Universität Paderborn: Verlagsschriftenreihe des Heinz Nixdorf Instituts, Paderborn, 2021, Band 397, ISBN: 978-3-947647-16-3
- Bd. 398 FRANK, M.: *Systematik zur Planung des organisationalen Wandels zum Smart Service-Anbieter*, Dissertation. Fakultät für Maschinenbau, Universität Paderborn: Verlagsschriftenreihe des Heinz Nixdorf Instituts, Paderborn, 2021, Band 398, ISBN: 978-3-947647-17-0
- Bd. 399 KOLDEWEY, C.: *Systematik zur Entwicklung von Smart Service-Strategien im produzierenden Gewerbe*, Dissertation. Fakultät für Maschinenbau, Universität Paderborn: Verlagsschriftenreihe des Heinz Nixdorf Instituts, Paderborn, 2021, Band 399, ISBN: 978-3-947647-18-7
- Bd. 400 GAUSEMEIER, J.: *Vorausschau und Technologieplanung : 16. Symposium für Vorausschau und Technologieplanung*. Berlin-Brandenburgische Akademie der Wissenschaften, Berlin: Verlagsschriftenreihe des Heinz Nixdorf Instituts, Paderborn, 2021, Band 400, ISBN: 978-3-947647-19-4
- Bd. 401 BRETZ, L. H.: *Rahmenwerk zur Planung und Einführung von Systems Engineering und Model-Based Systems Engineering*, Dissertation. Fakultät für Elektrotechnik, Informatik und Mathematik, Universität Paderborn: Verlagsschriftenreihe des Heinz Nixdorf Instituts, Paderborn, 2021, Band 401, ISBN: 978-3-947647-20-0
- Bd. 402 WU, L.: *Ultrabroadband sampling circuits in SiGe BiCMOS technology for time interleaved analog-to-digital converter*, Dissertation. Fakultät für Elektrotechnik, Informatik und Mathematik, Universität Paderborn: Verlagsschriftenreihe des Heinz Nixdorf Instituts, Paderborn, 2021, Band 402, ISBN: 978-3-947647-21-7
- Bd. 403 HILLEBRAND, M.: *Entwicklungssystematik zur Integration von Eigenschaften der Selbstheilung in Intelligente Technische Systeme*, Dissertation. Fakultät für Maschinenbau, Universität Paderborn: Verlagsschriftenreihe des Heinz Nixdorf Instituts, Paderborn, 2021, Band 403, ISBN: 978-3-947647-22-4
- Bd. 404 OLMA, S.: *Systemtheorie von Hardware-in-the-Loop-Simulationen mit Anwendung auf einem Fahrzeugachsprüfstand mit parallel-kinematischem Lastsimulator*, Dissertation. Fakultät für Maschinenbau, Universität Paderborn: Verlagsschriftenreihe des Heinz Nixdorf Instituts, Paderborn, 2021, Band 404, ISBN: 978-3-947647-23-1
- Bd. 405 CHRISTIAN, F.: *Rahmenwerk zur Gestaltung des Technologietransfers in mittelständisch geprägten Innovationsclustern*, Dissertation. Fakultät für Maschinenbau, Universität Paderborn: Verlagsschriftenreihe des Heinz Nixdorf Instituts, Paderborn, 2022, Band 405, ISBN: 978-3-947647-24-8
- Bd. 406 OLEFF, C.: *Proaktives Management von Anforderungsänderungen in der Entwicklung komplexer technischer Systeme*, Dissertation. Fakultät für Maschinenbau, Universität Paderborn: Verlagsschriftenreihe des Heinz Nixdorf Instituts, Paderborn, 2022, Band 406, ISBN: 978-3-947647-25-5

Zuletzt erschienene Bände der Verlagsschriftenreihe des Heinz Nixdorf Instituts

- Bd. 407 JAVED, A. R.: *Mixed-Signal Baseband Circuit Design for High Data Rate Wireless Communication in Bulk CMOS and SiGe BiCMOS Technologies*, Dissertation. Fakultät für Elektrotechnik, Informatik und Mathematik, Universität Paderborn: Verlagsschriftenreihe des Heinz Nixdorf Instituts, Paderborn, 2022, Band 407, ISBN: 978-3-947647-26-2
- Bd. 408 DUMITRESCU, R. und KOLDEWEY, C.: *Datengestützte Produktplanung*, Dissertation. Fakultät für Elektrotechnik, Informatik und Mathematik, Universität Paderborn: Verlagsschriftenreihe des Heinz Nixdorf Instituts, Paderborn, 2023, Band 408, ISBN: 978-3-947647-27-9
- Bd. 409 PÖHLER, A.: *Automatisierte dezentrale Produktionssteuerung für cyber-physische Produktionssysteme mit digitaler Repräsentation der Beschäftigten*, Dissertation. Fakultät für Maschinenbau, Universität Paderborn: Verlagsschriftenreihe des Heinz Nixdorf Instituts, Paderborn, 2022, Band 409, ISBN: 978-3-947647-28-6
- Bd. 410 RÜDDENKLAU, N.: *Hardware-in-the-Loop-Simulation von HD-Scheinwerfer-Steuergeräten zur Entwicklung von Lichtfunktionen in virtuellen Nachtfahrten*, Dissertation. Fakultät für Maschinenbau, Universität Paderborn: Verlagsschriftenreihe des Heinz Nixdorf Instituts, Paderborn, 2023, Band 410, ISBN: 978-3-947647-29-3
- Bd. 411 BIEMELT, P.: *Entwurf und Analyse modellprädiktiver Regelungsansätze zur Steigerung des Immersionsempfindens in interaktiven Fahrsimulationen*, Dissertation. Fakultät für Maschinenbau, Universität Paderborn: Verlagsschriftenreihe des Heinz Nixdorf Instituts, Paderborn, 2023, Band 411, ISBN: 978-3-947647-30-9
- Bd. 412 HAAKE, C.-J., MEYER AUF DER HEIDE, F., PLATZNER, M., WACHSMUTH, H. und WEHRHEIM, H.: *On-The-Fly Computing: Individualized IT-services in dynamic markets: Collaborative Research Centre 901 (2011 - 2023)*. Verlagsschriftenreihe des Heinz Nixdorf Instituts, Paderborn, 2023, Band 412, ISBN: 978-3-947647-31-6
- Bd. 413 DUMITRESCU, R. und HÖLZLE, K.: *Vorausschau und Technologieplanung: 17. Symposium für Vorausschau und Technologieplanung, 14. und 15. September 2023, Berlin*. Berlin-Brandenburgische Akademie der Wissenschaften, Berlin: Verlagsschriftenreihe des Heinz Nixdorf Instituts, Paderborn, 2023, Band 413, ISBN: 978-3-947647-32-3
- Bd. 414 ABUGHANNAM, S.: *Low-power Direct-detection Wake-up Receiver at 2.44 GHz for Wireless Sensor Networks*, Dissertation. Fakultät für Elektrotechnik, Informatik und Mathematik, Universität Paderborn: Verlagsschriftenreihe des Heinz Nixdorf Instituts, Paderborn, 2023, Band 414, ISBN: 978-3-947647-33-0
- Bd. 415 REINHOLD, J.: *Systematik zur musterbasierten Transformation von Wertschöpfungs-systemen für Smart Services*, Dissertation. Fakultät für Maschinenbau, Universität Paderborn: Verlagsschriftenreihe des Heinz Nixdorf Instituts, Paderborn, 2023, Band 415, ISBN: 978-3-947647-34-7
- Bd. 416 YANG, X.: *Eine Methode zur Unterstützung von Entscheidungen bei der Entwicklung modularer Leichtbauprodukte*, Dissertation. Fakultät für Maschinenbau, Universität Paderborn: Verlagsschriftenreihe des Heinz Nixdorf Instituts, Paderborn, 2023, Band 416, ISBN: 978-3-947647-35-4
- Bd. 417 GRÄLER, M.: *Entwicklung adaptiver Einrichtungsassistenzsysteme für Produktionsprozesse*, Dissertation. Fakultät für Maschinenbau, Universität Paderborn: Verlagsschriftenreihe des Heinz Nixdorf Instituts, Paderborn, 2023, Band 417, ISBN: 978-3-947647-36-1
- Bd. 418 RÖSMANN, D.: *Menschenzentrierte Montageplanung und -steuerung durch fähigkeitsorientierte Aufgabenzuordnung*, Dissertation. Fakultät für Maschinenbau, Universität Paderborn: Verlagsschriftenreihe des Heinz Nixdorf Instituts, Paderborn, 2024, Band 418, ISBN: 978-3-947647-37-8



This work demonstrates the analysis and implementation of MLL-based ultralow-noise optoelectronic PLL, the so-called OEPLL. Different RF-generation techniques using MLL are discussed and it is shown that the OEPLL is a suitable architecture for low-noise and wide-band frequency synthesis. The OEPLL is analyzed thoroughly at the system level and the component level, and different noise processes and nonlinear mechanisms are modeled. The results are used to design an ultralow-noise OEPLL with a frequency range of 2–20 GHz. The in-band phase noise of the OEPLL at 100 kHz offset frequency is below -150 dBc/Hz for a carrier frequency of 10 GHz, which is more than 10 dB below that of state-of-the-art commercial frequency synthesizers.